IPP-Report

Max-Planck-Institut
für Plasmaphysik

Matthias Hölzl

Diffusiver Wärmetransport über magnetische Inseln und stochastische Schichten in Tokamaks

Diffusive Heat Transport across Magnetic Islands and Stochastic Layers in Tokamaks

IPP 10/38
März, 2010

Technische Universität München
Fakultät für Physik
Max-Planck-Institut für Plasmaphysik

Diffusive Heat Transport across Magnetic Islands and Stochastic Layers in Tokamaks

Matthias Hölzl

Vollständiger Abdruck der von der Fakultät für Physik der Technischen Universität München zur Erlangung des akademischen Grades eines Doktors der Naturwissenschaften (Dr. rer. nat.) genehmigten Dissertation.

Vorsitzender: Univ.-Prof. Dr. St. Paul
Prüfer der Dissertation:

1. Hon.-Prof. Dr. S. Günter
2. Univ.-Prof. Dr. K. Krischer

Die Dissertation wurde am 30.10.2009 bei der Technischen Universität München eingereicht und durch die Fakultät für Physik am 29.01.2010 angenommen.

Diffusive Heat Transport across Magnetic Islands and Stochastic Layers in Tokamaks

Dissertation
von
Matthias Hölzl

durchgeführt am
Max-Planck-Institut für Plasmaphysik

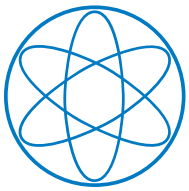

Physik Department der
Technischen Universität München

Abstract

In tokamak experiments, neoclassical tearing modes (NTMs) limit the maximum achievable pressure gradients. These modes can cause a sudden loss of the complete plasma confinement, which may damage the the vacuum vessel walls. An improved understanding of neoclassical tearing modes is therefore of great relevance for the development of an economic magnetic confinement fusion power plant. The driving term of NTM instabilities is tightly connected to heat transport phenomena, that are governed by a huge anisotropy in magnetized plasmas. Heat conduction along magnetic field lines, which is dominated by free-streaming electrons, is faster by up to ten orders of magnitude than cross-field transport that is mostly driven by turbulence.

This dissertation treats the plasma as a magnetized fluid and investigates the anisotropic heat transport from the hot plasma core towards the colder plasma boundary. The transport across magnetic islands and ergodic layers is simulated numerically with realistic plasma parameters. The computations are performed in unsheared helical coordinate systems with a finite difference scheme that does not require an exact alignment of the coordinate system to the magnetic field lines in spite of the pronounced heat diffusion anisotropy. Simulations are carried out for, both, simplified cylindrical and realistic tokamak geometries. This allows to perform direct comparisons to analytical predictions as well as to measurements in tokamak experiments and gain information regarding the stability properties of NTMs and important experimental plasma parameters.

The flattening of the temperature distribution inside islands is examined revealing significant differences between the in- and outboard sides of the torus. The reduction of the core plasma temperature due to the enhanced radial transport across magnetic islands is investigated and the characteristics of the NTM driving term are determined from numerical simulations, allowing to give an empirical correction factor for analytical predictions.

The exact value of the heat diffusion anisotropy is not well known in experiments, as there exists no direct way for measuring it. In this work, an approach is made to determine this quantity by comparing simulations of the heat transport across magnetic islands to measurements of the electron temperature at the tokamaks TEXTOR and ASDEX Upgrade. This way, the width of the magnetic island and the heat diffusion anisotropy are determined for individual transits of the rotating mode around the torus. The observed anisotropy is significantly lower than the classical prediction by Spitzer and Härm, indicating that the so-called heat flux limit determines heat transport across magnetic islands.

Overlapping islands lead to the formation of an ergodic layer in which magnetic field lines become stochastic, i.e., move randomly through that layer. The radial heat transport across

the layer is enhanced as a contribution along magnetic field lines arises. This is examined in cylindrical and toroidal geometries, revealing that single island effects dominate for low to moderate heat diffusion anisotropies which leads to a flattening of the temperature distribution in the individual island regions. For larger anisotropies, radial transport across the ergodic layer is increased strongly beyond single island values, causing a flattening of the temperature distribution in the whole layer. A comparison of the heat transport across a highly ergodic region produced by strongly overlapping islands to classical analytical predictions yields qualitative agreement while the predicted values cannot be approved.

It is demonstrated, that the sudden amplitude drop observed in high pressure experiments at neoclassical tearing modes in the so-called frequently interrupted regime may be tightly connected to an ergodization of the magnetic field structure at the NTM. The ergodization reduces the resonant helical perturbation of the plasma current, removing a large fraction of the island drive. In simulations of the heat transport across an ergodic plasma boundary in ASDEX Upgrade geometry, a considerable drop of the edge temperature pedestal height is observed when Spitzer-Härm conductivity is assumed.

Kurzfassung

In Tokamak-Experimenten limitieren neoklassische Tearing-Moden (NTMs) die maximal erreichbaren Druckgradienten. Diese Moden können außerdem zu einem plötzlichen Verlust des Plasma-Einschlusses und so zu einer Beschädigung der Wände des Vakuum-Gefäßes führen. Ein verbessertes Verständnis der Physik neoklassischer Tearing-Moden is somit von großer Bedeutung für die Entwicklung eines ökonomischen Fusionskraftwerks mit magnetischem Einschluss. Der Antrieb von NTM-Instabilitäten ist eng verbunden mit Wärmetransport-Phänomenen die in magnetisierten Plasmen durch eine enorme Anisotropie bestimmt werden. Der Wärmetransport entlang magnetischer Feldlinien erfolgt um bis zu zehn Größenordnungen schneller als der vorwiegend turbulente Senkrecht-Transport.

In dieser Dissertation wird das Plasma als magnetisiertes Fluid behandelt und der anisotrope Wärmetransport vom heißen Plasmazentrum hin zum kälteren Plasmarand untersucht. Der Wärmefluss über magnetische Inseln und ergodische Schichten wird mit realistischen Plasma-Parametern numerisch simuliert. Die Berechnungen werden in unverscherten helikalen Koordinatensystemen mit einem Finite-Differenzen-Verfahren durchgeführt, das trotz der ausgeprägten Anisotropie der Wärmeleitfähigkeit keine exakte Ausrichtung der Koordinaten an den magnetischen Feldlinien erfordert. Die Simulationen erfolgen in vereinfachten zylindrischen und in realistischen Tokamak-Geometrien. So sind direkte Vergleiche sowohl mit analytischen Vorhersagen als auch mit Messungen in Tokamak-Experimenten möglich, wodurch Informationen über das Stabilitätsverhalten von NTMs und über wichtige Plasma-Parametern gewonnen werden.

Die Abflachung der Temperatur-Verteilung im Inneren von Inseln wird untersucht, wobei sich deutliche Unterschiede zwischen Innen- und Außenseite des Torus ergeben. Die Verringerung der Plasma-Kerntemperatur durch den erhöhten radialen Transport über magnetische Inseln wird eruiert. Die Eigenschaften des Antriebsmechanismus von NTMs werden betrachtet wodurch ein empirischer Korrektur-Term für analytische Vorhersagen bestimmt werden kann.

Die Anisotropie der Wärmeleitfähigkeit in den Plasma-Experimenten ist nicht genau bekannt, da es keine Möglichkeit gibt, diese direkt zu messen. In der vorliegenden Arbeit wird daher der Versuch unternommen, die Anisotropie durch den Vergleich von Simulationen des Wärmeflusses über magnetische Inseln mit Messungen der Elektronentemperatur in den Tokamak-Experimenten TEXTOR und ASDEX Upgrade zu bestimmen. Dadurch wird die Inselbreite und die Anisotropie der Wärmeleitfähigkeit jeweils für einzelne Umläufe der um den Torus rotierenden Moden ermittelt. Die so detektierte Anisotropie ist erheblich kleiner als in der einschlägigen Arbeit von Spitzer und Härm vorhergesagt was einen wichtigen Hin-

weis darauf liefert, dass der Wärme-Transport über magnetische Inseln durch die sogenannte Heat-Flux-Limit-Theorie bestimmt wird.

Mehrere sich überlappende Inseln führen zur Entstehung einer ergodisierten Schicht, in der magnetische Feldlinien stochastisch werden, sich also zufällig durch diese Schicht bewegen. Der radiale Wärmetransport über eine derartige Schicht ist erhöht, da ein Beitrag entlang von magnetischen Feldlinien auftritt. Dies wird in zylindrischer und toroidaler Geometrie untersucht wobei sich zeigt, dass die Effekte einzelner Inseln bei niedrigen bis mittleren Anisotropien der Wärmeleitfähigkeit dominieren, wodurch die Temperaturverteilung im Bereich der einzelnen Inseln abflacht. Bei höheren Anisotropien ist der radiale Transport über die ergodische Schicht stark gegenüber den Effekten der einzelnen Inseln erhöht, was eine Abflachung der Temperaturverteilung in der gesamten Schicht hervorruft. Ein Vergleich des Wärmetransports über eine hoch-ergodische Schicht, die durch stark überlappende Inseln erzeugt wird, mit klassischen analytischen Vorhersagen zeigt qualitative Übereinstimmung, während die vorhergesagten Werte nicht bestätigt werden können.

Es wird ferner gezeigt, dass der plötzliche Amplituden-Abfall neoklassischer Tearing-Moden, der in Experimenten bei hohem Druck beobachtet wurde, in engem Zusammenhang mit einer Ergodisierung der Magnetfeldstruktur am Ort der Mode stehen könnte. Die Ergodisierung verringert die resonante helikale Störung des Plasmastroms, wodurch ein großer Teil des Moden-Antriebs unterdrückt wird. Der Wärmetransport über einen ergodisierten Plasmarand wird in der Geometrie von ASDEX Upgrade untersucht. Ein deutlicher Abfall der Höhe des Temperatur-Pedestals am Plasmarand wird unter der Annahme von Spitzer-Härm Leitfähigkeit beobachtet.

Contents

Nomenclature

a	Minor radius of the plasma
$\mathbf{B}$	Magnetic field vector
$\mathbf{b} = \mathbf{B}/B$	Magnetic field direction vector
$\chi = \chi_{\|\|}/\chi_{\perp}$	Heat diffusion anisotropy
$\chi_{\|\|}$	Heat diffusion coefficient along magnetic field lines
$\chi_{\perp}$	Heat diffusion coefficient perpendicular to the magnetic field lines
Δ'	Classical tearing stability index
Δ_{bs}	Tearing stability contribution from bootstrap current perturbations
$\Delta\iota$	Coordinate misalignment with respect to a magnetic island
dw/dt	Island growth rate
$\mathbf{e}^{\alpha}$	Contravariant basis vectors
$\mathbf{e}_{\alpha}$	Covariant basis vectors
$g = \det\left[g_{\alpha\beta}\right]$	Determinant of the covariant metric tensor
$g^{\alpha\beta}$	Contravariant metric tensor elements
$g_{\alpha\beta}$	Covariant metric tensor elements
$\nabla_{\|\|}T$	Temperature gradient along magnetic field lines
$\nabla_{\perp}T$	Temperature gradient perpendicular to magnetic field lines
$\iota = q^{-1}$	Rotational transform
ι_c	Coordinate helicity
j	Plasma current density
κ_{ρ}	Effective radial heat diffusivity, χ_{ρ}, normalized to $\chi_{\perp}$
κ_{ρ}^{+}	Increase of κ_{ρ} due to a magnetic perturbation
m	Poloidal mode number
n	Toroidal mode number
n_e	Electron particle density
P	Heat source density
p	Plasma Pressure
Φ	Toroidal magnetic flux

ϕ ..... Toroidal coordinate (→ Section 4.3.2)
Ψ ..... Poloidal magnetic flux
$\mathbf{q}$ ..... Heat flux density vector
R ..... Local major radius (distance to the torus axis)
r ..... Local minor radius (→ Section 4.3.6)
R_0 ..... Major radius of the plasma
r_s ..... Minor radius at the position of the considered resonant surface
ρ ..... Radial coordinate (→ Section 4.3.2)
σ_{Ch} ..... Chirikov parameter (measures degree of ergodization, → Section 2.7)
θ ..... Poloidal coordinate (→ Section 4.3.2)
w ..... Island width (radial extent of the island separatrix)
w_c ..... Scale island width for temperature flattening (→ Section 2.5.3)
Z ..... Vertical coordinate

Chapter 1.

Introduction

This dissertation tries to answer some open questions related to the heat transport properties of magnetized plasmas and the consequences for plasma instabilities like neoclassical tearing modes. Hence, numerical simulations of heat transport across magnetic islands and stochastic field layers are carried out in realistic tokamak geometry with realistic plasma parameters. The results are compared to analytical theories and measurements of the electron temperature in several magnetic confinement fusion devices.

This first Chapter gives a quick overview of nuclear fusion research and the magnetic confinement of fusion plasmas before it introduces the topic of the work at hand. In magnetized plasmas, heat transport is dominated by a pronounced anisotropy as the transport is much more efficient along magnetic field lines than perpendicular to them. Thus, the magnetic topology influences heat transport significantly and structures like magnetic islands and stochastic field layers have a strong impact on the heat transport which can, in turn, act back on certain plasma instabilities like neoclassical tearing modes.

Contents

1.1. Nuclear Fusion

The interplay of attractive and repulsive forces inside atomic nuclei leads to a non-monotonic dependence of the binding energy per nucleon on the atomic number. The most stable nucleus is the medium-size iron isotope ^{56}Fe. Thus, energy may be produced by, either, splitting large atomic nuclei into smaller ones – nuclear fission – or merging small atomic nuclei into larger ones – nuclear fusion. The fusion reaction of the heavy hydrogen isotopes deuterium

and tritium, $D + T \rightarrow {}^4_2He + n + 17.6$ MeV, features the largest reaction parameter of the candidates under consideration. The reaction parameter reaches its maximum value for the D-T reaction at temperatures of several 10 keV[1]. At these temperatures, the hydrogen isotopes form a plasma. Since fusion processes are still less probable than Coulomb collisions at each deuterium tritium collision event, the plasma needs to be confined well enough to ensure that each particle performs many collisions before it is lost. While gravitation provides the confinement inside stars, inertial and magnetic confinement are the candidates for the technological realizations of controlled fusion.

1.2. Magnetic Plasma Confinement

Magnetic confinement fusion, which is of interest for the work at hand, tries to develop optimized magnetic field configurations for a steady plasma confinement. The magnetic field is capable of confining the plasma in the cross-field directions only, while charged particles may move freely along the field lines[2]. Thus, a toroidal configuration is required to avoid end losses. However, the charge-dependent particle drift that arises from the intrinsically inhomogeneous magnetic field strength of toroidal devices, the ∇B drift, gives rise to a vertical electrical field[3]. The latter electrical field, in turn, causes the so called $E \times B$ drift that is oriented radially outwards and renders a purely toroidal magnetic field configuration unstable. An additional poloidal magnetic field component is required to stabilize the configuration such that the magnetic field lines wind helically around the torus.

tokamak

Such a helical magnetic field structure can be generated by non-planar magnetic field coils in the stellarator concept or by driving a toroidal plasma current to produce the poloidal magnetic field component in the tokamak concept. Tokamaks are the currently furthest developed magnetic confinement devices. The next generation fusion device, ITER, to be built and operated by an international cooperation on a site in France, will also be of the tokamak type. Refer to Reference [Wesson04] for a comprehensive introduction to tokamak physics. A schematic illustration of a tokamak plasma configuration is shown in Figure 1.1. Unperturbed tokamak equilibria contain nested so-called magnetic flux surfaces. Every magnetic field line is situated on one of these surfaces and stays on it while winding helically around the torus.

flux surface

Poincaré plot

The flux surfaces can be visualized by a Poincaré plot for which a selected set of field lines is traced over many toroidal turns. The position of each field line is marked after every toroidal turn, such that the field lines trace out their respective flux surfaces. A Poincaré plot of an equilibrium in the ASDEX Upgrade tokamak is shown in Figure 1.2. Here, the nested flux surfaces are surrounded by a last closed magnetic surface that is also called separatrix.

separatrix

[1] Temperatures are measured in units of energy assuming the Boltzmann constant as an implicit prefactor. An energy of 1 eV corresponds to a temperature of 11604.5 K.

[2] The free particle motion along magnetic field lines is somewhat restricted in the presence of magnetic field inhomogeneities as discussed in Section 2.3.3.

[3] Particle drifts are briefly discussed in Section 2.3.2. More details may be found, e.g., in Reference [Boyd03].

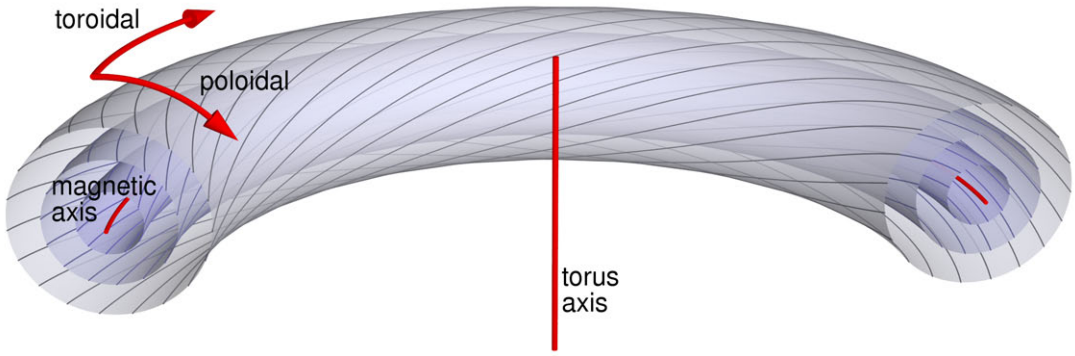

FIGURE 1.1. *Tokamaks are magnetic confinement devices that are virtually axisymmetric about the torus axis. The toroidal magnetic field component is produced by external coils, while the poloidal component is generated by a toroidal plasma current. The illustration shows a simplified tokamak plasma with a circular cross-section. Some of the nested magnetic flux surfaces and the magnetic field lines that wind helically around the torus on these surfaces are depicted.*

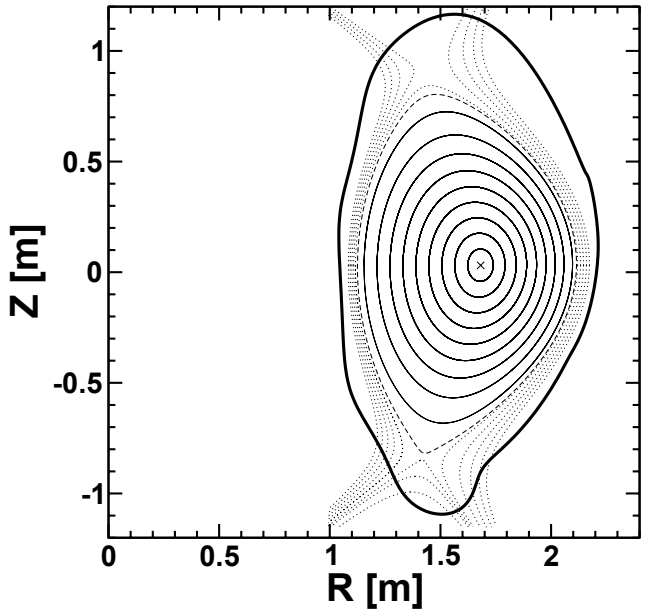

FIGURE 1.2. *The equilibrium magnetic field configuration of ASDEX Upgrade is visualized by a Poincaré plot. Inside the plasma region, magnetic field lines are located on nested magnetic flux surfaces (solid lines). The plasma is surrounded by the so-called last closed magnetic flux surface (lcms, dashed line). Flux surfaces outside the lcms (dotted lines) intersect with the first wall of the vacuum vessel (thick solid line, simplified wall model).*

divertor

Magnetic field lines that are situated on surfaces outside but close to the separatrix intersect with the first wall at the so-called divertor tiles. This way, energy and particle losses are transported to a well defined region and impurities can be removed with vacuum pumps. This divertor configuration is used in many state of the art tokamaks to avoid impurity transport from the first walls into the plasma.

The presence of the strong magnetic field introduces a distinct anisotropy to many plasma parameters. For instance, heat transport is faster by up to ten orders of magnitude parallel to the magnetic field lines than perpendicular to them. The physical processes responsible for this anisotropy are explained in Section 2.4. It will be one aim of this work to determine the true value of the heat diffusion anisotropy in fusion experiments by comparing numerical simulations to experimental temperature measurements. In an unperturbed tokamak equilibrium, the anisotropic heat transport levels any temperature inhomogeneities within a magnetic flux surface on a very short time scale. Hence, the temperature is virtually constant within each unperturbed flux surface.

1.3. Magnetic Islands

magnetic island

safety factor

rational surface

resonant surface

A magnetic island is a flux tube of locally nested magnetic flux surfaces that winds helically around the torus[4]. The magnetic field topology changes when a magnetic island evolves which may affect heat transport drastically. For island formation, the helicity of the magnetic field lines plays an important role. It is measured by the safety factor, q, that is defined as the number of toroidal turns a field line performs during one poloidal turn[5]. Flux surfaces, for which the safety factor q can be written as m/n, where m and n denote integer numbers, are called rational surfaces. Only rational surfaces with small m and n play a significant role. On these surfaces, magnetic field lines close on themselves after m toroidal and n poloidal turns. A magnetic perturbation with a helicity equal to that of a rational surface inside the plasma is called resonant and may create a magnetic island at the position of this surface. Rational surfaces are therefore also referred to as resonant surfaces.

tearing mode

When an island is formed, the respective resonant surface is replaced by locally nested island flux surfaces. Figure 1.3 illustrates this topological change for a $q = 2/1$ perturbation in a circular plasma equilibrium. Field lines are torn apart and reconnected in a different way during the formation of a magnetic island that is therefore also called a tearing mode. The formation of magnetic islands requires non-zero plasma resistivity as the magnetic flux would be "frozen" to an ideal plasma with zero resistivity such that topological changes were prohibited. A detailed discussion of the formation and structure of magnetic islands is given in Section 2.5.

Inside a magnetic island, field lines wind helically around the island axis on the island flux surfaces, thus connecting plasma regions radially further inwards with ones further outwards.

[4] This is discussed in detail in Section 2.5 and illustrated in Figure 2.4.

[5] More details regarding the safety factor are found in Section 2.2.1.

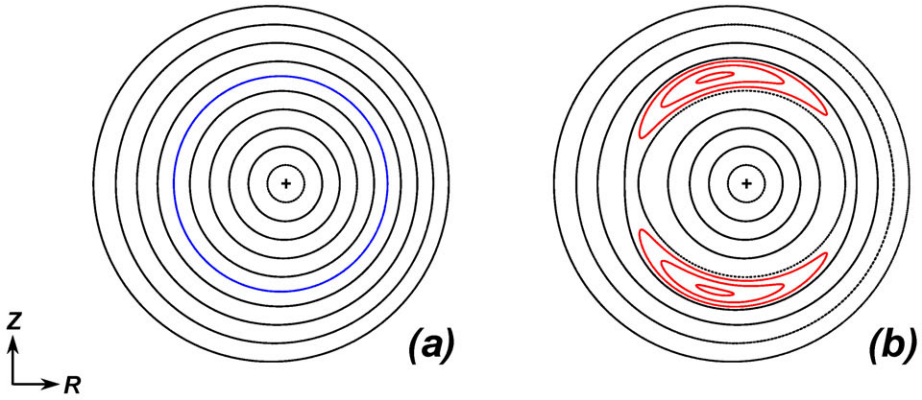

FIGURE 1.3. *The magnetic field structure of the circular plasma of the TEXTOR tokamak is depicted. Part* ***(a)*** *shows the flux surfaces in the unperturbed case. The* $^2/_1$ *resonant surface is marked in blue. Part* ***(b)*** *illustrates the magnetic topology after the formation of a* $^2/_1$ *magnetic island. The island magnetic surfaces are shown in red.*

Thus, parallel heat transport becomes possible around magnetic islands on these surfaces and a competition arises between the two heat transport channels perpendicular to the magnetic field lines across the magnetic island and parallel to the magnetic field lines around the island. The dominant contribution is essentially determined by the ratio between the island size, w, and the scale island size for temperature flattening, w_c, that depends on local equilibrium properties, the island mode numbers, and the heat diffusion anisotropy. In case parallel transport dominates, a flattening of the temperature profile results inside the magnetic island degrading the total energy confinement of the plasma. More details on heat transport across magnetic islands are given in Section 2.5.3.

temperature flattening

The flattening of the pressure inside magnetic islands can have a destabilizing effect, thus leading to further island growth. The reason is the bootstrap current that is connected to charged particles trapped to the outboard side of the torus by magnetic field inhomogeneities, which move on so-called banana orbits due to particle drifts. Charged particle motion in tokamaks is discussed in Section 2.3. As the bootstrap current is roughly proportional to the pressure gradient, a resonant helical lack current arises when the temperature profile flattens inside an island. This lack current acts as an additional island drive and increases the island size further. Such an island is called a neoclassical tearing mode (NTM). NTMs require a seed perturbation that already causes some temperature flattening to emerge. Details are discussed in Section 2.6. The driving mechanism of NTMs that depends very sensitively on the temperature distribution at the island is one of the topics investigated in this work. In some cases, periodic amplitude drops of NTMs have been observed experimentally (neoclassical tearing modes in the frequently interrupted regime, FIR-NTMs). A possible explanation for the phenomenon will be given in this work.

bootstrap current

NTMs

The simultaneous presence of several overlapping magnetic islands leads to a chaotic field structure in which flux surfaces dissolve. Magnetic field lines move randomly within such a volume called an ergodic layer as explained in Section 2.7 in detail[6]. Both, magnetic islands and ergodic layers lead to a degradation of the global plasma confinement properties through an enhanced radial transport.

ergodic layer

Neoclassical tearing modes limit the achievable pressure gradients in tokamak plasmas and can cause a rapid loss of the complete plasma confinement, a major disruption, which may damage the walls. The achievement of the design targets of the ITER tokamak requires among others a robust control of NTMs. For these reasons, a detailed understanding of NTMs is of great importance. It implies the development of accurate methods for the prediction of heat transport across magnetic islands and stochastic field layers and knowledge of the true heat diffusion anisotropy of fusion plasmas. These points will be addressed by the work at hand.

disruption

1.4. Aims of this Work

By modeling the anisotropic heat transport in magnetized plasmas numerically and comparing the results to analytical predictions and experimental measurements, this work tries to give answers to the following problems.

- It is investigated, if numerical heat transport simulations are possible with realistic heat diffusion anisotropies in toroidal plasma configurations without aligning the coordinate system exactly to the magnetic field lines. → Sections 4.2.2 – 4.4.4
- The mechanisms of heat transport across magnetic islands in cylindrical and toroidal geometries are addressed and it is investigated how well they are described by the analytical approximations found in literature. → Sections 5.1 – 5.4
- The dependency of the island drive of neoclassical tearing modes on the island size, w, and the scale island size for temperature flattening, w_c, is investigated and compared to analytical predictions. → Section 5.5
- An attempt is made to determine the heat diffusion anisotropy in experiments by comparing numerical simulations to experimental temperature measurements. The results are compared to classical analytical predictions. → Chapters 6 and 7
- Heat transport across stochastic field layers is examined and compared to the various transport regimes predicted by classical analytical theory. → Sections 8.1 and 8.2
- An explanation is given for the sudden amplitude drop of neoclassical tearing modes in the frequently interrupted regime. → Section 8.3

[6] The terms “ergodic layer” and “stochastic layer” are used synonymously in this work.

- It is considered, how the ergodization of the plasma boundary by resonant magnetic perturbation coils affects the temperature at the plasma boundary. → Section 8.4

1.5. Outline

The rest of this work is organized as follows. The theoretical background is given in Chapter 2. This includes a brief introduction to plasma fluid theory and an overview over plasma equilibria, heat transport in magnetized plasmas, magnetic islands, neoclassical tearing modes, and ergodic layers. Some experimental aspects relevant to this work are introduced in Chapter 3. The tokamak experiments TEXTOR and ASDEX Upgrade are briefly described, some experimental observations regarding neoclassical tearing modes and edge localized modes are reviewed, resonant magnetic perturbation coils are explained, and temperature measurement techniques are shown.

In Chapter 4, the physical, mathematical, and numerical model used in this work is covered. To be able to investigate heat transport across magnetic islands and stochastic field layers, a numerical code for precise computations of heat transport needed to be developed that is capable of treating realistic plasma parameters in real tokamak geometries. The enormous anisotropy of the heat diffusion tensor is a numerical challenge exclusively found in magnetized plasmas. Details are given on the numerical finite difference scheme that was used and on its implementation. Existing numerical codes that were used, e.g., for the determination of plasma equilibria are briefly introduced. Subsequently, the relevant coordinate systems are described and an overview over the most important physical assumptions that were made is given.

Chapter 5 contains the results obtained regarding heat transport across magnetic islands. Differences and similarities are highlighted between simulations performed in realistic toroidal geometries and simplified cylindrical geometry. The island drive of neoclassical tearing modes is investigated and compared to analytical theory.

In Chapters 6 and 7, comparisons of numerical simulations and measurements of the electron temperature at the tokamak experiments TEXTOR and ASDEX Upgrade are performed. This allows to determine the experimental value of the heat diffusion anisotropy.

Results obtained for heat transport across ergodic layers are presented in Chapter 8. Comparisons to classical analytical theories are made and a possible explanation for the physics of FIR-NTMs is given. The effect of plasma edge ergodization onto the pedestal temperature distribution is examined.

Chapter 9 summarizes the work and contains an outlook. In the Appendix, some additional details about the coordinate systems used in this work and on the implementation of the heat diffusion code are given. The list of references and the acknowledgments the author would like to make are found at the end of the work.

1.6. List of Publications

Parts of this dissertation have been published as articles in refereed journals and as conference contributions. The corresponding references are given below.

Refereed Journals

1. M. Hölzl, S. Günter, I. Classen, Q. Yu, TEXTOR Team, and E. Delabie. *Determination of the heat diffusion anisotropy by comparing measured and simulated electron temperature profiles across magnetic islands*. Nucl. Fusion **49**, 115009 (2009). doi:10.1088/0029-5515/49/11/115009.

2. M. Hölzl, S. Günter, and the ASDEX Upgrade Team. *Heat diffusion across magnetic islands and ergodized plasma regions in realistic tokamak geometry*. Phys. Plasmas **15**, 072514 (2008). doi:10.1063/1.2959138.

3. M. Hölzl, S. Günter, Q. Yu, and K. Lackner. *Numerical modeling of diffusive heat transport across magnetic islands and highly stochastic layers*. Phys. Plasmas **14**, 052501 (2007). doi:10.1063/1.2722980.

Workshops and Conferences

1. A. Runov, S. Kasilov, R. Schneider, O. Kalentyev, R. Zagorski, Y. Feng, S. Günter, M. Hölzl. *Edge transport in 3D magnetic geometries: physics and numerics.* 13^{th} European Fusion Theory Conference, Riga, Latvia (2009).

2. M. Hölzl, S. Günter, I. Classen, Q. Yu, and the TEXTOR Team. *Simulation of Heat Transport Across Magnetic Islands in TEXTOR*. 36^{th} EPS Conference on Plasma Physics, P1.183, Sofia, Bulgaria (2009).

3. M. Hölzl, S. Günter, and the ASDEX Upgrade Team. *Heat diffusion across magnetic islands and ergodized plasma regions in realistic tokamak geometry*. 35^{th} EPS Conference on Plasma Physics, P2.064, Crete, Greece (2008).

4. M. Hölzl, S. Günter, Q. Yu, and K. Lackner. *Numerical modeling of diffusive heat transport across magnetic islands and highly stochastic layers*. 2^{nd} International Workshop on Stochasticity in Fusion Plasmas, Jülich, Germany (2007).

5. Q. Yu, M. Hölzl, S. Günter, and K. Lackner. *Theoretical studies of diffusion across magnetic island and local stochastic magnetic field*. 2^{nd} International Workshop on Stochasticity in Fusion Plasmas, Jülich, Germany (2007).

Chapter 2.

Theoretical Background

This Chapter introduces the theoretical background for the work at hand. The derivation of plasma fluid equations and the properties of plasma equilibria are shown concisely. After that, we turn to the physical heat transport processes that act parallel and perpendicular to the magnetic field lines. The physics of magnetic islands, neoclassical tearing modes, ergodic layers, and edge localized modes are discussed successively. The outline is as follows:

Section 2.1 sketches the derivation of fluid equations starting from a kinetic plasma description and the steps that reduce the model to a one-fluid picture – magnetohydrodynamics (MHD). In the MHD picture, the plasma state is characterized by the spatio-temporal distributions of the fluid quantities density, velocity, temperature, and heat flux. The methods for the determination of plasma equilibria from the MHD model and the properties of these equilibria are discussed in Section 2.2.

MHD

Charged particle motion in the inhomogeneous tokamak field is discussed briefly in Section 2.3. Emphasis is put onto the trajectories of trapped particles that move on so-called banana orbits. It is explained, how the bootstrap current arises from trapped particle motion. There are many different physical processes that contribute to heat transport parallel and perpendicular to the magnetic field lines. The most important ones are discussed in Section 2.4 and the mathematical description of anisotropic heat transport in magnetized plasmas is given.

Internal or external resonant magnetic perturbations may change the equilibrium magnetic topology and lead to the formation of magnetic islands as discussed in Section 2.5. Temperature gradients are reduced within island flux surfaces due to the fast parallel transport which leads to a flattening of the temperature distribution at magnetic islands. The temperature flattening acts back on the island stability as the bootstrap current is perturbed. This perturbation constitutes a helical lack current that leads to further island growth. Magnetic islands dominated by this effect are called neoclassical tearing modes, they are discussed in Section 2.6. The formation of an ergodic field layer, i.e., a region with a chaotic magnetic field structure, due to overlapping magnetic islands, is covered in Section 2.7.

Contents

2.1. Plasma Fluid Equations

The state of a plasma may be described by distribution functions that specify the particle densities of each particle species in phase-space. The time-evolution of these distribution functions is given by the kinetic equation. Determining moments of the kinetic equation and applying an appropriate closure to the resulting system of equations results in a multi-fluid description that characterizes the plasma state by the spatial distributions and temporal dependencies of quantities like the particle densities and temperatures associated with the different particle species. Additional assumptions are required for the derivation of the magneto-hydrodynamic (MHD) model that describes the magnetized plasma as a single conducting fluid. The derivation of the

MHD model starting from the kinetic equation is sketched in the following. A more detailed derivation may for example be found in Reference [Fitzpatrick09].

2.1.1. Kinetic Equations

The plasma state can be described by microscopic distribution functions, $F_s(\mathbf{r},\mathbf{v},t)$, for each particle species s which specify the phase-space densities at a given position $\mathbf{r}$, velocity $\mathbf{v}$ and time t. Each particle is represented by a delta function of the respective distribution function in phase space. Particle conservation demands

$$\frac{dF_s}{dt} = \frac{\partial F_s}{\partial t} + \mathbf{v}\cdot\nabla_r F_s + \mathbf{a}_s\cdot\nabla_v F_s = 0, \tag{2.1}$$

where, ∇_r and ∇_v denote, respectively, the real space and velocity space grad-operators, q_s and m_s the charge and mass of a single particle of species s, and $\mathbf{a}_s = (q_s/m_s)(\mathbf{E}+\mathbf{v}\times\mathbf{B})$ its acceleration due to electrical and magnetic fields. Ensemble averaging[1] Equation (2.1) results in

$$\frac{\partial f_s}{\partial t} + \mathbf{v}\cdot\nabla_r f_s + \overline{\mathbf{a}_s}\cdot\nabla_v f_s = C_s(f), \tag{2.2}$$

where an overbar denotes ensemble averaging, $f_s = \overline{F_s}$ the ensemble averaged distribution function, and $C_s(f) = \overline{\mathbf{a}_s}\cdot\nabla_v\overline{F_s} - \overline{\mathbf{a}_s\cdot\nabla_v F_s}$ the collision operator for species s that depends on the distribution functions of all particle species. Overbars are omitted in the following for simplicity. Unlike the microscopic distribution functions, F_s, the macroscopic distribution function, f_s, is a smooth phase space function. Equation (2.2) can be simplified to the form

$$\frac{\partial f_s}{\partial t} + \nabla_r\cdot(\mathbf{v}f_s) + \nabla_v\cdot(\mathbf{a}_s f_s) = C_s(f) \tag{2.3}$$

exploiting $\nabla_v\mathbf{a}_s = 0$ and $\nabla_r\mathbf{v} = 0$.

2.1.2. Moment Equations

Moments of the distribution function are determined by integrating $f_s\mathbf{v}^k$ over velocity space, where k is a non-negative integer number and $\mathbf{v}^k$ denotes the k-fold dyadic product, $\mathbf{v}\otimes\mathbf{v}\otimes\cdots\otimes\mathbf{v}$. The first moments are the particle density, $n_s(\mathbf{r},t) = \int f_s(\mathbf{r},\mathbf{v},t)d^3\mathbf{v}$, the particle flux density, $n_s\mathbf{v}_s(\mathbf{r},t) = \int \mathbf{v}f_s(\mathbf{r},\mathbf{v},t)d^3\mathbf{v}$, the pressure tensor, $\hat{p}_s(\mathbf{r},t) = \int m_s\mathbf{w}_s\otimes\mathbf{w}_s f_s(\mathbf{r},\mathbf{v},t)d^3\mathbf{v}$, and the heat flux density, $\mathbf{q}_s(\mathbf{r},t) = \int \frac{m_s}{2}w_s^2\mathbf{w}_s f_s(\mathbf{r},\mathbf{v},t)d^3\mathbf{v}$. Here, $\mathbf{v_s}$ denotes the flow velocity of particle species s and $\mathbf{w}_s = \mathbf{v}-\mathbf{v_s}$ the particle velocity relative to the mean flow of species s. The (kinetic) temperature is defined as $T_s = p_s/n_s$.

[1] Ensemble averaging refers to the determination of the mean value of a quantity in the (infinite) set of possible states of the system.

Analogously, moments of the collision operator can be derived, which is approximated to be bi-linear in the distribution functions. The zero-moment of the collision operator vanishes due to particle conservation, whereas the first moment is the friction force, $\mathbf{F}_{ss'} = \int m_s \mathbf{v} C_{ss'} d^3\mathbf{v}$, particle species s experiences due to the presence of particle species s'. In total, species s experiences the force $\mathbf{F}_s = \sum_{s'} \mathbf{F}_{ss'}$ due to the interaction with all particle species. The second moment of the collision operator is the collisional energy moment, $W_{ss'} = \int \frac{m_s}{2} w_s^2 C_{ss'} d^2\mathbf{v}$. It measures the kinetic energy change of species s due to collisions with species s'. In total, species s experiences the energy change $W_s = \sum_{s'} W_{ss'}$. By multiplying Equation (2.3) by $\mathbf{v}^k$ and integrating it over velocity space, the moment respectively fluid equations

$$\frac{dn_s}{dt} + n_s \nabla \cdot \mathbf{v}_s = 0, \tag{2.4}$$

$$m_s n_s \frac{d\mathbf{v}_s}{dt} + \nabla \cdot \hat{p}_s - q_s n_s \left(\mathbf{E} + \mathbf{v}_s \times \mathbf{B}\right) = \mathbf{F}_s, \tag{2.5}$$

$$\frac{3}{2}\frac{dp_s}{dt} + \frac{3}{2} p_s \nabla \cdot \mathbf{v}_s + \hat{p}_s \nabla \mathbf{v}_s + \nabla \cdot \mathbf{q}_s = W_s \tag{2.6}$$

may be derived for each particle species s. Here, $d/dt = \partial/\partial t + \mathbf{v}_s \cdot \nabla$ denotes the convective (also substantial) derivative, i.e., the time-derivative in the co-moving frame of species s.

convective derivative

2.1.3. Braginskii Equations

An asymptotic closure to Equations (2.4) – (2.6) can be derived exploiting one of the two possible small parameters λ_{mfp}/L and ρ_L/L. Here, λ_{mfp} denotes the mean free path between collisions, L the length-scale of the system, and ρ_L the Larmor radius. The parameter, ρ_L/L, is adequate for magnetized plasmas that are of interest for this work. By the Chapman-Enskog method that is explained in Reference [Chapman53], a closed set of fluid equations, the Braginskii equations, can be derived for a collisional magnetized plasma [Braginskii65]. Explicit expressions for the right hand sides of Equations (2.5) and (2.6) as well as for the pressure tensor $\hat{p}_s$ and the heat flux density $\mathbf{q}_s$ are computed from the distribution function f which is expanded in the small parameter for this purpose. Although the derivation of the Braginskii equations are strictly valid for collisional plasmas only, comparisons to hybrid kinetic-fluid models revealed that only the sound wave dynamics are considerably modified. This renders the fluid approach reasonable also for "collision-less plasmas" provided the parallel sound wave dynamics are less important than the perpendicular Alfvén waves[2].

Braginskii equations

2.1.4. Magneto-Hydrodynamic Model

A normalization of the Braginskii Equations to typical values of the physical quantities clarifies the magnitudes of the various terms in each of the equations as it expresses them in terms

[2] An Alfvén wave is a special kind of wave that occurs in magnetized plasmas and involves field line oscillations.

of small parameters. Several different orderings between these parameters are possible. The MHD limit, which is of interest for the work at hand, corresponds to the assumption that fluid velocities are of the order of ion thermal velocities. Exploiting the small mass ratio between electrons and ions and assuming that electrons and ions move approximately together (strict quasi-neutrality) leads to the resistive MHD model which describes the plasma as a single fluid. An additional equation is required for the pressure to close the system of equations. Here, usually adiabatic behavior described by $d(p/n^\gamma)/dt = 0$ is assumed. The resistive MHD equations take the following form in a fixed frame:

quasi-neutrality
resistive MHD

$$\frac{\partial \rho_m}{\partial t} = -\nabla\cdot(\rho_m \mathbf{v}), \qquad \text{(continuity)} \qquad (2.7)$$

$$\frac{\partial \mathbf{v}}{\partial t} = -(\mathbf{v}\cdot\nabla)\mathbf{v} + \frac{1}{\rho_m}\left[(\nabla\times\mathbf{B})\times\mathbf{B} - \nabla p\right], \qquad \text{(momentum)} \qquad (2.8)$$

$$\frac{\partial p}{\partial t} = -(\mathbf{v}\cdot\nabla)p - \gamma p\nabla\cdot\mathbf{v} - \nabla\cdot\mathbf{q}, \qquad \text{(energy)} \qquad (2.9)$$

$$\frac{\partial \mathbf{B}}{\partial t} = \nabla\times(\mathbf{v}\times\mathbf{B} - \eta\nabla\times\mathbf{B}), \qquad \text{(Maxwell-Ohm)} \qquad (2.10)$$

The Maxwell-Ohm equation is formed from Faraday's law and Ohm's law. Here, η denotes the electrical plasma resistivity, $\rho_m = mn$ the mass density, and γ the ratio of the specific heats that is also called adiabaticity coefficient ($\gamma = 5/3$ for an ideal gas with three degrees of freedom). In addition, $\nabla\cdot\mathbf{B} = 0$ must be provided for by the initial conditions and is then maintained by Equation (2.10). If the plasma resistivity is neglected, Equations (2.7) – (2.10) are referred to as "ideal" MHD equations.

ideal MHD

2.2. Tokamak Equilibria

For the understanding of many plasma phenomena, it is sufficient to consider the effect of perturbations to plasma equilibria. Ideal stationary MHD equilibria can be determined from the ideal MHD equilibrium equations,

$$(\nabla\times\mathbf{B})\times\mathbf{B} - \nabla p = 0, \qquad (2.11)$$

$$\nabla\cdot\mathbf{B} = 0, \qquad (2.12)$$

which may be derived by neglecting any time-dependencies ($\partial/\partial t = 0$), plasma motion ($\mathbf{v} = 0$), heat-fluxes ($\mathbf{q} = 0$), and plasma resistivity ($\eta = 0$) in the MHD equations. Equation (2.11) describes a balance between the pressure of the plasma and the forces of the magnetic field. The most important properties of tokamak equilibria will be discussed in the following.

The main magnetic field component in tokamak plasmas is oriented in toroidal direction and is produced by external field coils. The toroidal magnetic field strength is proportional to $1/R$. In- and outboard sides of the torus are, thus, also referred to as high and low field sides.

high field side
low field side

aspect ratio

In a typical tokamak with an aspect ratio of about 3, the magnetic field strength at the plasma edge is twice as strong on the in- than on the outboard side. The aspect ratio denotes the ratio between the major radius, R_0, and the minor radius, a, of the plasma configuration.

major radius
minor radius

The distribution of the poloidal magnetic field component is determined by the toroidal plasma current that is driven mostly inductively in current tokamak experiments by a primary winding using the transformer principle. A plasma current can also be driven by resonant electromagnetic waves (→ Section 3.2.2) or by neutral beam injection. The bootstrap current that arises from trapped particles contributes to the toroidal plasma current as well. This current is explained in the context of charged particle motion in Section 2.3.

Tokamak equilibria are characterized by a set of nested magnetic flux surfaces as is illustrated in Figure 1.1. Due to the superposition of the toroidal and poloidal magnetic field components, every magnetic field line winds helically around the torus on a certain flux surface. The helicity of the field lines is different on each surface as discussed in the following Section. Equation (2.11) describes the balance $\mathbf{j} \times \mathbf{B} = \nabla p$ between magnetic and pressure forces. Obviously, $\mathbf{B} \cdot \nabla p = 0$ holds, which implies that no pressure gradients along magnetic field lines are present in ideal equilibria. Thus, the flux surfaces are surfaces of constant pressure, wherefore the pressure is denoted a flux function.

2.2.1. Safety Factor

Every magnetic field line winds helically around the torus on a certain flux surface. The safety factor, q, of the flux surface is defined as

$$q = \frac{d\Phi}{d\Psi}, \tag{2.13}$$

where Φ and Ψ denote the toroidal and poloidal magnetic fluxes associated with the respective surface. These are defined as the magnetic fluxes through the surfaces indicated in Figure 2.1. A constant is usually added to the poloidal flux such that it vanishes at the magnetic axis. A different sign for the safety factor may be found in literature depending on the definition of the positive coordinate directions. The safety factor may also be interpreted as the number of toroidal turns a field line performs during one poloidal turn. As the safety factor diverges at the plasma boundary of divertor configurations, the rotational transform, $\iota = q^{-1}$, is usually the better parameter to describe the field line helicity at the plasma edge. The magnetic shear is defined as $s = rq'/q$, where q' denotes the radial derivative of q.

rotational transform
magnetic shear

2.2.2. Shafranov Shift and Plasma Shaping

magnetic pressure

Both the plasma pressure and the "magnetic pressure", $B^2/(2\mu_0)$, raise so-called Hoop-forces directed outwards along the major radius. These need to be compensated by the interaction of the toroidal plasma current with an additional vertical magnetic field that is produced by external field coils. The additional field amplifies the poloidal magnetic field at the outboard

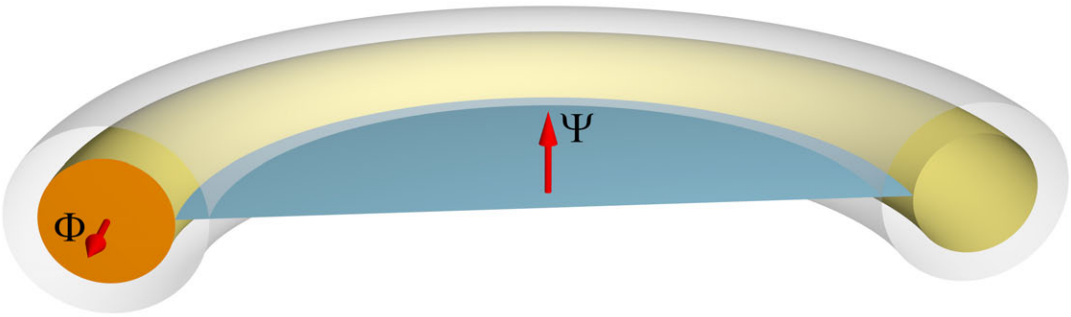

FIGURE 2.1. *For the magnetic flux surface shown in yellow, the toroidal magnetic flux, Φ, is defined as the magnetic flux that goes through the poloidal cross-section depicted in orange. The poloidal magnetic flux, Ψ, similarly, is defined as the magnetic flux through the blue surface.*

side. Thus, the distance between the magnetic flux surfaces is smaller on the out- than on the inboard side of the torus as seen in the equilibria of the ASDEX Upgrade (→ Figure 1.2) and TEXTOR tokamaks (→ Figure 1.3a). This effect is called Shafranov shift and is described by the Grad-Shafranov equation. For details refer, e.g., to References [Boyd03, Wesson04].

Shafranov shift
Grad-Shafranov equation

The magnetic flux surfaces of most tokamak experiments are not circular as the stability properties of shaped plasmas are more favorable ("plasma shaping"). Divertor plasmas[3], for example, are usually shaped triangularly to some degree. For the ASDEX Upgrade tokamak, the elongated and triangular shape of the plasma is shown in Figure 1.2. TEXTOR, in contrast to that, is a limiter tokamak[4] with circular flux surfaces (Figure 1.3a).

plasma shaping

2.2.3. Poloidal Mode Coupling

In toroidal plasma configurations with a shaped (non-circular) plasma cross-section, a magnetic perturbation with the poloidal mode number m and the toroidal mode number n couples inevitably with magnetic perturbations with different poloidal mode numbers. An m/n perturbation is coupled

- with $m\pm1/n$ sidebands due to toroidicity,
- with $m\pm2/n$ sidebands due to a vertical elongation, and
- with $m\pm3/n$ sidebands due to triangularity

of the plasma cross-section [Connor85, Fitzpatrick93, Coelho04]. The mode-coupling is illustrated by the Poincaré plot of Figure 2.2 which shows the magnetic topology that arises in

[3] In divertor configurations, the magnetic field lines outside the plasma separatrix intersect with the first wall in the so-called divertor region. Refer, e.g., to Reference [Wesson04] for details.

[4] In limiter configurations, the plasma edge directly strikes the first wall at the so-called limiter tiles.

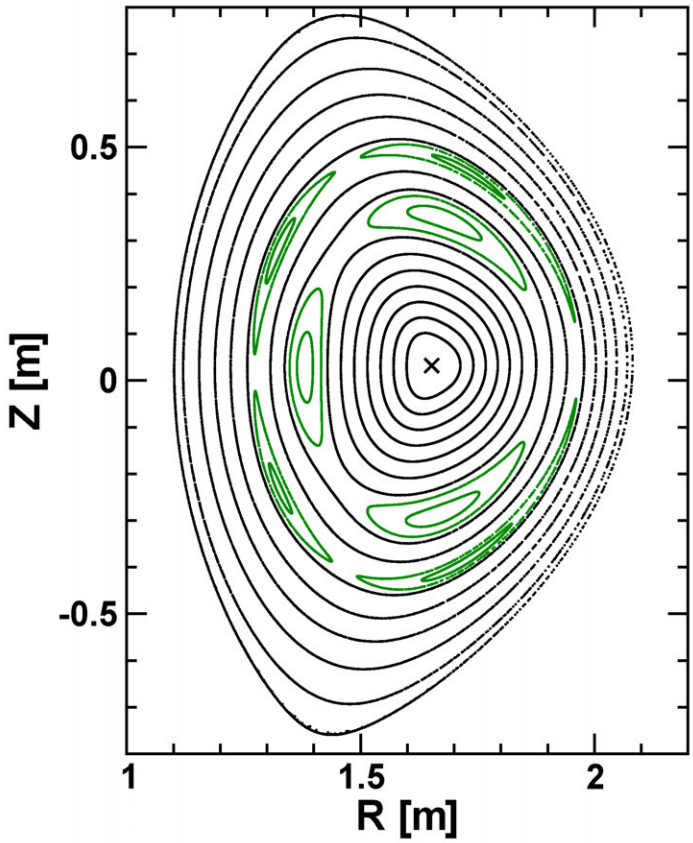

FIGURE 2.2. *In the magnetic field structure that results from a $^3/_2$ magnetic perturbation in ASDEX Upgrade, a $^4/_2$ magnetic island that is driven by the poloidal mode-coupling is visible besides the large $^3/_2$ island. Higher harmonics are much smaller and are not shown here.*

response to a strong single-helicity $^3/_2$ magnetic perturbation in ASDEX Upgrade. Clearly, a $^4/_2$ magnetic island is driven by the toroidicity-induced sideband in addition to the large $^3/_2$ magnetic island. In the presence of differential plasma rotation, the sidebands are, however, usually shielded by plasma currents such that the sidebands cannot produce magnetic islands.

2.2.4. Periodic Cylinder

To concentrate on the physical basics of heat transport across magnetic islands, the so-called "periodic cylinder" will be considered for the rest of Chapter 2. Magnetic field inhomogeneities due to the toroidal geometry of a tokamak are neglected in this model, as well as the Shafranov shift and plasma shaping. These simplifications are often used for analytical examinations ($\rightarrow$ e.g., Reference [Fitzpatrick95]). It has the advantage that magnetic islands remain a two-dimensional physical problem. Stochastic field layers produced by overlapping islands are, however, already a three-dimensional problem in the cylinder.

In analogy to toroidal geometries, the "major radius", R, of the cylinder is defined as the length of the cylinder in x-direction divided by 2π and the "toroidal angle", $\phi = x/R$, is usually used as coordinate along the cylinder axis. Any quantity Q must comply with the periodicity condition $Q(\phi) = Q(\phi + 2\pi)$. Unperturbed magnetic field lines may be described by

$$r \equiv r_0 \tag{2.14}$$

$$\theta = \theta_0 + \iota(r) \cdot \phi, \tag{2.15}$$

where the toroidal coordinate ϕ serves as a free parameter. The radial and poloidal coordinates are denoted r and θ. A normalized radial coordinate, $\rho = r/a$, may be introduced, where a denotes the minor radius of the plasma. In periodic cylindrical geometry, the safety factor may be written as

$$q = \frac{r}{R}\frac{B_\phi}{B_\theta}, \tag{2.16}$$

where r denotes the local minor radius, B_ϕ the "toroidal", and B_θ the poloidal magnetic field components.

2.3. Charged Particle Motion

This Section discusses the motion of individual charged particles in magnetic and electrical fields as far as it is relevant to the work at hand. First, the gyro-motion of charged particles in a homogeneous magnetic field is described in Section 2.3.1, then the particle drifts that arise from additional forces or magnetic field inhomogeneities are discussed in Section 2.3.2. Particle trapping due to the inhomogeneous magnetic field strength of toroidal confinement devices and the resulting bootstrap current are explained in Section 2.3.3

2.3.1. Gyro Motion

In a homogeneous magnetic field, the motion of a charged particle of mass m_s and charge q_s is determined by the equation of motion,

$$m_s \frac{\partial \mathbf{v}}{\partial t} = \frac{q_s}{c} \mathbf{v} \times \mathbf{B}, \tag{2.17}$$

where $F_L = (q_s/c)\mathbf{v} \times \mathbf{B}$ denotes the Lorentz force. When assuming $\mathbf{B} = B_z \mathbf{e}_z$ without loss of generality, Equation (2.17) can be split into the three Cartesian components. These coupled ordinary differential equations are then solved by the velocity components

$$v_x = v_\perp \sin(\omega_c t + \phi_0), \tag{2.18}$$
$$v_y = v_\perp \cos(\omega_c t + \phi_0), \tag{2.19}$$
$$v_z = v_{||}. \tag{2.20}$$

Here, $v_\perp$ denotes the velocity component perpendicular to the magnetic field and $v_{||}$ the (constant) parallel velocity component. This corresponds to a uniform motion parallel to the magnetic field and a circular gyro-motion in perpendicular directions with a constant perpendicular velocity. In total, the particle moves on a helical orbit following the magnetic field lines. The angular frequency of the gyro motion, the gyro-frequency, is given by

gyro-motion

gyro-frequency

$$\omega_c = \frac{q_s B}{m_s c} \tag{2.21}$$

and the gyro radius that is also called Larmor radius is given by

Larmor radius

$$\rho_L = \frac{m_s v_\perp}{q_s B}. \tag{2.22}$$

In a homogeneous magnetic field, the gyro-center of the particle motion exactly follows the magnetic field lines.

2.3.2. Particle Drifts

In the presence of an additional force, $\mathbf{F}_\perp$, perpendicular to the magnetic field lines, Equation (2.17) is amended by the respective force term on the right hand side. The solution to the equation of motion is then given by the gyro-motion described above superposed with an additional drift velocity,

drift velocity

$$\mathbf{v}_D = \frac{c\mathbf{F}_\perp \times \mathbf{B}}{q_s B^2}, \tag{2.23}$$

that is oriented perpendicular to, both, the magnetic field vector and the force[5]. As the particle drifts are usually much slower than the gyration, they can be imagined as a slow perpendicular motion of the gyro-center of the particle. Thus, the gyro-center does not follow the magnetic field lines exactly any more. Four especially important drifts shall be mentioned briefly. For more details on particle drifts, refer, e.g., to Reference [Boyd03].

- The charge-independent $E \times B$ drift is caused by a perpendicular electrical force, $\mathbf{F}_E = q_s \mathbf{E}_\perp$. It causes a motion of the complete plasma into the direction that is perpendicular to the electrical and magnetic fields. The $E \times B$ drift velocity is given by *E-cross-B drift*

$$\mathbf{v}_{E\times B} = \frac{c\mathbf{E}\times\mathbf{B}}{B^2}. \tag{2.24}$$

- The ∇B drift arises when the magnetic field strength has a gradient perpendicular to the magnetic field direction, which is always the case in toroidal configurations with helical field lines. The drift velocity is given by *grad B-drift*

$$\mathbf{v}_{\nabla B} = \frac{m_s c v_\perp^2}{2 q_s B^3}\mathbf{B}\times\nabla B. \tag{2.25}$$

  If a component of ∇B parallel to the magnetic field vector exists, it brings forth the so-called mirror force *mirror force*

$$m_s \frac{dv_{||}}{dt} = -\mu_s \nabla_{||} B, \tag{2.26}$$

  where $\mu_s = m_s v_\perp^2/(2B)$ denotes the magnetic moment which can be shown to be an approximately conserved quantity (adiabatic invariant). The mirror force leads to particle trapping as discussed in the subsequent Section.

- The curvature drift is caused by the centrifugal force, $\mathbf{F}_c = m_s v_{||}^2 \mathbf{R}_c/R_c^2$, that results from the particle motion along a curved magnetic field line. Here, $\mathbf{R}_c$ denotes the vector from the center of curvature to the particle position. The curvature drift is oriented perpendicular to both the magnetic field direction and to the vector $\mathbf{R}_c$. In toroidal magnetic confinement devices, particles therefore drift vertically upwards or downwards depending on the particle charge. The curvature drift velocity is given by *curvature drift*

$$\mathbf{v}_{curv} = \frac{m_s v_{||}^2}{q_s B^2}\frac{\mathbf{R}_c\times\mathbf{B}}{R_c^2}. \tag{2.27}$$

- The polarization drift is caused by a variation of the perpendicular electrical field with time. As the polarization drift is proportional to the particle mass, ions are affected *polarization drift*

[5] A parallel external force simply causes a parallel acceleration or deceleration of the respective particle.

polarization current

much stronger than electrons and give rise to the polarization current. The polarization drift velocity is given by

$$\mathbf{v}_{pol} = \frac{m_s c^2}{q_s B^2} \frac{d\mathbf{E}_\perp}{dt}. \tag{2.28}$$

2.3.3. Trapped Particles

The inhomogeneous magnetic field strength of toroidal configurations gives rise the mirror force as already mentioned in the previous Section. This force traps the fraction of particles with $v_{||}/v_\perp$ below the so-called reflection limit, $\sqrt{B_{max}/B_{min} - 1}$, to the low field side of the torus. Here, B_{min} and B_{max} denote the minimum and maximum magnetic field strengths on the considered flux surface. This may be understood in terms of the pitch angle, α, between the velocity vector and the magnetic field vector. All particles with a pitch angle larger than the threshold value,

pitch angle

$$\alpha_c = \arctan\left(1/\sqrt{B_{max}/B_{min} - 1}\right), \tag{2.29}$$

are repelled from the high field side.

Due to the curvature drift, charged particles drift vertically as discussed in the previous Section. In combination with the mirror force, the trapped particles are forced to move on so-called banana orbits. Figure 2.3 schematically shows an orbit of a trapped particle and its projection onto a poloidal cross section. In ASDEX Upgrade, the radial extent of ion banana orbits is typically between 7 mm and 3 cm [Poli02]. For the particles to be able to complete at least one drift cycle before being scattered by collisions, the plasma needs to be sufficiently collision-less which is the case for typical tokamak parameters already at temperatures above several hundred electron-volts [Wesson04]. The gyro-motion and the banana-orbits will play a role in the classical and neoclassical transport mechanisms discussed in Section 2.4.2.

banana orbit

In the presence of radial pressure gradients, the number of trapped particles, respectively their velocity, varies between different banana orbits. This leads to a net motion of particles in toroidal direction that is oriented contrarily for opposite charges. Through collisions, the passing (untrapped) particles come into equilibrium in velocity with the trapped particles giving rise to the toroidal bootstrap current. A heuristic derivation of the bootstrap current density, which is roughly proportional to the pressure gradient, is given in Reference [La Haye06]. For more details, refer, e.g., to Reference [Wesson04]. The bootstrap current plays an important role for the stability of neoclassical tearing modes as will be discussed in Section 2.6.

2.4. Heat Transport

Heat conductivity parallel and perpendicular to the magnetic field lines is determined by completely different physical processes which brings forth a large anisotropy. This may be de-

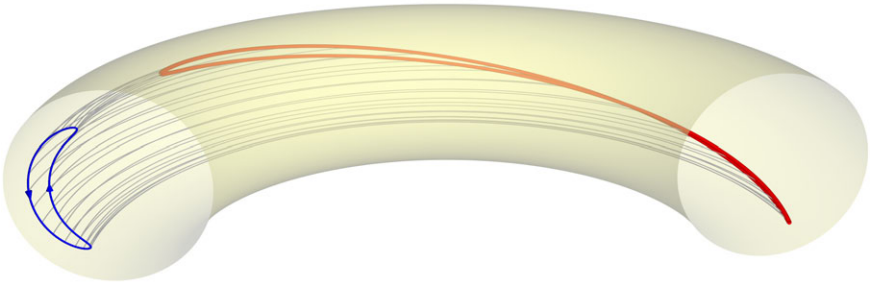

FIGURE 2.3. *The trajectory of a trapped particle in toroidal geometry is shown schematically. The orbit is depicted in red and its projection onto the poloidal cross-section at $\phi \equiv 0$ is shown in blue where the typical banana shape becomes visible. The gray lines illustrate the projection.*

scribed by an anisotropic heat diffusion tensor, $\hat{\chi}$, defined as the heat conduction tensor, $\hat{\kappa}$, divided by the particle density, n. Its component perpendicular to the magnetic field lines, $\chi_\perp$, is typically of the order 1 m^2/s in fusion plasmas [Callen92], while the component parallel to the magnetic field lines, $\chi_{||}$, is expected to be larger by a factor of typically $10^8 \ldots 10^{10}$. The heat diffusion anisotropy, $\chi_{||}/\chi_\perp$, plays an important role for the stability of neoclassical tearing modes (→ Section 2.6), but cannot directly be measured in the experiment. Thus, one aim of this work is to develop a method for the determination of the heat diffusion anisotropy by comparing temperature measurements at a magnetic island to numerical simulations. In the following, the heat diffusion equation and the physical processes contributing to heat transport perpendicular and parallel to the magnetic field lines will be discussed.

heat diffusion anisotropy

2.4.1. Heat Diffusion Equation

The heat transport parallel and perpendicular to the magnetic field lines in a magnetized plasma is described by the anisotropic heat diffusion equation,

heat diffusion equation

$$\frac{3}{2} n_e \frac{\partial T}{\partial t} + \nabla \cdot \mathbf{q} = P, \tag{2.30}$$

where

$$\begin{aligned} \mathbf{q} &= -n_e \hat{\chi} \cdot \nabla T \\ &= -n_e \left[\chi_{||} \nabla_{||} T + \chi_\perp \nabla_\perp T \right] \\ &= -n_e \chi_\perp \left[\chi \nabla_{||} T + \nabla T \right] \end{aligned} \tag{2.31}$$

denotes the heat flux density (often just heat flux in literature), n_e the electron particle density, P the energy source term, $\mathbf{b} = \mathbf{B}/B$ the magnetic field direction vector, $\nabla_{||} T = \mathbf{b}(\mathbf{b} \cdot \nabla T)$ the

heat flux density

parallel temperature gradient, $\nabla_\perp T = \nabla T - \nabla_{||} T$ the perpendicular temperature gradient, and

$$\chi = \frac{\chi_{||} - \chi_\perp}{\chi_\perp} \approx \frac{\chi_{||}}{\chi_\perp} \tag{2.32}$$

the heat diffusion anisotropy. For the toroidal coordinate systems required for tokamak computations, the heat diffusion equation needs to be expressed in tensor notation. The corresponding form may be found in Section 4.1.

Due to the efficient heat transport along magnetic field lines, the temperature distribution can be assumed to follow slow changes of the magnetic topology instantaneously. It is therefore reasonable to consider the steady state solution of the heat diffusion equation, where the time-derivative of the temperature is neglected. This assumption will be made in most parts of this work.

2.4.2. Perpendicular Heat Transport

This Section gives a brief overview of the physical processes contributing to cross-field heat transport. Perpendicular to the magnetic field lines, the Lorentz force constrains charged particles to gyro-orbits. The Larmor-radius of these orbits is $\rho_{L,e} \approx 0.1$ mm for electrons and $\rho_{L,D} \approx 7$ mm for deuterium ions assuming typical plasma parameters ($|\mathbf{B}| = 2$ T and $T_e = 5$ keV). When it comes to transport perpendicular to the magnetic field lines, the gyro-motion of trapped particles interrupted by collisions can be described as a random walk process with a step-size equal to the gyro-radius and a time-constant equal to the typical 90° scattering time by Coulomb collisions. This mechanism is called classical transport.

classical transport

In contrast to the simplified cylindrical model, magnetic field inhomogeneities and field line curvature play an important role in toroidal magnetic confinement devices. As discussed in Section 2.3, trapped particles move on so-called banana orbits which are typically between 7 mm and 3 cm wide for ions. The untrapped particles experience a similar radial displacement caused by the curvature drift. This displacement gives rise to a random walk process with a step-size equal to the width of the banana orbits. This mechanism is called neoclassical transport. As the banana-width is significantly larger than the radius of the gyro-orbits, this mechanism exceeds classical transport considerably.

neoclassical transport

Plasma distributions apart from thermodynamic equilibrium, i.e., from a spatially uniform Maxwell-Boltzmann velocity distribution, have free energy available to drive turbulence. Different types of turbulence are relevant for tokamak plasmas that are for example driven by the electron temperature gradient (ETG), the ion temperature gradient (ITG) or by trapped electrons (TEM). Turbulence accounts for the dominant cross-field heat transport contribution in most cases. Transport drops to the neoclassical level only in few cases: At the plasma boundary of H-mode plasmas, the ion transport is strongly reduced which leads to the formation of the characteristic pedestal with increased pressure gradients. Another example are internal transport barriers (ITBs) where the radial transport is reduced over a certain radial range of

turbulence

H-mode pedestal

the bulk plasma. In these cases, turbulence is believed to be suppressed by zonal flows which allows for the formation of steep temperature and density gradients.

2.4.3. Parallel Heat Transport

Parallel to the magnetic field lines, a random-walk process with a very large step size, which arises from the parallel motion of electrons interrupted by collisions, contributes to the transport. It can be described by Spitzer-Härm diffusivity [Spitzer53, Braginskii65], *Spitzer-Härm diffusivity*

$$\chi_{||}^{SH} = 3.16 \cdot v_{th,e} \cdot \lambda_e, \tag{2.33}$$

where $v_{th,e} = \sqrt{T_e/m_e}$ is the electron thermal velocity, λ_e the collisional electron mean free path, T_e the electron temperature, and m_e the electron mass. Equation (2.33) is valid in the collisional regime only, where λ_e is much smaller than the scale length L of temperature gradients. In tokamak plasmas, this is strictly the case only at the plasma boundary.

When the plasma is in the collision-less regime instead, heat transport is dominated by convection and the temperature becomes non-local. It has been shown that heat transport can still be described as a diffusive process when the so-called heat flux limit is applied [Malone75]. *heat flux limit* The heat flux is limited to a fraction of the value for free-streaming electrons in this model by adopting

$$\chi_{||}^{limit} = L \cdot v_{th,e} \tag{2.34}$$

wherever the heat flux according to Spitzer-Härm diffusivity would exceed this limit. Chang and Callen derived $L \approx 1/|k_{||}|$ with a theoretical approach, where $k_{||}$ denotes the parallel wave number [Chang92, Yu00]. Where the heat flux limit correction is applied in the work at hand, an analytical matching,

$$\chi_{||}^{hfl} = \frac{\chi_{||}^{SH}\chi_{||}^{limit}}{\chi_{||}^{SH} + \chi_{||}^{limit}}, \tag{2.35}$$

between the limits of Equations (2.33) and (2.34) is used as done similarly before, e.g., in References [Yu00, Tokar07].

2.5. Magnetic Islands

Due to the pronounced anisotropy between the heat diffusion coefficients parallel and perpendicular to the magnetic field lines, heat transport is very sensitive to changes in the magnetic topology. Magnetic islands, thus strongly influence heat transport. The formation of magnetic islands by reconnection of magnetic field lines is a resistive process [Furth63], which *reconnection* may be triggered by tearing mode instabilities or external resonant magnetic field perturba-

tions (RMPs). Inside a sufficiently large magnetic island, the temperature profile usually flattens which reduces the overall energy confinement of the plasma. Heat is transported around such an island within a narrow heat conduction layer that is located at the island separatrix. Periodic cylindrical geometry will be assumed in this Section to concentrate on the basic physical processes. First, tearing mode theory is briefly reviewed in Section 2.5.1, then the magnetic field structure of magnetic islands is discussed in Section 2.5.2 and the basic concepts of island heat transport are introduced in Section 2.5.3. Neoclassical tearing modes are discussed in Section 2.6.

2.5.1. Tearing Mode Theory

The time-evolution of tearing modes is discussed here only briefly. For a concise introduction to linear and nonlinear tearing mode theory, readers may refer to Reference [Fitzpatrick09].

The safety factor, q, is a function of the minor radius. A magnetic surface where the value of the safety factor becomes rational, $q = m/n$, is called a rational surface. Plasma resistivity can be shown to be important only in the immediate vicinity of these rational surfaces. It is therefore possible to solve the resistive MHD equations in a thin layer around a resonant surface located at $r = r_s$ and the ideal MHD equations in the rest of the plasma bulk. Subsequently, both solutions need to be matched continuously at the edges of their respective domains [Furth63]. This approach leads to a discontinuity in the radial derivative of the perturbed poloidal flux, $\tilde{\Psi}$. The normalized discontinuity of $\tilde{\Psi}'$ is given by the "tearing stability index",

tearing stability index

$$\Delta' = \left[\frac{1}{\tilde{\Psi}}\frac{d\tilde{\Psi}}{dr}\right]_{r_s-}^{r_s+}, \tag{2.36}$$

that depends on the plasma equilibrium and the position of the resonant surface only and can be interpreted as the available free energy. The growth rate, dw/dt, of the tearing mode is proportional to Δ' as described by the classical Rutherford equation [Rutherford73],

Rutherford equation

$$0.82\tau_r\frac{dw}{dt} = r_s^2\Delta', \tag{2.37}$$

where, $\tau_r = \mu_0 r_s^2/\eta$ denotes the current diffusion time. Thus, tearing modes with a positive tearing stability index are unstable as the magnetic configuration with the island is energetically more favorable than the unperturbed situation. Nonlinear investigations reveal that tearing modes saturate at a finite island width, w_{sat}, which is reached at $\Delta'(w) = 0$, where

$$\Delta'(w) \approx \Delta'\left[1 - \frac{w}{w_{sat}}\right]. \tag{2.38}$$

Classical tearing modes are linearly unstable, if $\Delta'(w = 0) > 0$ and would therefore in practice

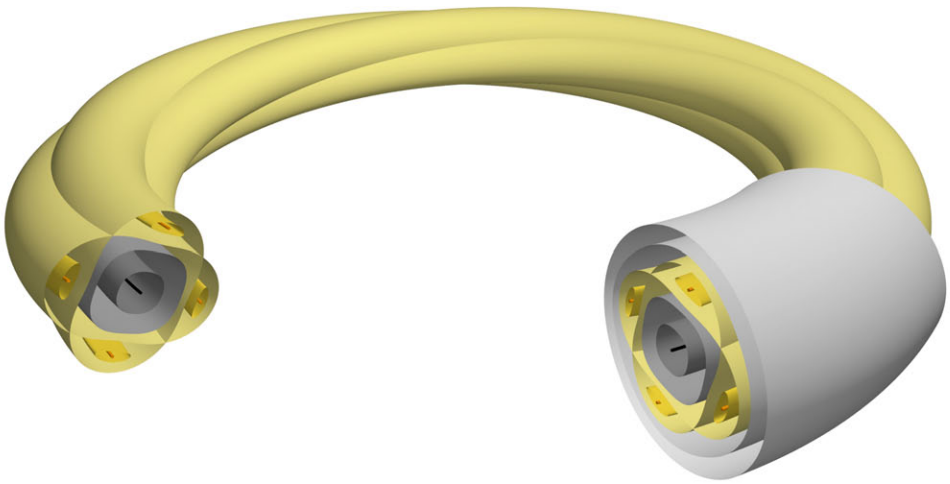

FIGURE 2.4. *The flux surfaces of a $4/3$ magnetic island in a circular plasma configuration are plotted. The island constitutes a helical flux tube that closes on itself after four toroidal and three poloidal turns.*

always be triggered, as an arbitrarily small resonant perturbation is sufficient for that. In tokamak plasmas with a safety factor $q_{95} \gtrsim 3$ close to the plasma boundary and a safety factor at the magnetic axis around unity, essentially all tearing modes are stable[6].

A more precise description of the tearing mode evolution that includes the local plasma properties is given in Reference [Wesson04]. Classically stable tearing modes can be destabilized by helical perturbations of the bootstrap current. These modes are called neoclassical tearing modes and are discussed in Section 2.6.

2.5.2. Field Structure

An m/n magnetic island at the $q = m/n$ resonant surface can be imagined as a helical flux tube which closes on itself after m toroidal and n poloidal turns. The three-dimensional structure of a magnetic island is illustrated in Figure 2.4, where the flux surfaces of a $4/3$ magnetic island in a toroidal plasma configuration with a circular cross-section are depicted. When an island arises, the resonant magnetic flux surface is replaced by locally nested island magnetic flux surfaces and the axisymmetry of the tokamak equilibrium is destroyed. The magnetic axis of the flux tube is referred to as the island O-point and the outermost flux surface of the island is called the island separatrix as labeled in Figure 2.5. The position where the radially inner and outer branches of the separatrix intersect is called X-point.

O-point
island separatrix
X-point

In the following, the trajectory of a magnetic field line at a magnetic island will be considered qualitatively. For this investigation, we assume that the safety factor, q, and its radial

[6]The safety factor at the flux surface that corresponds to 95% of the toroidal flux is commonly denoted by q_{95}.

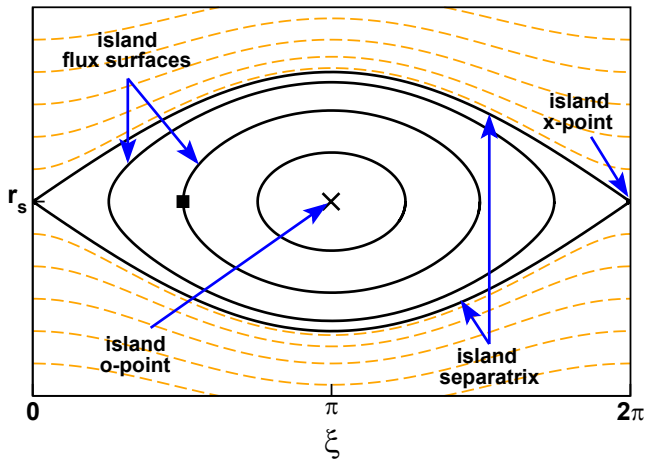

FIGURE 2.5. *A resonant magnetic perturbation may lead to the formation of a magnetic island at the resonant surface of the perturbation. Field lines wind helically around the island magnetic axis within island flux surfaces. The outermost surface is called the island separatrix. The intersection of the separatrix with the resonant surface is denoted X-point. The island width denotes the maximum radial extent of the island separatrix.*

derivative, dq/dr, are positive and that the toroidal magnetic field is oriented in positive ϕ-direction. It is convenient to introduce the coordinate

$$\xi = \theta - \frac{n}{m}\phi, \tag{2.39}$$

which allows to identify any unperturbed field line on the $q = {}^{m}/_{n}$ resonant surface uniquely by specifying the values of

$$r = r_s, \tag{2.40}$$
$$\xi = \text{const.} \tag{2.41}$$

At first, we consider the equilibrium configuration. The B_ξ component of the magnetic field vanishes at the resonant surface as the coordinate system is aligned to the helicity of the magnetic field lines on this surface. Due to the magnetic shear, B_ξ is oriented in positive ξ-direction at $r < r_s$, which means that the value of the coordinate ξ increases when moving along a magnetic field line in positive ϕ-direction. For $r > r_s$, B_ξ is oriented in negative ξ-direction such that ξ decreases when moving along a field line in positive ϕ-direction.

A magnetic field perturbation of the form $\tilde{\mathbf{B}} = \nabla\phi \times \nabla\tilde{\Psi}$, where $\tilde{\Psi}(r,\xi) = \tilde{\Psi}_0(r)\sin(m\xi)$, denotes the perturbed poloidal magnetic flux associated with a resonant magnetic perturbation (RMP). It is constant along the trajectory of an unperturbed field line on the resonant

magnetic surface. Thus, after many toroidal turns even a small perturbation amplitude causes a significant excursion of magnetic field lines close to the resonant surface. If the value of $\tilde{\Psi}_0(r)$ respectively $\tilde{B}_{r,0}(r)$ does not change its sign at the resonant surface, a magnetic island is formed. Otherwise, an ideal mode arises that does not change the magnetic topology but only deforms the magnetic flux surfaces.

The trajectory of the magnetic field line that passes through the position $r = r_s$ and $\xi = \xi_0$, where $0 < \xi_0 < \pi$, will be discussed qualitatively in the following. In Figure 2.5, such a position is marked by a solid square. The field line slowly drifts radially outwards due to the radial magnetic field perturbation and additionally moves towards larger values of ξ because of the magnetic shear. For $\xi > \pi$, the radial magnetic perturbation has the opposite sign such that the field line drifts radially inwards now and reaches the resonant surface again at $\xi = 2\pi - \xi_0$. An analogous excursion radially inwards from the resonant surface follows before the field line reaches its starting position again. The field line has performed a full turn around the island magnetic axis on its island flux surface just like a field line in an unperturbed tokamak configuration winds helically around the magnetic axis on its respective flux surface. Consequently, an island safety factor q_{isl} may be defined that gives the field line helicity with respect to the magnetic island.

Thus, we have seen that field lines at magnetic islands connect positions with different radial locations similar to a short-circuit. This renders heat transport around the magnetic island possible along magnetic field lines which may lead to a flattening of the temperature profile inside the islands as discussed in detail in Section 2.5.3.

Analytical theory usually introduces the island flux label Ω as an island coordinate that takes a value of -1 at the island O-point and a value of $+1$ at the separatrix. With the "constant $\tilde{\Psi}$ approximation", $\tilde{\Psi}_0 \equiv$ const, the island width w in periodic cylindrical geometry may be expressed analytically by

$$w = 4q_s \sqrt{\frac{\tilde{\Psi}_0}{r_s B_\phi \left[\partial q/\partial r\right]_{r=r_s}}}, \tag{2.42}$$

where q_s denotes the value of the safety factor at the resonant surface, B_ϕ the toroidal magnetic field component and r_s the value of the minor radius at the resonant surface [Fitzpatrick95].

2.5.3. Heat Transport Across Islands

For typical plasma parameters, the temperature distribution inside the separatrix of an island flattens in the absence of local heat sources. This can be observed from the experiment using electron cyclotron emission spectroscopy (ECE) which is capable of measuring the local electron temperature with a high temporal resolution while the island rotates around the torus (→ Section 3.5 for details on ECE measurements). Theoretical investigations for heat transport across magnetic island layers have been performed, e.g., by Scott [Scott85] and Fitzpatrick [Fitzpatrick95].

ECE

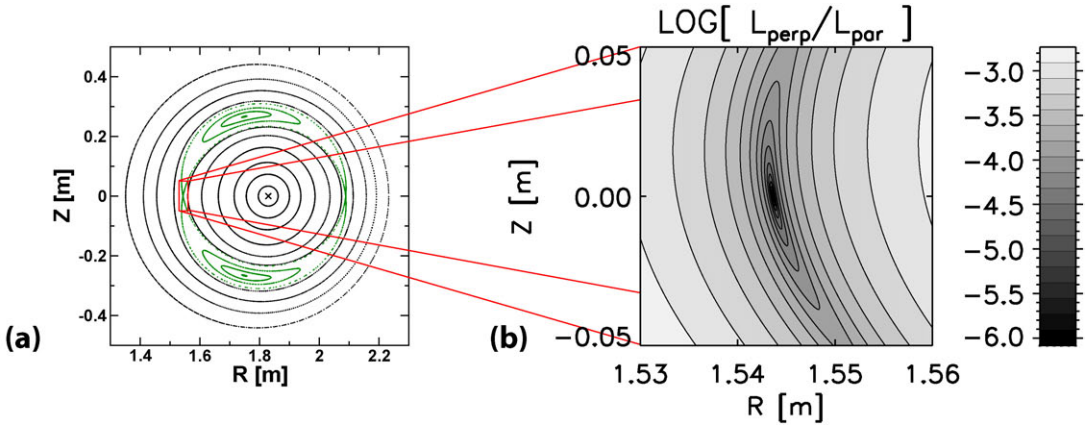

FIGURE 2.6. *The position of a magnetic field line relative to an $^m/_n$ magnetic island changes by a distance $L_\perp$ after m toroidal turns whereas the parallel distance along the field line is approximately $L_{||} = 2\pi m R_0$.*
*Part **(a)** of the figure shows a Poincaré plot of a $^2/_1$ magnetic island in TEXTOR. Part **(b)** shows a contour plot of the ratio $L_\perp / L_{||}$ for the region around the X-point that is indicated by the red box in the Poincaré plot. The ratio between the two length scales drops by several orders of magnitude in the vicinity of the X-point. This effect is called field line stagnation.*

Field lines in the island region wind helically around the magnetic island, thus connecting regions closer to the hot plasma core with regions located further outwards. The distance from the inboard side of a magnetic island to its outboard side is, however, much longer parallel to magnetic field lines than perpendicular to them. As, on the other hand, transport along magnetic field lines is much faster than perpendicular to them (→ Section 2.4), a competition between both heat transport mechanisms arises.

heat flux competition

If the heat diffusion anisotropy is large enough, parallel transport dominates in a region around the island O-point and the temperature gets constant within each island flux surface, there. In the absence of local heat sources, the temperatures of the different flux surfaces equalize and the temperature distribution flattens in the island O-point region. Heat is then transported around the island O-point on flux surfaces close to the island separatrix instead of just radially across the island. Local heat sources inside the magnetic island may result in a local temperature peaking around the island due to confining properties of the nested island flux surfaces.

temperature peaking

field line stagnation

On island flux surfaces close to the island separatrix, field line stagnation occurs as illustrated in Figure 2.6: Field lines advance much slower on their way around the island in the vicinity of the island X-point which leads to increased values of the island safety factor close to the island separatrix. The distance around the island along magnetic field lines is increased significantly, which renders parallel heat transport less efficient, there.

Consequently, temperature flattening first arises close to the island O-point and successively

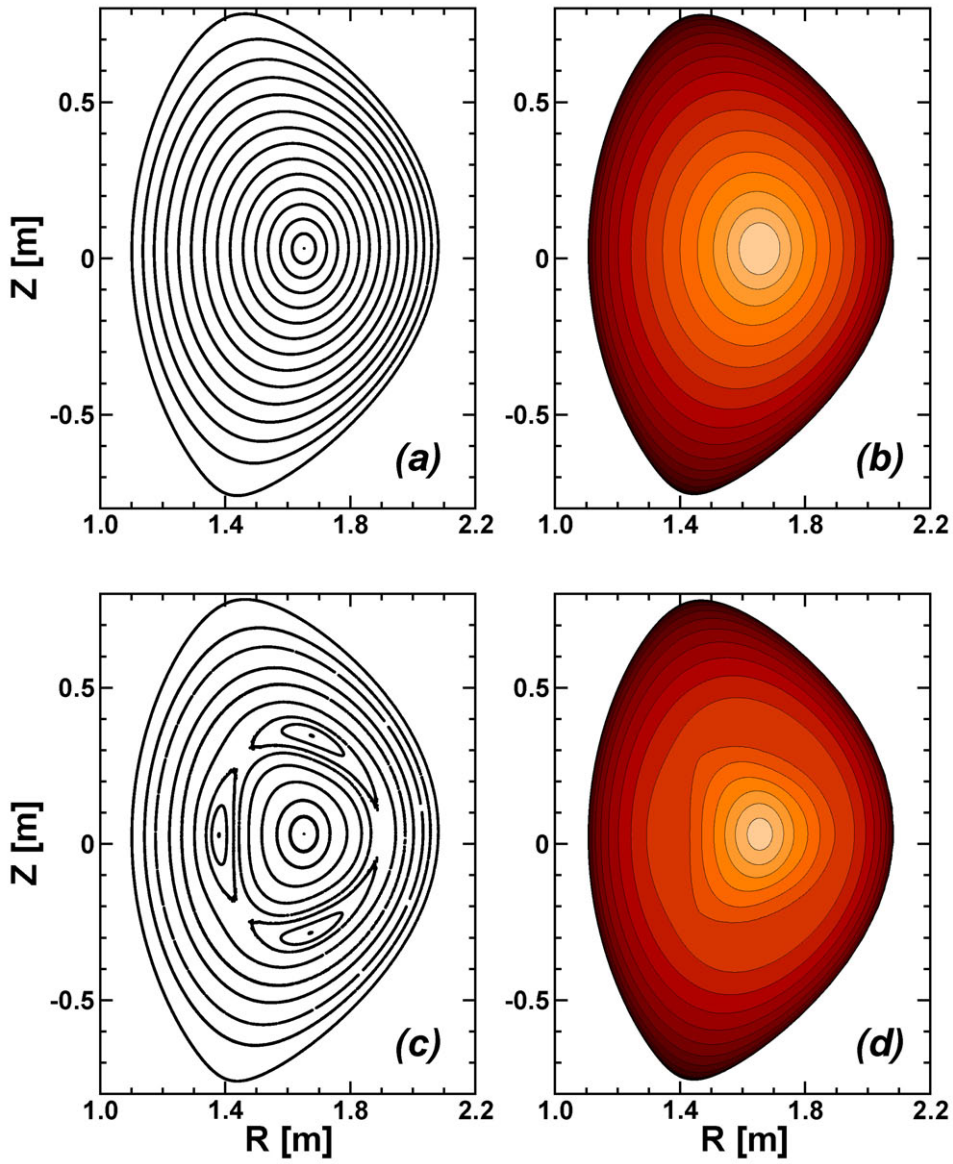

FIGURE 2.7. *Numerical results for the temperature flattening caused by a* $3/2$ *magnetic island in ASDEX Upgrade geometry at a heat diffusion anisotropy of* 10^9 *are shown. Figures* ***(a)*** *and* ***(b)*** *correspond to the Poincaré plot of the magnetic field structure in the unperturbed case and the corresponding temperature distribution, whereas Figures* ***(c)*** *and* ***(d)*** *show the perturbed case with a large* $3/2$ *magnetic island present. The temperature profile is flattened in the island region.*

extends towards the island separatrix for increasing heat diffusion anisotropies or increasing island sizes. In return, the region with non-zero parallel temperature gradients located around the island separatrix, which is called the heat conduction layer, narrows gradually with increasing $\chi_{||}/\chi_{\perp}$. The degree of flattening may be described by one single parameter: The ratio between the island width, w, and the scale island width for temperature flattening,

$$w_c = \left(\frac{\chi_{||}}{\chi_{\perp}}\right)^{-1/4} \left(\frac{8R_0 q}{n\,(\partial q/\partial r)}\right)^{1/2}. \tag{2.43}$$

Here, R_0 denotes the distance of the magnetic axis from the torus axis (major radius) and n the toroidal mode number of the resonant magnetic field perturbation. According to Fitzpatrick's analytical investigations, a significant flattening may not be expected unless $w/w_c \gtrsim 1$. Similar processes apply for density transport, but as the scale island width for density flattening, $w_{c,\rho}$, is usually much larger than w_c, the density flattening is less pronounced and can be neglected in most cases.

The effect of an island on the temperature distribution is shown in Figure 2.7. Parts (a) and (b) of the Figure show a Poincaré plot of an unperturbed ASDEX Upgrade equilibrium and the corresponding temperature distribution, respectively. Parts (c) and (d) contain the same data but for a large $3/2$ magnetic island present in the plasma. The temperature distribution, which was computed for a heat diffusion anisotropy of $\chi_{||}/\chi_{\perp} = 10^9$, shows a flattened temperature profile inside the island.

The heat flux across a magnetic island layer can be visualized by heat flux streamlines which give the trajectories of "heat test elements". Figure 2.8 shows projections of heat flux streamlines onto a poloidal cross section, i.e., onto a $\phi = \text{const}$ surface. For this Figure, a $4/3$ magnetic island case is computed in cylindrical geometry[7] and the streamlines are traced using a predictor-corrector scheme.

2.6. Neoclassical Tearing Modes

NTMs

Neoclassical tearing modes (NTMs) are a high-pressure phenomenon that can give rise to magnetic island growth although the plasma is stable to classical tearing modes [Carrera86, Fitzpatrick95, La Haye06, Hender07]. NTMs are destabilized by a helical perturbation of the bootstrap current at an initial seed island. The bootstrap current arises in tokamak plasmas due to particle trapping and particle drifts as discussed in Section 2.3. It is roughly proportional to the pressure gradient which means that NTMs become more likely when the normalized plasma beta,

seed island

plasma beta

$$\beta_N = \frac{aB_t}{I_p}\beta, \tag{2.44}$$

[7] In toroidal geometry, the heat flux streamlines are qualitatively similar. However, the three-dimensionality of the problem renders a corresponding Figure significantly less intuitive to read.

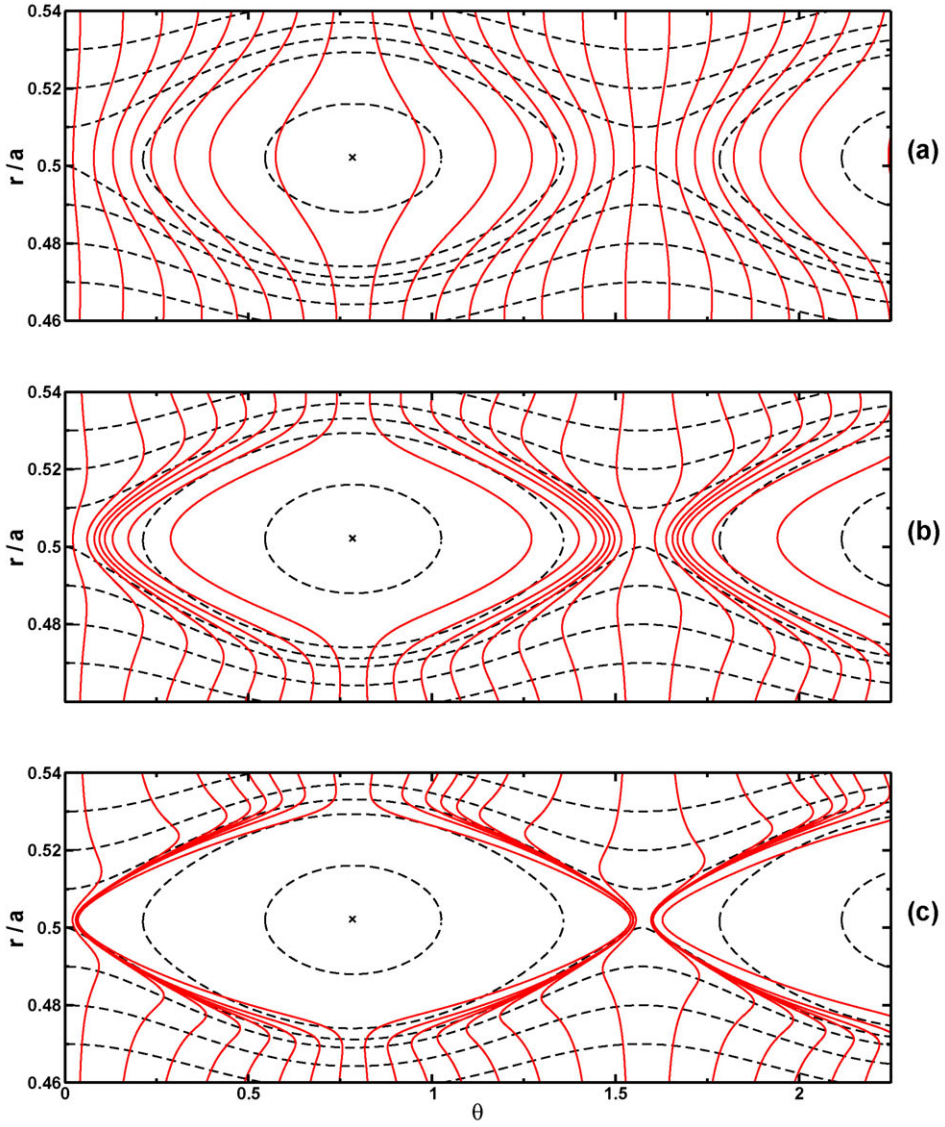

FIGURE 2.8. *Heat transport across a magnetic island layer in periodic cylindrical geometry is illustrated. The black dashed lines show a Poincaré plot of the magnetic field structure, while the red solid lines are heat flux streamlines. Parts* ***(a)****,* ***(b)****, and* ***(c)****, respectively, show results for* $w/w_c = 1.3$, 2.0, *and* 3.0.

rises. Here,

$$\beta = \frac{2\mu_0}{B_0^2}\langle p \rangle \tag{2.45}$$

denotes the ratio between the volume-averaged plasma pressure, $\langle p \rangle$, and the magnetic pressure, $B_0^2/(2\mu_0)$. As a result, neoclassical tearing modes seriously limit the maximum achievable pressure gradients of tokamak plasmas and can even lead to major disruptions.

NTMs are meta-stable modes that they can only emerge from a sufficiently large initial perturbation. The non-linear time-evolution of a classical tearing mode is described by the Rutherford equation as explained in Section 2.5.1. The evolution of neoclassical tearing modes is, accordingly, explained by a modification of the equation,

Rutherford equation

$$\frac{\tau_R}{r^2}\frac{dw}{dt} = \Delta' + \varepsilon^{1/2}\frac{L_p}{L_q}\frac{\beta_p}{w}, \tag{2.46}$$

where the driving term due to the helical bootstrap current perturbation is included. Here, τ_R denotes the local resistive time scale from Spitzer resistivity, r the minor radius, w the island size, Δ' the classical tearing stability index, $\varepsilon = r/R$ the local inverse aspect ratio, $L_p = -p/(dp/dr)$ the pressure gradient length, $L_q = q/(dq/dr)$ the magnetic shear length, $\beta_p = \langle p \rangle/(B_\theta^2/2\mu_0)$ the poloidal plasma beta, $\langle p \rangle$ the volume-averaged plasma pressure, B_θ the poloidal magnetic field strength, and μ_0 the magnetic constant.

Without additional stabilizing effects, any m/n magnetic island would be linearly unstable according to Equation (2.46) and could be triggered by an arbitrarily small initial perturbation. As this is obviously not the case in the experiment, stabilizing small island effects are missing in Equation (2.46) that negate the destabilizing contribution from the bootstrap current perturbation at small island sizes. The most important small island effects are the transport threshold, i.e., the incomplete flattening of the temperature inside small islands and the polarization threshold caused by the ion polarization current that arises from the electric field varying with time due to the island rotation relative to the plasma. Both lead to a critical seed island size below which no neoclassical growth arises such that too small initial islands decay away. With the mentioned small island effects included, the modified Rutherford equation can be written in the form

small island effects

transport threshold

polarization threshold

$$\frac{\tau_R}{r^2}\frac{dw}{dt} = \Delta' + \varepsilon^{1/2}\frac{L_p}{L_q}\frac{\beta_p}{w}\left[\frac{w^2}{w^2 + w_d^2} - \frac{w_{pol}^2}{w^2}\right]. \tag{2.47}$$

The terms in the brackets correspond to the transport and polarization threshold corrections. Here, $w_d \approx 1.8 w_c$. The transport threshold term is investigated numerically in Section 5.5 and a correction factor to the analytical term is derived.

The characteristic dependence of the island growth rate on the island size according to Equation (2.47) is illustrated in Figure 2.9. One case is plotted where the NTM is stable

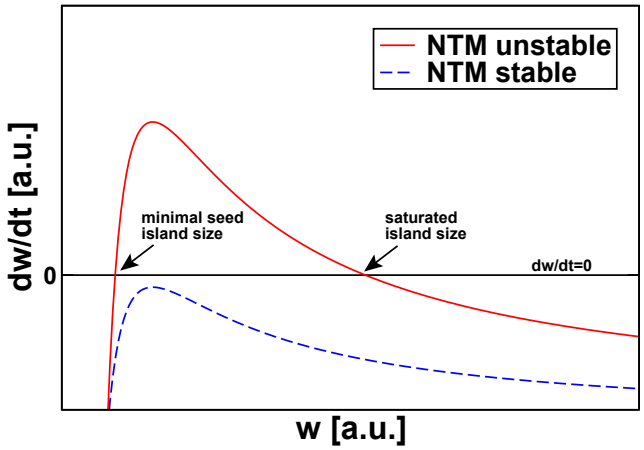

FIGURE 2.9. *The growth rate, dw/dt of a neoclassical tearing mode is plotted versus the island size. Two cases are show, one for an NTM that is stable independent of the initial island size (dashed curve) and a second one for an NTM that requires a finite seed island size to emerge and grow to its saturated island size (solid curve).*

(dashed curve), i.e., the growth rate is always negative. The solid curve shows a case where the NTM is linearly stable but non-linearly unstable. There, the unperturbed state is metastable and needs to be perturbed by a sufficiently large seed island to cause NTM growth. The left zero crossing of the curve determines the minimum seed island size required to trigger the NTM while the right zero crossing gives the saturated island size to which the NTM grows non-linearly. NTMs are explained from the experimental point of view in Section 3.2.

2.7. Stochastic Magnetic Field Layers

Helical magnetic perturbations may produce magnetic islands at the respective resonant surfaces. If these islands become large enough such that they overlap, the island magnetic flux surfaces are (partly) destroyed and a region is produced that is called an ergodic or stochastic layer [8]. The trajectories of magnetic field lines within such a layer become chaotic. Figure 2.10 shows a Poincaré plot of an ergodic region produced by two overlapping $3/2$ and $4/3$ magnetic islands in ASDEX Upgrade geometry. The degree of island overlapping is characterized by the so-called Chirikov parameter, σ_{Ch} [Chirikov79, Ghendrih96]. For the example of two $3/2$ and $4/3$ magnetic islands, this parameter is simply given by the average value of the

ergodic layer

Chirikov parameter

[8] Ergodization can also arise due to the coexistence of a magnetic island with an ideal mode with a different helicity. An ideal mode is a magnetic perturbation for which $\tilde{\Psi}_0(r)$ changes its sign at the resonant surface such that flux surfaces are only deformed. Refer to Section 2.5.2 for details.

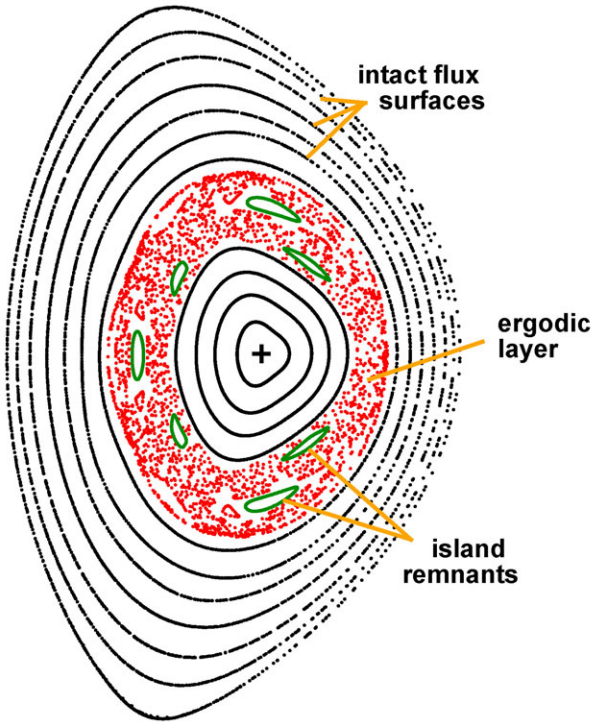

FIGURE 2.10. *The Poincaré plot shows an ergodic layer produced by two overlapping $3/2$ and $4/3$ magnetic islands with a Chirikov-parameter $\sigma_{Ch} = 1.6$. Some remnants of the flux surfaces of both magnetic islands are visible.*

island widths divided by the distance between the respective resonant surfaces,

$$\sigma_{Ch} = \frac{(w_{3/2} + w_{4/3})/2}{r_{3/2} - r_{4/3}}. \tag{2.48}$$

Here, $w_{m/n}$ and $r_{m/n}$, respectively, denote the island width and the minor radius corresponding to the m/n resonant surface. The chaotic trajectories of magnetic field lines within an ergodic layer result in a parallel contribution to the radial heat transport. For sufficiently large heat diffusion anisotropies, this leads to a flattening of the temperature profile in the ergodic region. The effect of ergodization onto the resonant bootstrap current perturbations of the individual islands, i.e., the neoclassical contribution to the island drive, will be examined in Section 5.5.

Extensive analytical work has been done, e.g., by Rechester and Rosenbluth [Rechester78], Kadomtsev and Pogutse [Kadomtsev79], Stix [Stix78], and Krommes et. al. [Krommes83] regarding diffusion heat transport across highly stochastic layers. A comprehensive review was written by Liewer [Liewer85]. Krommes et. al. identified three different sub-regimes of the collisional regime, where the fluid picture used in this work is valid. They are separated

by the ordering of the characteristic electron diffusion times

$$\tau_{||} = L_0^2/\chi_{||}, \tag{2.49}$$
$$\tau_k = L_k^2/\chi_{||}, \tag{2.50}$$
$$\tau_\perp = 1/(k_\perp^2 \chi_\perp). \tag{2.51}$$

With decreasing collisionalities, the regimes are called fluid regime ($\tau_\perp < \tau_{||} < \tau_k$), Kadomtsev-Pogutse regime ($\tau_{||} < \tau_\perp < \tau_k$), and Rechester-Rosenbluth regime ($\tau_{||} < \tau_k < \tau_\perp$). The diffusion times correspond to the characteristic length scales L_0, L_k and $1/k_\perp$, which are

$$L_0 \approx qR_0, \qquad \text{(quasi-linear auto-correlation length)} \tag{2.52}$$
$$L_k \approx \left[L_s^2/(k_\perp^2 D_M)\right]^{1/3}, \qquad \text{(Kolmogorov length)} \tag{2.53}$$
$$D_M = L_0 \sum_{\mathrm{m,n}} \left(B_{r,m/n}/B_{\phi,0}\right)^2, \qquad \text{(magnetic diffusion coefficient)} \tag{2.54}$$
$$L_s = Rq^2/(rq'), \qquad \text{(magnetic shear length)} \tag{2.55}$$
$$1/k_\perp \approx r/m. \qquad \text{(characteristic perpendicular wave length)} \tag{2.56}$$

Here, the radial component of the m/n magnetic perturbation, $B_{r,m/n}$, the perpendicular wave vector of the perturbations, $k_\perp \approx m/r$, the safety factor, q, and its radial derivative, q', were used. The sum in Equation (2.54) must be carried out over all locally resonant m/n magnetic perturbations. The increase, χ_r^+, of the radial heat diffusivity, $\chi_r = \chi_\perp + \chi_r^+$, in these subregimes is

$$\chi_{r,fl}^+ = D_M \chi_{||}/L_0, \qquad \text{(fluid regime)} \tag{2.57}$$
$$\chi_{r,KP}^+ = D_M (\chi_\perp \chi_{||})^{1/2} k_\perp, \qquad \text{(Kadomtsev-Pogutse regime)} \tag{2.58}$$
$$\chi_{r,RR}^+ = D_M \chi_{||}/L_k. \qquad \text{(Rechester-Rosenbluth regime)} \tag{2.59}$$

In the limit of small w/w_c, an analytical expression derived in Reference [Yu06] corrects the fluid regime prediction by about a factor of $1/2$ for the case considered in Section 8.2 in which a comparison of numerical simulations to these stochastic transport theories will be given.

Chapter 3.

Experimental Background

This Chapter introduces experimental background relevant for the rest of the work. First, the tokamak devices that are relevant for the further investigations are briefly described in Section 3.1. Then, neoclassical tearing modes (NTMs) are addressed in Section 3.2. The pressure gradient limit caused by these modes and the confinement degradation they induce are discussed. It is shown, that NTMs arise from seed islands which are driven by MHD activity in most cases. The frequently interrupted regime of neoclassical tearing modes is presented and the suppression of NTMs by local heating and current drive is described. Edge localized modes (ELMs) which are observed at the plasma boundary of the so-called high confinement regime are explained in Section 3.3. Successively, resonant magnetic perturbation coils that are installed at many tokamak experiments are discussed in Section 3.4. Their application for systematic island triggering and for an artificial ergodization of the plasma boundary to suppress ELMs is demonstrated. Finally, in Section 3.5, temperature measurements using electron cyclotron emission spectroscopy are explained.

NTMs

Contents

3.1. Tokamak Experiments

For the work at hand, the tokamaks TEXTOR and ASDEX Upgrade are of special interest. TEXTOR is a limiter tokamak with a circular plasma cross-section, a minor radius of 0.47 m,

TEXTOR

ASDEX Upgrade

ITER

Ohmic heating
NBI
ECRH

and a major radius of 1.75 m. Carbon tiles are used for the first wall. A recent overview is given in Reference [Neubauer05]. The divertor tokamak ASDEX Upgrade has a major radius of 1.65 m. The horizontal and vertical minor radii of the elongated plasma are typically 0.5 m respectively 0.8 m. The first wall surfaces are coated with tungsten. A current overview may be found in Reference [Hermann03]. The plasma cross-section of ASDEX Upgrade is similar to the one projected for the next-generation fusion experiment, ITER, which will have an average minor radius of 2 m and a major radius of 6.2 m. In all devices, the plasma is heated by the plasma current (Ohmic heating) as well as by additional heating methods like neutral beam injection (NBI) and electron cyclotron resonance heating (ECRH).

3.2. Neoclassical Tearing Modes

Neoclassical tearing modes, which have already been introduced theoretically in Section 2.6, are pressure driven instabilities that arise due to the helical perturbation of the bootstrap current caused by an initial magnetic island. They were originally identified experimentally by demonstrating the pressure-driven nature of $^3/_2$, $^4/_3$, and $^5/_4$ modes in the TFTR tokamak [Chang95]. For conventional tokamaks with a positive magnetic shear length,

$$L_q = \frac{q}{dq/dr} > 0, \tag{3.1}$$

and a negative radial pressure gradient,

$$\frac{dp}{dr} < 0, \tag{3.2}$$

the bootstrap current perturbation has a destabilizing effect and may render classically stable tearing modes metastable ($\rightarrow$ Section 2.6). An NTM can in this case be triggered by a sufficiently strong seed perturbation that is usually caused by different MHD activity as discussed below. A detailed understanding of these deleterious modes that are expected to be metastable in ITER as well ($^2/_1$ and $^3/_2$) is of great importance as will be explained below.

Figure 3.1 shows the averaged radial temperature profile across a $^3/_2$ NTM in ASDEX Upgrade. It demonstrates that the enhanced radial heat transport across magnetic islands deteriorates the energy confinement of the plasma significantly [Chang94, Sauter97]. The electron temperature is measured by electron cyclotron emission spectroscopy (ECE) which will be explained in Section 3.5. The temperature clearly flattens in the island region which notably reduces the temperature all the way from the position of the magnetic island to the plasma core (only a radial section is shown in the Figure). The temperature radially inwards from the island is reduced as $\nabla T_e/T_e$ is roughly constant in fusion plasmas due to temperature gradient driven turbulence. In fusion plasmas, such a drop of the plasma core temperature would strongly affect the fusion reaction rate. The confinement degradation due to magnetic islands will be examined numerically in Section 5.1. NTMs restrict the maximum achievable pressure gra-

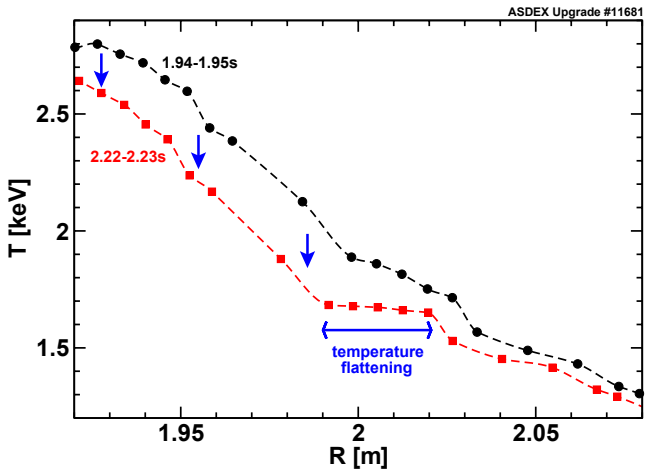

FIGURE 3.1. *Measurements of the time-averaged temperature profile are shown for ASDEX Upgrade discharge 11681. Profiles are given for the times where a $^3/_2$ island starts to grow ($t = 1.94 - 1.95$ s) and where it has reached its saturated size ($t = 2.22 - 2.23$ s). The temperature profile at the magnetic island flattens which leads to a reduction of the core plasma temperature.*

dients in tokamaks well below the ideal MHD limit[1]. Under certain conditions, neoclassical tearing modes can even lead to major plasma disruptions.

An NTM is triggered by a sufficiently large seed island that causes some temperature flattening. The perturbation of the bootstrap current acts as an additional island drive, which is described by the modified Rutherford equation that was already discussed in Section 2.6. The initial seed island is in most cases produced by different MHD modes like sawtooth crashes[2], fishbone activity[3], and edge localized modes (ELMs, → Section 3.3) while no clear trigger could be identified in a few cases where the NTMs start from a very small amplitude below the noise level [Sauter97, Gude99]. To predict the behavior of NTMs in ITER, the minimum seed island size that can raise an NTM at given normalized plasma pressure needs to be investigated and extrapolated. As discussed in Section 2.6, the polarization threshold related to island rotation and the transport threshold related to the incomplete temperature flattening inside small islands are relevant in this context. It is not completely clear yet how large the role of these two stabilizing contributions is for the seed island sizes in current tokamak experiments and how the relation between them will be in larger devices like ITER. The normalized plasma pressure (→ Section 2.6 for the definition of β_N) at the onset of neoclassical

ELMs

[1] The ideal limit is connected to the so-called ideal non-axisymmetric kink modes.

[2] Sawtooth crashes are periodic $^1/_1$ instabilities localized to the plasma center. The core plasma temperature drops abruptly, then slowly recovers.

[3] Oscillations in the soft x-ray emission related to a recurrent $m = 1$ internal kink mode that often occur during intense NBI heating are denoted fishbones.

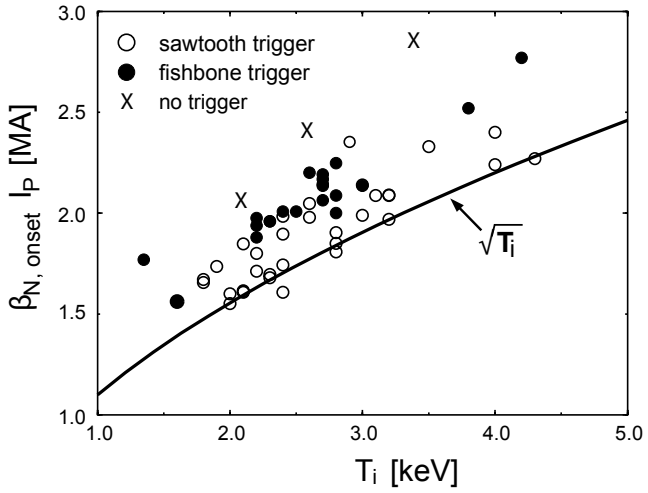

FIGURE 3.2. *The product of the normalized plasma pressure at mode onset, $\beta_{N,onset}$, and the plasma current, I_p, is shown versus the ion temperature, T_i, at the rational surface of the $^3/_2$ mode. The scaling $\beta_{N,onset} \cdot I_p \propto \rho_i^* \propto \sqrt{T_i}$ is depicted additionally. Good agreement with the scaling is observed. Clearly, different NTM triggering mechanisms require different values of $\beta_{N,normalized}$. The Figure is taken from Reference [Gude99].*

tearing modes, $\beta_{N,onset}$, has, however, been found in several experiments to be proportional to the normalized ion gyro-radius, $\rho_i^* = \rho_i/a \propto \sqrt{T_i}/(B_t a)$, as proposed by the ion polarization model [Günter98, La Haye00, Maraschek03]. This can be seen from Figure 3.2.

A special regime of neoclassical tearing modes has been identified in which the growth of the NTM is permanently interrupted by a sudden drop of the mode amplitude. Neoclassical tearing modes in this frequently interrupted regime have less impact on the energy confinement than usual NTMs, as they do not reach the saturated island size. These so-called FIR-NTMs are described in Section 3.2.1. Much effort has been made to develop methods for the avoidance or suppression of NTMs. Mode suppression by local heating and current drive techniques is demonstrated in Section 3.2.2.

3.2.1. Neoclassical Tearing Modes in the Frequently interrupted Regime

At large values of the normalized plasma pressure, β_N, a frequent interruption of the growth of neoclassical tearing modes by a sudden drop of the mode amplitude has been observed. The mode amplitude collapses periodically wherefore the mode does never reach its saturated island size [Günter01]. Such a mode is called a neoclassical tearing mode in the frequently interrupted regime (FIR-NTM).

FIR-NTM

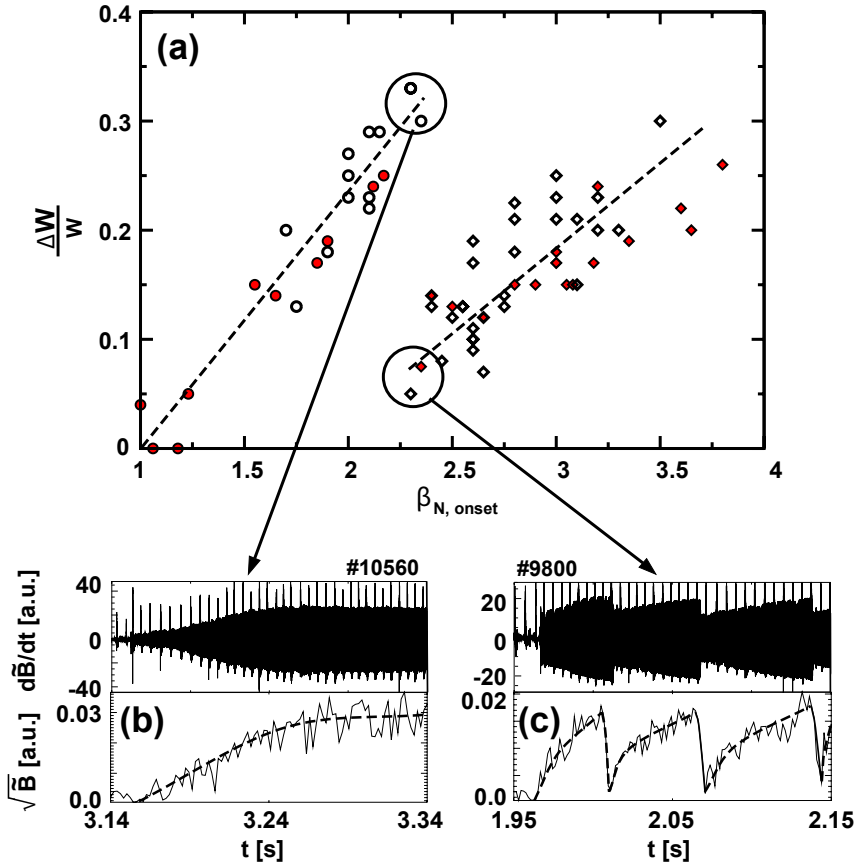

FIGURE 3.3. *Comparison of the reduction in the energy confinement ($\Delta W/W$) due to $^3/_2$ NTMs on ASDEX Upgrade (open symbols) and JET (full symbols). Very good agreement is seen, both in the relative confinement degradation as well as in the β_N value above which FIR-NTMs cause a reduced confinement degradation. The lower Figures show the NTM behavior for two ASDEX Upgrade discharges at about $\beta_N = 2.3$. The time-averaged amplitude for the FIR-NTM is significantly smaller (b) than the saturated amplitude of the smoothly growing mode (a). The Figure is taken from References [Günter01, Günter04].*

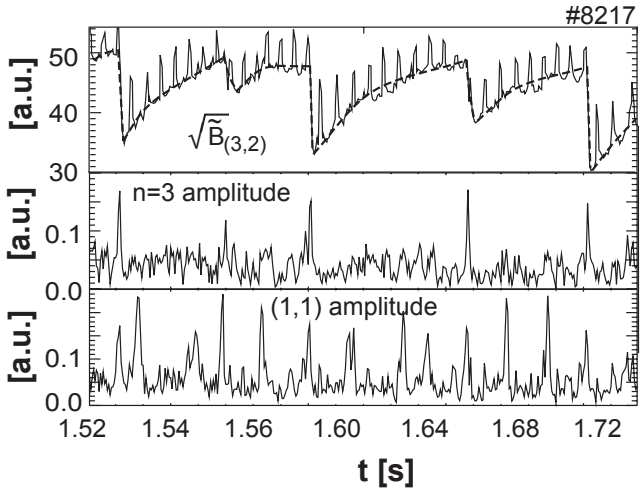

FIGURE 3.4. *The amplitude of a 3/2 FIR-NTM in ASDEX Upgrade is opposed to the amplitudes of 4/3 and 1/1 activities. The amplitude drops of the mode clearly coincide with 4/3 bursts and 1/1 activity. The spikes on the 3/2 signals result from large ELM activity. The Figure is taken from Reference [Günter03].*

Parts (b) and (c) of Figure 3.3 show typical magnetic signals, measured by Mirnov coils[4] in ASDEX Upgrade, for a 3/2 NTM and a 3/2 FIR-NTM. The repeated amplitude drops of the FIR-NTM are clearly visible and lead to a reduced average mode amplitude. As a result, the FIR-NTM causes less confinement degradation than the NTM. This can be seen from Part (a) of Figure 3.3, where the relative drop of the total plasma energy, $\Delta W/W$, is plotted versus the value of β_N at mode onset. With increasing values of β_N, the confinement degradation due to NTMs increases linearly and suddenly steps down as the FIR-NTM regime is reached.

The amplitude drop of FIR-NTMs has been shown to be correlated with different MHD mode activity [Gude02, Günter03]. This is shown in Figure 3.4, where the magnetic signal of the 3/2 NTM is compared to 4/3 and 1/1 activities. The amplitude drop of the 3/2 NTM coincides with bursts of these two modes. While the mode grows on a long time scale of the order of 50 ms, the amplitude drop takes place within about 1 ms. This may be related to field stochastization that arises due to the simultaneous occurrence of the different modes. This possibility will be examined in Section 8.3.

3.2.2. NTM Suppression

Methods for the prevention of NTMs are essential for a successful ITER operation. Various strategies have therefore been developed to avoid or suppress NTMs. These include the con-

[4] A voltage is induced in conducting coils in response to changes in the magnetic flux. Small coils placed outside the torus that are used to measure changes of the local poloidal magnetic field are called Mirnov coils.

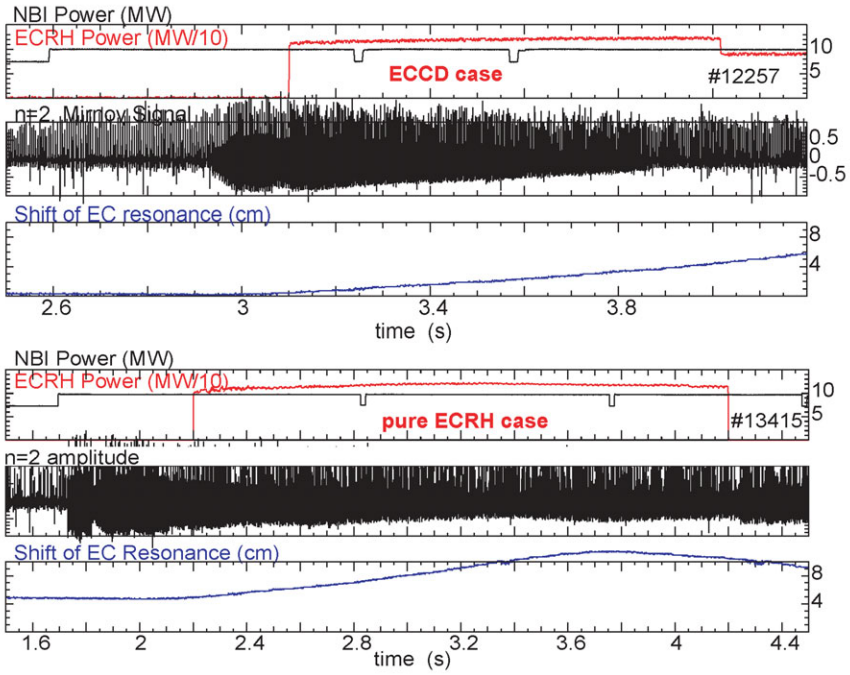

FIGURE 3.5. *The suppression of neoclassical tearing modes by electron cyclotron current drive (top) and with pure electron cyclotron resonance heating (bottom) is compared with similar discharge parameters. The application of ECRH allows to reduce the NTM amplitude only slightly, while ECCD of the same power leads to complete stabilization as seen from the $n = 2$ Mirnov coil signals. The spikes on these signals result from strong ELM activity. The blue curve gives the shift of the ECRH/ECCD resonant surface due to a B_t ramp. The Figure is taken from Reference [Zohm01].*

trol of sawteeth to eliminate or reduce seeds, the obstruction of the helical bootstrap current perturbation by external perturbation fields, and the application of microwave current drive at the resonant surface of the mode. The latter method stabilizes the NTM in two ways. It may replace the missing bootstrap current around the island O-point and increase the linear stability properties by modifying the equilibrium configuration [Hegna97, Zohm99, Isayama00].

ECCD

The necessary helical current can be generated by electron cyclotron current drive (ECCD) or electron cyclotron resonance heating (ECRH). Both methods rely on the absorption of electromagnetic radiation emitted by a gyrotron millimeter wave source that needs to be in resonance with the second harmonic of the electron gyration frequency. As the gyration frequency depends on $|\mathbf{B}|$, which is proportional to $1/R$ in toroidal plasma configurations, the deposition is localized to a narrow radial range. In ASDEX Upgrade, the deposition of the ECRH/ECCD system is shifted to the resonant surface of the NTM by ramping the toroidal magnetic field strength up or down ("B_t ramp"). ECRH relies on the heating effect of the radiation that locally reduces the plasma resistivity and thereby increases the inductively driven plasma current at the island O-point. For ECCD, the electromagnetic radiation is injected obliquely. Due to relativistic effects, the resonant surfaces of the electrons traveling in opposite toroidal directions are shifted slightly with respect to each other such that one of the two species is heated preferentially. These electrons become hotter and therefore less collisional than the electrons moving in the opposite toroidal direction which gives rise to an effective toroidal current. Experimental investigations have proven that ECRH has a stabilizing effect onto NTMs. However, ECCD is expected to be significantly more efficient as illustrated in Figure 3.5.

Bt ramp

3.3. Edge Localized Modes

H-mode pedestal

In the so-called high-confinement regime (H-mode), a transport barrier with strongly reduced transport coefficients (pedestal) is formed just inside the separatrix, which increases the plasma confinement significantly [Wagner82]. The exact physics behind the formation of the pedestal is still not well understood. It is hypothesized that it is connected to the suppression of turbulence by zonal flows, a sheared plasma rotation in the high magnetic shear region that may interfere with the formation of turbulent eddies.

Edge localized modes (ELMs) are observed at the H-mode plasma boundary. They lead to a periodic loss of energy and particles (several percent of the total plasma energy and particle content during one ELM crash) on the time-scale of one millisecond. The ensuing large transient heat load to the divertor targets may damage the wall materials. The mitigation of ELMs is therefore of great importance. Experimental approaches to achieve this goal have been made, e.g., with artificial ELM triggering by the injection of frozen deuterium pellets into the plasma edge. This allows to increase the ELM frequency and thereby reduce the energy loss per ELM crash [Lang03].

Another method is the ELM suppression by an ergodization of the plasma boundary with

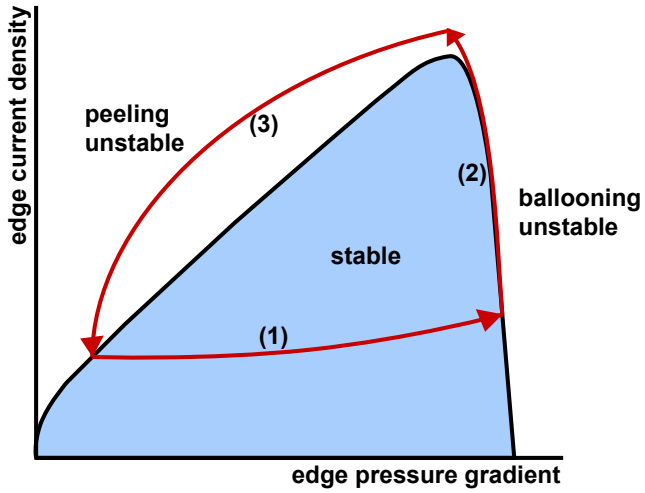

FIGURE 3.6. *An ELM cycle according to the ballooning-peeling model is shown. The ELM cycle starts at a low edge pressure gradient and a low edge current density after a previous ELM crash. The edge pressure gradient starts to rise due to the reduced transport at the H-mode plasma boundary until the ballooning stability limit is reached (1). Successively the pressure gradient driven bootstrap current builds up until the peeling stability limit is reached (2). The edge plasma becomes unstable and an ELM crash takes place which reduces the edge pressure gradient and the edge current density on a very short time-scale (3). Then, with the restoration of the pressure pedestal, the next ELM cycle starts.*

external perturbation coils [Evans08], which will briefly be discussed in Section 3.4.3. An increased radial impurity transport across the transport barrier at the edge as it is provided by ELMs is important for steady state H-mode operation as it helps to avoid impurity accumulation in the plasma. This is especially important for fusion plasmas with a continuous production of helium impurities and for wall materials with a large atomic number, Z. The increased transport can, however, not only be provided by ELMs but also by an ergodization of the plasma boundary by magnetic perturbation coils. This is discussed in the following Section as a method for ELM suppression.

ELMs can be explained reasonably by the ballooning-peeling model [Connor98]. The strong pressure gradient and the strong bootstrap current at the plasma boundary drive edge instabilities: the pressure-driven ballooning mode and the current-driven peeling mode. It has been shown, that both types of modes can become unstable at moderate to high toroidal mode numbers ($n = 3 \ldots 30$). After the ELM crash the pedestal height is reduced significantly such that the plasma has dropped below the ballooning-peeling stability limit. When pressure and current rise again, the stability limit is reached anew such that the next ELM crash takes place. Figure 3.6 illustrates the ballooning-peeling model for an ELM cycle.

3.4. Resonant Magnetic Perturbation Coils

As discussed in Section 2.5, the formation of magnetic islands is connected to resonant magnetic field perturbations which may result from plasma instabilities like tearing modes but can also be produced artificially by resonant magnetic perturbation coils (RMP-coils). The RMP coils installed at TEXTOR and the ones planned for ASDEX Upgrade are described briefly in Section 3.4.1. The field produced by such coils usually contains a broad spectrum of magnetic perturbations which can raise several magnetic islands as shown in Section 3.4.2. At the plasma boundary, the magnetic field may become stochastic due to the large number of adjacent resonant surfaces. There is experimental evidence that a stochastic plasma boundary can suppress edge localized modes as briefly discussed in Section 3.4.3.

RMP-coils

3.4.1. RMP Coils in TEXTOR and ASDEX Upgrade

In TEXTOR, 16 RMP-coils are installed at the high-field side of the plasma. They are aligned to the $^3/_1$ surface in the sense that they wind helically around the torus, each coil performing one full toroidal and $^1/_3$ of a poloidal turn. They can optionally be operated with DC or AC currents. This allows for a dynamic stochastisation of the plasma boundary which is called dynamic ergodic divertor (DED) at TEXTOR [Finken97]. Depending on how the individual coils are connected to the four available current phases, dominant $^3/_1$, $^6/_2$, or $^{12}/_4$ perturbation modes are possible.

DED

When the coils are applied to drive a magnetic island in the core plasma which is briefly described in Section 3.4.2, the AC capability can be used to create a rotating magnetic island. The geometry of the coil set is shown in Figure 3.7. As the coils do not cover the full poloidal angle, they also produce a strong $^2/_1$ magnetic component when operated in $^3/_1$ mode (sideband) which may give rise to a $^2/_1$ magnetic island. For such an island, a comparison of numerical heat diffusion simulations to measurements of the electron temperature is performed in Chapter 6.

sideband

At the ASDEX Upgrade tokamak, a set of 24 saddle field coils is planned to be installed for the generation of resonant magnetic perturbations [Suttrop07]. They are designed in a way that offers large operational flexibility for experiments, e.g., regarding ELM suppression, feedback control of certain MHD modes, and the triggering of magnetic islands. The geometry of these coils that will be installed at the low-field side of the plasma inside the vacuum vessel is shown in Figure 3.8. ELM suppression with a plasma boundary ergodized by RMP-coils is briefly addressed in Section 3.4.3. Heat transport across such an ergodic plasma boundary is investigated numerically in Section 8.4.

3.4.2. Driving Islands

RMP coils can be used to systematically trigger magnetic islands. In TEXTOR, where NTMs are not unstable due to the low bootstrap current fraction, this opportunity is taken to desta-

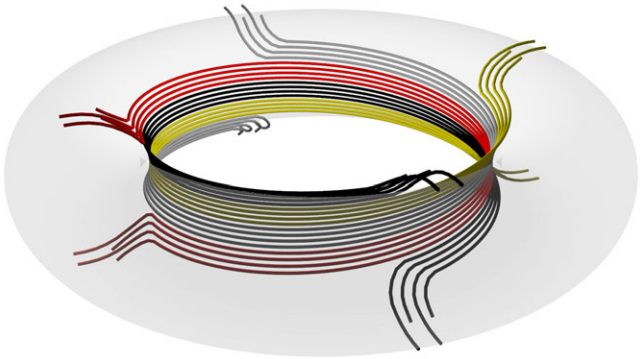

FIGURE 3.7. *The DED coils that are installed at the high-field side of the TEXTOR tokamak are aligned to the magnetic field lines of the* $^3/_1$ *resonant surface. Four different current phases, which are shifted by* 90° *each, are available for coil supply. The color coding indicates which coils are fed by the same current phase when the DED coils are operated in* $^3/_1$ *configuration.*

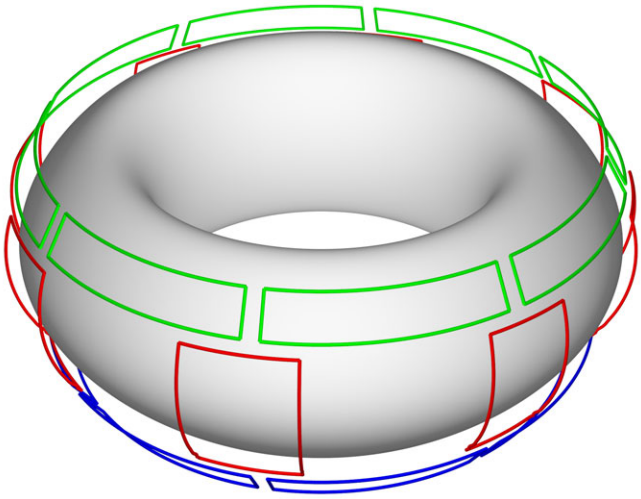

FIGURE 3.8. *The RMP coils that will be installed at the low field side of the ASDEX Upgrade tokamak are shown. The eight coils located around the midplane are denoted A-coils (red), the upper eight coils Bu-coils (green) and the lower eight coils Bl-coils (blue).*

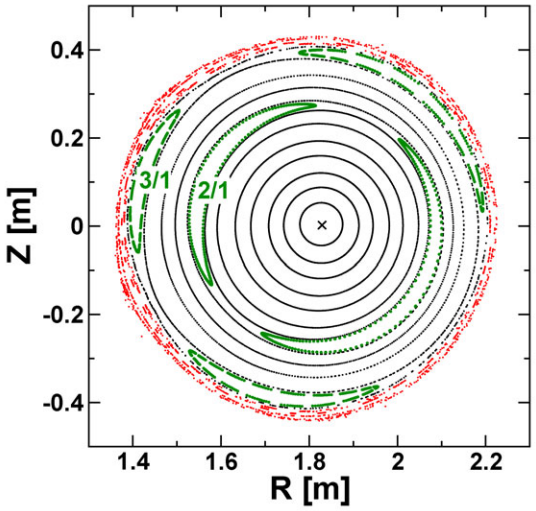

FIGURE 3.9. *The magnetic field structure of the TEXTOR tokamak is shown for an equilibrium that is perturbed by the DED coils in $^3/_1$ configuration. Marked in green, $^2/_1$ and $^3/_1$ islands can be seen as well as the ergodic plasma boundary (red) and unaffected flux surfaces (black).*

bilize and study magnetic islands. Figure 3.9 shows a Poincaré plot of the magnetic topology that results when the DED coils are operated in $^3/_1$ configuration. The $^2/_1$ and $^3/_1$ islands caused by the external magnetic perturbation are clearly visible as well as the ergodized plasma boundary. For this Figure, the plasma response to the external magnetic field perturbation was not taken into account ("vacuum-assumption").

vacuum-assumption

The external perturbation field changes the boundary condition for the perturbed poloidal flux, $\tilde{\Psi}$, at the plasma edge and thereby modifies the value of the tearing stability index, Δ' ($\rightarrow$ Section 2.5.1), which may destabilize the otherwise stable island. Islands triggered by such an external perturbation behave like "usual" magnetic islands in most respects. Using the AC capability of the RMP coil set, a rotating island can be triggered.

3.4.3. ELM Suppression

For large machines like ITER, natural ELM events might damage the first wall materials due to the large transient heat load onto the divertor targets. One approach to face this problem is to trigger ELMs artificially by depositing deuterium pellets at the plasma edge to increase the ELM frequency and reduce the lost thermal energy per ELM event [Lang03]. ELMs can also be mitigated by an ergodization of the plasma boundary with auxiliary magnetic field coils [Hender92, Evans04, Evans08].

The results of ELM mitigation experiments at the DIII-D tokamak are shown in Figure 3.10. The ELM size can be decreased or ELMs can even be suppressed completely by a stochastisa-

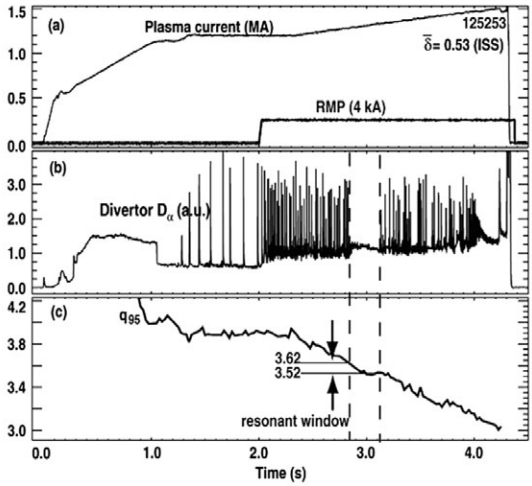

FIGURE 3.10. *The influence of an ergodic plasma boundary onto ELMs is demonstrated. ELMs are visible as peaks in the D_α signal that gives the divertor radiation intensity. With increasing RMP coil currents, the ELM frequency increases reducing the energy loss per ELM event. By a ramp-up of the plasma current, the edge safety factor, q_{95}, is reduced. Within a certain range of q_{95} values, ELMs are completely suppressed. The Figure is taken from [Evans08].*

tion of the magnetic field structure at the plasma edge with resonant magnetic field coils. The physics that lead to the effectiveness of this method are not fully understood yet. It is believed to be related to an increased heat and particle transport at the plasma edge that keeps the pressure gradient from rising to the peeling-ballooning limit. In this work, the isolated effect of a stochastization of the magnetic field structure at the plasma boundary onto the electron heat transport will be addressed (Section 8.4).

3.5. Temperature Measurement

For the comparison of numerical heat transport simulations to the experiment, sophisticated temperature measurement techniques are required. Various diagnostics like Langmuir probes (at the plasma edge only), Thomson scattering, or charge exchange recombination spectroscopy (CXRS) play a role for the determination of plasma temperatures in fusion experiments. Electron cyclotron emission spectroscopy (ECE) is the most reliable instrument for the determination of local electron temperatures with sampling frequencies up to several Megahertz. The physical basics and technical capabilities of ECE diagnostics are briefly discussed in the following. For more details, refer, e.g., to Reference [Hartfuss97].

ECE

Similarly to an antenna, electrons emit electromagnetic radiation at the gyration angular frequency, $\omega_{c,e} = eB/m_e$, and the harmonics, $l \cdot \omega_{c,e}$, when gyrating around magnetic field lines

(l denotes an integer number). The component of the emission for which the wave-vector, $\mathbf{k}$, is perpendicular to the (toroidal) magnetic field, $\mathbf{B}_t$, consists of the "O-mode" ($\mathbf{E}||\mathbf{B}_t$) and "X-mode" ($\mathbf{E}\perp\mathbf{B}_t$) polarization flavors. Fusion plasmas are usually optically thick for the first harmonic O-mode and the first and second harmonic X-modes [Hartfuss97] which means that radiation is continuously absorbed and re-emitted. In this case, the plasma behaves roughly like a black-body radiator and can be described by Planck's law. As the gyration frequency is situated in the long wavelength-tail of the Plack distribution, Planck's law simplifies to the Rayleigh-Jens law which predicts the emitted radiation intensity at a given frequency to be proportional to the electron temperature. Thus, the temperature can directly be determined from the radiation intensity while the spatial information is obtained from the frequency.

As the magnetic field strength is proportional to $1/R$ in toroidal configurations, each emitted frequency corresponds to a well-defined radial plasma position such that a complete radial profile of the electron temperature may, in principle, be gained from a single line of sight. Apart from relativistic broadening, the spatial resolution is restricted by the finite optical thickness of the plasma and the spectral resolution of the diagnostic. Due to these physical and technical restrictions, the temperature is in practice determined on several discrete points along the line of sight that are typically separated by about one centimeter. Pre-conditions for ECE measurements are a sufficient optical thickness of the plasma at the measurement frequency and a low enough plasma density to ensure that the detected frequencies remain beyond the plasma frequency. The plasma frequency is an eigen-oscillation of the electrons below which no electromagnetic oscillations can permeate through the plasma (cut-off).

plasma frequency

cut-off

As a result of the plasma rotation, ECE can be used to obtain two-dimensional information about the electron temperature, provided the temperature distribution changes slowly compared to the plasma rotation frequency. In this case, the time dependence of the ECE-signals translates into the toroidal temperature distribution. Using several lines of sight, the electron temperature can be simultaneously measured on a two-dimensional domain. Such ECE-Imaging [Park03] diagnostics are installed in TEXTOR and, since very recently, also in ASDEX Upgrade. Data from ECE(-Imaging) measurements is, for example, found in References [Meskat01] for ASDEX Upgrade and [Classen07] for TEXTOR.

ECE-Imaging

The averaged radial temperature profile determined by ECE in ASDEX Upgrade for discharge 11681 is given in Figure 3.1. The local flattening of the temperature profile due to a magnetic island can clearly be seen. A comparison of numerical simulations to ECE-Imaging measurements in TEXTOR that allows to determine the experimental heat diffusion anisotropy is presented in Chapter 6. A similar comparison for ASDEX Upgrade, where an ECE-Imaging diagnostic was installed very recently, is found in Chapter 7.

Chapter 4.

Model

Analytical studies of diffusive heat transport are usually restricted to simple slab geometries or the so-called periodic cylinder, where examinations are still limited to the small ($w/w_c \to 0$) and large island cases ($w/w_c \to \infty$). For investigations regarding realistic islands (w/w_c of order unity) and for toroidal geometries, numerical approaches are necessary. For this purpose, it is useful to express the heat diffusion equation in tensor notation as done in Section 4.1. This general formulation provides a large flexibility regarding the coordinate choice as it does not rely on any physical properties of the coordinate system.

Numerical simulations of heat transport in magnetized plasmas are quite demanding due to the large heat diffusion anisotropy in state of the art fusion devices. The discretization method needs to be chosen with care to avoid the poisoning of cross-field transport by unphysical numerical diffusion. Usual numerical schemes introduce a strong numerical diffusion that may even exceed the true physical diffusion unless the coordinate system is aligned very precisely to the magnetic field lines or extremely high order schemes are used. Both approaches result in large computational efforts. In this work, in contrast to that, a low-order finite difference scheme is applied which suppresses numerical diffusion effectively even for unrealistically large anisotropies. This scheme, which is described in Section 4.2, renders heat transport simulations possible in coordinates that are not aligned to the magnetic field lines.

Some coordinate adaptation to the respective physical problem is still useful as it allows to reduce the necessary spatial resolutions. In all cases, except for computations across the plasma boundary, coordinates are used where the magnetic flux surfaces are radial coordinate surfaces (flux coordinates) and the magnetic field lines are straight lines (straight field line coordinates). A transformation to a helical coordinate system that is roughly aligned to the physical problem, e.g., to a magnetic island, is useful to relax the toroidal resolution requirements. The radial resolution can locally be adapted to the physical demands by radial grid meshing. The coordinate systems relevant for this work are described in Section 4.3. Some additional details are given in Appendix A.

flux coordinates
straight field line coordinates

Numerical codes have been implemented for the solution of the heat diffusion equation in, both, periodic cylindrical and realistic toroidal geometries to allow for a direct comparison to analytical theories and experimental measurements. Some details on the implementation are given in Section 4.4.

Contents

4.1. Heat Diffusion Equation

To be able to solve the heat diffusion equation, which was already discussed in Section 2.4.1, in curvilinear toroidal coordinate systems, it is convenient to use tensor notation. For a brief introduction to tensor analysis refer to Appendix A.1 or for more details to Reference [D'haeseleer91]. The divergence of the heat flux density has the tensorial form

$$\frac{1}{\sqrt{g}}\frac{\partial}{\partial u^{\alpha}}(\sqrt{g}q^{\alpha}), \tag{4.1}$$

where $g = \det[g_{\alpha\beta}]$ denotes the determinant of the metric tensor and q^{α} the contravariant components of the heat flux density[1]. Using Equation (4.1), the heat diffusion equation, Equa-

[1] The Einstein summation convention is applied as α appears as a co- and as a contravariant index in the same term ($\rightarrow$ Appendix A.1).

tion (2.30), may be written as

$$\frac{3}{2}n_e\frac{\partial T}{\partial t}+\frac{1}{\sqrt{g}}\frac{\partial}{\partial u^\alpha}(\sqrt{g}q^\alpha)=P, \tag{4.2}$$

which contains components of the heat flux density that also need to be expressed in tensor notation. The heat flux density is given by Equation (2.31) and contains the temperature gradient, ∇T, and the temperature gradient along magnetic field lines, $\nabla_{||}T$. The contravariant components of the temperature gradient are given by

$$[\nabla T]^\alpha=[\nabla T]\cdot\mathbf{e}^\alpha=\left[\frac{\partial T}{\partial u^\beta}\mathbf{e}^\beta\right]\cdot\mathbf{e}^\alpha=g^{\alpha\beta}\frac{\partial T}{\partial u^\beta}, \tag{4.3}$$

where $\mathbf{e}^\alpha$ denote the contravariant basis-vectors and use has been made of $\mathbf{e}^\alpha\cdot\mathbf{e}^\beta=g^{\alpha\beta}$. The contravariant components of the parallel temperature gradient may be expressed by

$$\left[\nabla_{||}T\right]^\alpha=\left[\nabla_{||}T\right]\cdot\mathbf{e}^\alpha=[\mathbf{b}(\mathbf{b}\cdot\nabla T)]\cdot\mathbf{e}^\alpha=\left[b^\gamma\mathbf{e}_\gamma\left(b^\varepsilon\mathbf{e}_\varepsilon\cdot\frac{\partial T}{\partial u^\beta}\mathbf{e}^\beta\right)\right]\cdot\mathbf{e}^\alpha, \tag{4.4}$$

where $\mathbf{e}_\alpha$ denote the covariant basis vectors and $b^\alpha=\mathbf{e}^\alpha\cdot\mathbf{b}$ the contravariant components of the magnetic field direction vector. Using

$$\mathbf{e}_\alpha\cdot\mathbf{e}^\beta=\delta_\alpha^\beta\equiv\begin{cases}1, & \text{for } \alpha=\beta\\ 0, & \text{otherwise,}\end{cases} \tag{4.5}$$

where δ_α^β denotes the Kronecker-delta, this can be further simplified to the form

$$\left[\nabla_{||}T\right]^\alpha=b^\alpha b^\beta\frac{\partial T}{\partial u^\beta}. \tag{4.6}$$

Thus, by applying Equations (4.3) and (4.6), the contravariant components of the heat flux density can be written as

$$q^\alpha=-n_e\chi_\perp\left[\chi b^\alpha b^\beta+g^{\alpha\beta}\right]\frac{\partial T}{\partial u^\beta}. \tag{4.7}$$

Finally, by inserting Equation (4.7) into Equation (4.2), the heat diffusion equation can be written as

$$\frac{3}{2}n_e\frac{\partial T}{\partial t}-\frac{1}{\sqrt{g}}\frac{\partial}{\partial u^\alpha}\left[C^{\alpha\beta}\frac{\partial T}{\partial u^\beta}\right]=P, \tag{4.8}$$

where the tensor

$$C^{\alpha\beta} = \sqrt{g} n_e \chi_\perp \left(\chi b^\alpha b^\beta + g^{\alpha\beta} \right) \tag{4.9}$$

has been introduced as a short-hand. This formulation does not presume certain physical properties of the coordinates such that almost any toroidal coordinate system may be used. However, the structure of the physical problems still demands adequately chosen coordinate systems. Narrow temperature structures, for instance, arise at magnetic islands. Resolving these requires unnecessarily large spatial resolutions in inappropriate coordinate systems. The coordinate systems utilized in this work are described in Section 4.3 and some additional details are given in Appendix A.

4.2. Discretization

The discretization of the heat diffusion equation is performed with a finite difference scheme that suppresses the numerical diffusion, which normally arises due to the large heat conduction anisotropy when unaligned coordinate systems are used, very effectively. "Unaligned" refers to coordinate systems where no coordinate line is parallel to the magnetic field lines. The numerical scheme is described in Section 4.2.1 and it's capabilities are discussed in Section 4.2.2. Details on the periodicity and boundary conditions are given in Section 4.2.3. Subsequently, the system of equations that results from the discretization is discussed in Section 4.2.4 and the solution of this system of equations that can be written in matrix form is addressed in Section 4.2.5.

4.2.1. Finite Difference Scheme

finite difference scheme

The finite difference scheme used for the discretization of the heat diffusion equation was developed in References [Günter05, Günter07]. Two spatial grids are required for the implementation.

T-grid

- The temperature, the heating power density, and several other quantities are given on one grid that is called T-grid. The grid points of the T-grid are denoted by integer grid point indices. The radial, poloidal, and toroidal grid point indices, i, j, and k, take the values

$$i = 0 \ldots G_\rho, \tag{4.10}$$
$$j = 0 \ldots G_\theta - 1, \tag{4.11}$$
$$k = 0 \ldots G_\phi - 1 \tag{4.12}$$

  on the T-grid. Here, G_ρ, G_θ, and G_ϕ denote the number of radial, poloidal, and toroidal grid points, respectively.

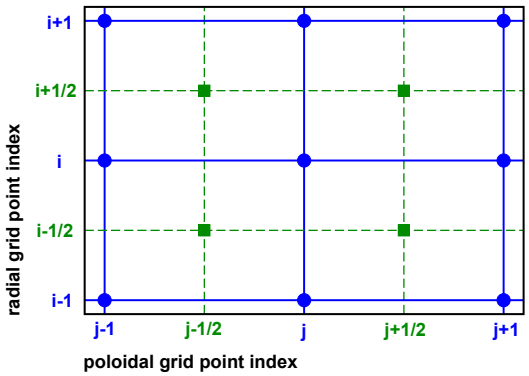

FIGURE 4.1. *The staggered grids required for the discretization of the heat diffusion equation are illustrated in two dimensions. The temperature grid (T-grid) is marked by blue circles and the heat flux grid (q-grid) by green squares. Both grids are shifted against each other by half a grid point distance in all dimensions.*

- The heat flux density, the heat diffusion coefficients, and several other quantities are defined on the other grid called q-grid. The q-grid is shifted against the T-grid by half a grid point distance in all three dimensions as illustrated in Figure 4.1 (staggered grids). Half-integral grid point indices are associated with the grid points of the q-grid.

q-grid
staggered grids

For the discretization of the heat diffusion equation, the differential operators are expressed by finite differences. Each derivative required on grid points of the q-grid is calculated from values on the T-grid and vice versa. As an example, the radial, poloidal and toroidal derivatives of the temperature at the grid point $[i+\frac{1}{2}, j+\frac{1}{2}, k+\frac{1}{2}]$ on the q-grid are given by the finite difference expressions

$$\left[\frac{dT}{d\rho}\right]_{i+\frac{1}{2},j+\frac{1}{2},k+\frac{1}{2}} = \frac{1}{4\Delta\rho}\sum_{\tilde{j}=j}^{j+1}\sum_{\tilde{k}=k}^{k+1}\left(T_{i+1,\tilde{j},\tilde{k}} - T_{i,\tilde{j},\tilde{k}}\right), \tag{4.13}$$

$$\left[\frac{dT}{d\theta}\right]_{i+\frac{1}{2},j+\frac{1}{2},k+\frac{1}{2}} = \frac{1}{4\Delta\theta}\sum_{\tilde{i}=i}^{i+1}\sum_{\tilde{k}=k}^{k+1}\left(T_{\tilde{i},j+1,\tilde{k}} - T_{\tilde{i},j,\tilde{k}}\right), \tag{4.14}$$

$$\left[\frac{dT}{d\phi}\right]_{i+\frac{1}{2},j+\frac{1}{2},k+\frac{1}{2}} = \frac{1}{4\Delta\phi}\sum_{\tilde{i}=i}^{i+1}\sum_{\tilde{j}=j}^{j+1}\left(T_{\tilde{i},\tilde{j},k+1} - T_{\tilde{i},\tilde{j},k}\right). \tag{4.15}$$

Here, i, j, and k denote integral radial, poloidal, and toroidal grid point indices. Any derivative of the temperature on the q-grid may, thus, be expressed as a linear combination of the temperature values on the eight neighboring grid points on the T-grid ($2\times2\times2$ stencil). Derivatives on the q-grid are determined completely analogical to that and involve the eight neighboring grid points on the T-grid. For instance, consider the toroidal derivative of a contravariant

component of the heat flux density that is determined by the finite difference formulation

$$\left[\frac{dq^{\alpha}}{d\phi}\right]_{i,j,k} = \frac{1}{4\Delta\phi}\sum_{\tilde{i}=i-\frac{1}{2}}^{i+\frac{1}{2}}\sum_{\tilde{j}=j-\frac{1}{2}}^{j+\frac{1}{2}}\left(q^{\alpha}_{\tilde{i},\tilde{j},k+\frac{1}{2}} - q^{\alpha}_{\tilde{i},\tilde{j},k-\frac{1}{2}}\right). \tag{4.16}$$

As the heat diffusion equation contains second derivatives, the finite difference formulation of the heat diffusion equation on one grid point $[i,j,k]$ of the temperature grid involves a linear combination of the temperature values on 27 grid points of the T-grid: The considered grid point itself and the nearest neighbors in all three dimensions ($3\times3\times3$ stencil).

4.2.2. Scheme Capabilities

In contrast to other schemes, the discretization method described in the previous Section allows to perform heat diffusion computations with realistic values of χ in coordinate systems with no coordinate line parallel to the magnetic field lines. This is especially important, if permanently adapting the coordinate system in time-dependent computations becomes too expensive or if exactly aligned global coordinate systems do not even exist as in the cases of ergodic field layers or calculations extending across the plasma separatrix.

In the following, the scheme-capabilities are demonstrated by a simple numerical test that is taken from Reference [Günter05]. The two-dimensional magnetic field configuration defined by $\mathbf{B} = \mathbf{e}_z \times \nabla\Psi$ is chosen, where $\Psi = \sin(2\pi x)\cos(2\pi y)$. By setting the energy source term to $P = -\chi_{\perp}\nabla^2\Psi$, it is ensured that the temperature is constant on flux surfaces independently of the heat diffusion anisotropy, $\chi_{||}/\chi_{\perp}$, for appropriate boundary conditions. The computational domain $x,y = -0.5\ldots0.5$ is resolved.

In Figure 4.2, numerical solutions to the two-dimensional problem are given. Part (a) of the Figure contains the results obtained with the finite difference formulation described in Section 4.2.1, while Part (b) shows the results for a conventional discretization. In the region with field lines that intersect with the boundary of the computational regime, both solutions are essentially correct. However, in the region with closed field lines ($y = -0.25\ldots0.25$), only the symmetric discretization is able to obtain the correct results. For the conventional numerical scheme, the temperature profile is completely flattened in the closed field line region which results from strong unphysical diffusion arising perpendicular to the magnetic field lines.

4.2.3. Periodicity and Boundary Conditions

periodic boundaries
virtual grid points

To be able to use the discretization formulations of Section 4.2.1 also on grid points close to the periodic boundaries at $\theta = 2\pi$ respectively $\phi = 2\pi$, virtual grid points are introduced. In the poloidal direction, the virtual grid points $[i,-1,k]$ are equivalent to the grid points $[i,G_{\theta}-1,k]$ and the virtual grid points $[i,G_{\theta},k]$ are equivalent to the grid points $[i,0,k]$. In toroidal direction the situation is analogous unless the coordinate system is transformed to a

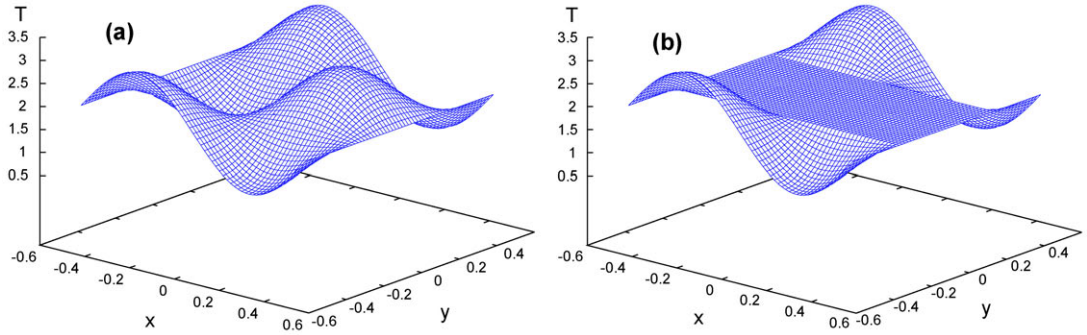

FIGURE 4.2. *Numerical solutions of the two-dimensional heat diffusion equation are shown* ***(a)*** *for the symmetric scheme described above and* ***(b)*** *for an asymmetric discretization. The heat diffusion anisotropy is set to* 10^9 *and the problem is chosen such that the solution is analytically known. It is reproduced almost exactly by the symmetric scheme. The asymmetric discretization, however, leads to a large numerical diffusion that flattens the temperature profile in parts of the computational domain. The solution is only correct in regions where the magnetic field lines intersect with the edge of the computational regime where Dirichlet boundary conditions are applied. The numerical test is described in detail in Reference [Günter05], from which this Figure was taken.*

helical one, in which case the coordinate lines do in general not close into themselves. This is discussed in detail in Section 4.3.4.

boundary conditions

For the solution of the heat diffusion equation, appropriate boundary conditions need to be applied at the inner ($\rho = \rho_{min}$) and outer ($\rho = \rho_{max}$) radial boundaries of the computational regime. Three different boundary conditions are implemented in the cylindrical and toroidal heat diffusion codes written for this work.

- Dirichlet boundary conditions that specify the temperature values may be used at the inner and outer boundaries of the computational regime. The implementation involves only grid points at $i = 0$ for the inner boundary and grid points at $i = G_\rho$ for the outer boundary.

  Dirichlet boundary conditions

- Neumann boundary conditions that specify the first radial derivative of the temperature may be used at the inner and outer boundaries of the computational regime. If Neumann boundary conditions are applied, they involve grid points at $i = 0, 1$ for the inner boundary respectively at $i = G_\rho, G_\rho - 1$ for the outer boundary.

  Neumann boundary conditions

- For computations that include the plasma center ($\rho_{min} \equiv 0$), an additional "natural" boundary condition is available for the magnetic axis. For this center boundary condition, the heat diffusion equation is also solved at the inner boundary. The derivation is discussed in the following. This boundary condition involves grid points at $i = 0, 1, 2$.

The heat diffusion equation needs be modified for the use as a boundary condition at the magnetic axis, as some terms diverge at $\rho = 0$. This problem can be solved by integrating Equation (4.8) over a small volume around the magnetic axis,

$$\int_0^{2\pi} d\phi \int_0^{2\pi} d\theta \int_0^{\Delta\rho} d\rho \; g \; \ldots. \tag{4.17}$$

Here, $\Delta\rho$ denotes the radial grid point distance. Assuming axisymmetric coordinates, the integration can be carried out partially, and the remaining integrals may be approximated by sums. After dividing the result by $\frac{1}{2}\Delta\phi\Delta\theta\Delta\rho$, one obtains

$$\sum_{kj} \left\{ g \left[\frac{3}{2} n \frac{\partial T}{\partial t} - P \right] - [gP]_{0,j,k} - C^{\rho\beta} \frac{\partial T}{\partial u^\beta} \left[\frac{2\sqrt{g}}{\Delta\rho} - \frac{\partial \sqrt{g}}{\partial \rho} - \frac{\partial \sqrt{g}}{\partial \theta} \right] \right\} = 0, \tag{4.18}$$

which is an appropriate boundary condition for the plasma center at $\rho = 0$. All quantities are evaluated at the grid point indices $[1, j, k]$ unless explicitly indicated differently by a subscript. The derivative $[\partial T/\partial\rho]_{1,j,k}$ is discretized straight-forwardly by

$$\left[\frac{\partial T}{\partial \rho} \right]_{1,j,k} = \frac{T_{2,j,k} - T_{0,j,k}}{2\Delta\rho}. \tag{4.19}$$

Analogous discretizations are applied to $[\partial T/\partial\theta]_{1,j,k}$ and to $[\partial T/\partial\phi]_{1,j,k}$.

4.2.4. Matrix Structure

When the grid points are ordered linearly by assigning the unique index,

$$ind(i, j, k) = i \cdot G_\phi G_\theta + j \cdot G_\phi + k + 1, \tag{4.20}$$

to each real grid point of the T-grid, the linear system of equations that arises from the discretization of the heat diffusion equation may be written in matrix-vector form,

$$\hat{A}\mathbf{x} = \mathbf{b}, \tag{4.21}$$

where $\hat{A}$ denotes the coefficient matrix of the system of equations, $\mathbf{b}$ the right hand side vector representing the source term, and $\mathbf{x}$ the vector of the unknown temperature values that need to be determined by solving the system of equations.

The implicit discretization of the heat diffusion equation at one point of the T-grid involves the unknown temperature values at 27 grid points as discussed above. This corresponds to 27 non-zero entries per matrix row. For the grid points at the inner and outer radial boundary of the computational regime, where the boundary conditions are implemented, this number is naturally different. The matrix structure is shown in Figure 4.3 for a resolution of $G_\rho = G_\theta = G_\phi = 5$ radial, poloidal, and toroidal grid points. A block tri-diagonal structure is visible,

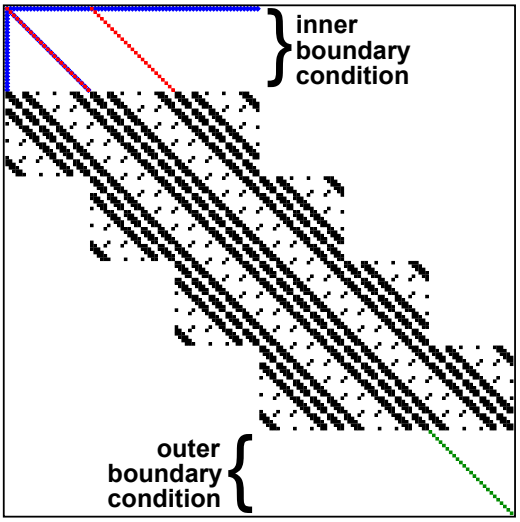

FIGURE 4.3. *The matrix structure for $5 \times 5 \times 5$ grid points is shown. For this purpose, the non-zero matrix elements are marked. At the inner boundary of the computational regime, Neumann (red) respectively center boundary conditions (blue) are applied while Dirichlet boundary conditions are used at the outer edge of the computational regime (green).*

where each block has the dimension $dim_{block} = G_\theta \times G_\phi$. Each block-row and block-column corresponds to a certain radial grid point index i and there are 9 non-zero matrix entries in each row inside a single block.

The dimension of the matrix is equal to the number of grid points on the temperature grid, that is, $dim = (G_\rho + 1) \times G_\theta \times G_\phi$. The number of non-zero matrix entries, nnz, is asymptotically proportional to the matrix dimension, dim, which clearly constitutes a sparse matrix structure. The individual blocks of the block tri-diagonal matrix are sparse as well with $9 \times dim_{block}$ non-zero entries in each block.

sparse matrix

4.2.5. Matrix Solver

The solution of the linear system of equations with a full-matrix solver is computationally much too expensive and would lead to an infeasible memory consumption. Instead, the solving algorithm needs to take advantage of the matrix sparsity. The matrix is stored in compressed sparse row format (CSR) in which only the non-zero matrix elements are given and the memory consumption for matrix-storage is proportional to the number of non-zero matrix entries instead of dim^2 for full matrix storage.

For the solution of the matrix equation, the sparse matrix solver of the Watson Sparse Matrix Package (`WSMP`) was used that is described in Reference [Gupta00] and can handle general sparse matrices. `WSMP` uses a direct solution technique. The solver takes the sparse matrix

WSMP Solver

stored in CSR format and the right hand side vector as an input. For the problems of this work, where the number of nonzero elements in the original matrix is asymptotically proportional to the matrix dimension, it is empirically observed that this number increases to a value which is proportional to $dim^{\sqrt{2}}$ during the solution process. The memory consumption is determined by this value. The number of floating point operations required for the solution is proportional to dim^2 which determines the computational effort of the solution process.

For a higher efficiency, the block tri-diagonality of the matrix could be exploited for the solution, which would involve the inversion of the block matrices. In case these inversion operations are carried out treating the blocks as full matrices, the computational effort would, however, even increase at an already reduced memory consumption. To make this approach more efficient, a sparse matrix inversion routine would be required. Dealing with this effort was not necessary for the current work that concentrates mostly on time-independent problems where the linear system of equations needs to be solved only once for every given physical problem. For the implementation of the heat diffusion equation in a time-dependent MHD code, the computational domain could also be split radially by the mixed implicit-explicit finite difference scheme described in Reference [Günter08], which allows to separate the single large system of equations into several smaller ones.

4.3. Coordinate Systems

Due to the favorable properties of the finite difference scheme that is described in detail in Section 4.2, it is possible to solve the heat diffusion equation using a coordinate system that is not exactly aligned to the magnetic field lines. Some adaptation of the coordinates to the physical problem is, however, still desirable to ease the spatial resolution requirements. For core plasma simulations, a coordinate system is employed in which the unperturbed magnetic flux surfaces coincide with $\rho = \text{const}$ coordinate surfaces (flux coordinates). Here, ρ denotes the radial coordinate. The magnetic field lines are straight lines in θ-ϕ space (straight field line coordinates), where θ and ϕ denote the poloidal and toroidal coordinate directions. A transformation to helical coordinates is performed for a rough coordinate alignment to the physical structures that need to be resolved. An overview over the coordinate systems used in this work is given in the following.

Section 4.3.1 briefly describes the numerical codes used for equilibrium reconstruction and the determination of the straight field line coordinates that are explained in Section 4.3.2. The adaptation of the coordinates to the physical problem is discussed subsequently. This includes an explanation of local radial grid refinement (Section 4.3.3) and of the transformation to helical coordinates (Section 4.3.4). The special coordinate system used for computations across the plasma boundary is described in Section 4.3.5. Some information about the definition of the minor radius in plasmas with a shaped cross-section is given in Section 4.3.6. Many additional details regarding tensor analysis, coordinate systems, and coordinate transformations may be found in Appendix A.

4.3.1. Equilibrium reconstruction

A coordinate system with flux coordinate properties and straight field line properties can be determined for a reconstructed plasma equilibrium. The package of numerical codes that is used in this work for the equilibrium reconstruction and the determination of the flux/straight field line coordinate systems for various plasma equilibria is described briefly in the following.

equilibrium reconstruction

A plasma equilibrium can be obtained from the ideal MHD equilibrium equations (→ Section 2.2) by minimizing the total plasma energy (magnetic plus thermal energies, "energy principle"). In this process, the flux surface shapes and positions are adjusted iteratively. The vacuum magnetic field of the toroidal field coils needs to be computed in advance and profiles for pressure and safety factor as they are known from the experiment must be prescribed. The last closed flux surface of the plasma region may either be specified in the code input ("fixed boundary") or determined by the energy minimizing algorithm ("free boundary"). The most important numerical codes required for the equilibrium reconstruction are given in the following. A flow-chart that gives an overview of the interplay between these equilibrium codes with the codes implemented for this work is shown in Appendix B.1.

energy principle

fixed boundary

free boundary

- Plasma equilibria reconstructed with the `CLISTE` code [McCarthy99a, McCarthy99b] are available for ASDEX Upgrade discharges. Due to the larger flexibility and the easier interaction with other codes, the `VMEC/NEMEC` code [Hirshman86a, Hirshman86b] is used in this work instead. It determines high-resolution plasma equilibria for a given vacuum magnetic field and pressure profile using the energy principle.

  VMEC/NEMEC Code

- The vacuum magnetic field that is required as an input to the `VMEC/NEMEC` code can be determined from the magnetic coil geometries and currents solving Biot-Savart's law by the `VACFIELD` code, which can carry out these computations for various different coil types [Strumberger05].

  VACFIELD Code

- The `VACFIELD` code can also be used to determine the magnetic field perturbations that are produced by resonant magnetic perturbation coils.

- The `COTRANS` code [Strumberger04] "translates" between the input and output formats of many different numerical codes. This involves, e.g., coordinate transformations. Here, it is used to extract the data required for the `MFBE` code from the output of the `VMEC/NEMEC` code ("mode 7").

- The `MFBE` code [Strumberger02] determines the equilibrium magnetic field inside and outside the plasma from the equilibrium data and the vacuum magnetic field ("equilibrium mode"). It is also possible to superpose magnetic perturbation fields that give rise to magnetic islands or stochastic field layers ("perturbation mode").

  MFBE Code

- Poincaré plots of equilibrium or perturbed magnetic field structures may be produced with the `GOURDON` code by tracing magnetic field lines [Gourdon].

  GOURDON Code

- The COTRANS code described above can extract the necessary coordinate Fourier modes that describe a straight field line coordinate system ("mode 11"). These coordinates are used as a basis for the computations in this work. As discussed in the following Section, several transformations are performed to adapt the coordinate system better to the requirements of the heat diffusion simulations.

4.3.2. Flux and Straight Field Line Coordinates

The axisymmetric toroidal coordinate systems used in this work with the radial, poloidal and toroidal coordinates ρ, θ, and ϕ can be defined by the transformation

$$R(\rho,\theta,\phi) = \sum_m \left\{ R_m(\rho)\sin[m\theta] + \tilde{R}_m(\rho)\cos[m\theta] \right\}, \tag{4.22}$$

$$Z(\rho,\theta,\phi) = \sum_m \left\{ Z_m(\rho)\sin[m\theta] + \tilde{Z}_m(\rho)\cos[m\theta] \right\}. \tag{4.23}$$

In the code, a more general transformation is implemented that may describe very general toroidal coordinates including coordinate systems without the flux and straight field line properties, non-axisymmetric coordinates as they would be adequate for stellarator geometries, and coordinates in which the $\phi = const$ surfaces are not planar, e.g., Boozer-Grad coordinates [Grad71, Boozer80]. The more general transformation is described in Appendix A.3. In most cases, flux coordinates with the straight field line property will be used in this work. The flux coordinate property ensures that apart from magnetic islands and stochastic layers, coordinate surfaces coincide roughly with flux surfaces. This coordinate choice is favorable, as most equilibrium quantities are virtually constant on flux surfaces. The straight field line property will be exploited in Section 4.3.4 to adapt the coordinates roughly to the physical problem. For this purpose, a further coordinate transformation is carried out which leads to an unsheared helical coordinate system that eases the toroidal resolution requirement. A radial grid meshing transformation for a local enhancement of the radial grid resolution is discussed in the following Section.

4.3.3. Radial Grid Meshing

The temperature distribution at magnetic islands features narrow structures that need to be resolved in numerical heat diffusion simulations. A method to locally enhance the radial resolution at a magnetic island or a stochastic field layer compared to the rest of the plasma (radial grid meshing) is therefore desirable. This is achieved by a coordinate transformation that increases the radial grid point density in a specific region where it is required for an accurate description of the physical problem and decreases the radial grid point density where a moderate resolution is sufficient. The transition between the regions with the different grid point densities is smooth such that the meshing transformation function and its first three derivatives are continuous.

grid meshing

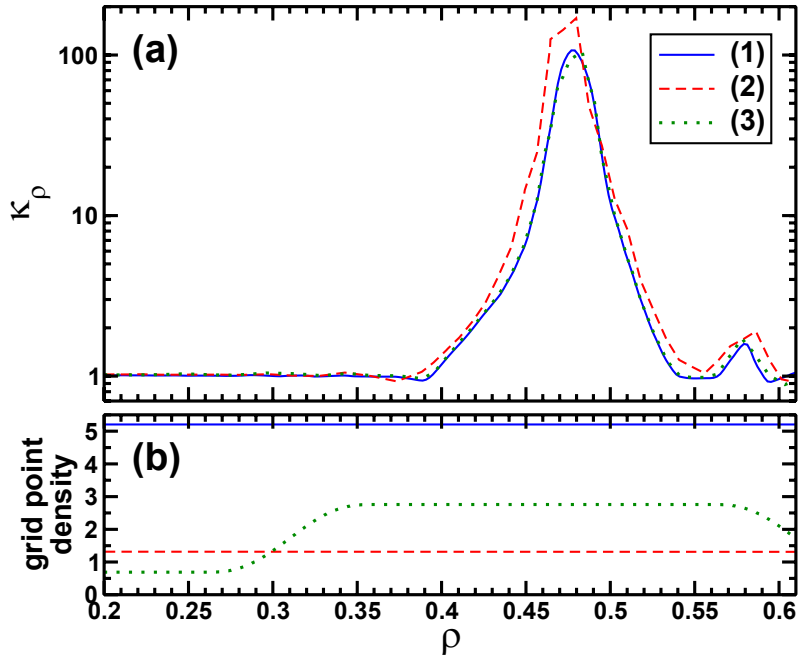

FIGURE 4.4. *For demonstrating the efficiency of radial grid meshing, the normalized effective radial heat diffusivity, $\kappa_\rho = \chi_\rho / \chi_\perp$, is plotted in Part **(a)** at a $^3/_2$ island in ASDEX Upgrade geometry with $\chi = 10^{10}$. Case (1) corresponds to 257 radial, 129 poloidal, and 23 toroidal grid points (reference run). For Case (2), the radial resolution was reduced to 65 points which causes significant errors. For Case (3), 65 radial grid points were used with an adequate grid meshing. The corresponding radial grid point densities are plotted in Part **(b)**.*

In this work, the default choice for the radial coordinate, ρ, is the normalized square-root of the equilibrium toroidal magnetic flux, Φ, which is similar to the definition of the minor radius described in Section 4.3.6. The definition of the toroidal magnetic flux is illustrated in Figure 2.1. Using a different radial coordinate does not require any changes in the heat diffusion code as no physical assumptions regarding the coordinate system were made. In particular, this allows to apply a radial coordinate transformation for grid meshing.

The effectiveness of grid meshing is demonstrated in Figure 4.4 at the example of a single $3/2$ magnetic island in ASDEX Upgrade. Results obtained for the effective normalized radial heat diffusivity, κ_ρ, with three different radial grids are shown. The complete plasma ($\rho = 0 \ldots 1$) is covered by the simulations and all three cases were performed with identical poloidal and toroidal resolutions. It is clearly visible from the Figure, that the grid meshing allows to resolve the magnetic island equally well as in the reference run with only one fourth of the total number of radial grid points.

It must be noted, that this example is somewhat artificial. In cases with one single island only, the computational regime would in practice be restricted to the vicinity of the magnetic island using appropriate boundary conditions rendering grid meshing less important. However, when the whole plasma needs to be resolved as several radially distinct magnetic islands shall be resolved, grid meshing is an essential technique to reduce the computational effort.

4.3.4. Helical Coordinates

Due to the fast parallel transport, the temperature distribution is very smooth along magnetic field lines. It is therefore helpful to align the coordinate system roughly to the field lines at magnetic islands which leads to larger gradient lengths in ϕ direction and allows to reduce the required toroidal resolution as will be demonstrated a bit later in this Section. The toroidal coordinate system can be transformed to a helical one by replacing $\zeta_m(\theta) = m\theta$ in Equations (4.22) and (4.23) by $m(\theta - \iota_c \phi)$. The transformation is determined by the choice for ι_c as discussed in the following:

- In the case $\iota_c = 0$, no transformation is performed such that the coordinate system remains purely toroidal.
- When a constant value

$$\iota_c \equiv \frac{\tilde{j}}{G_\theta} \tag{4.24}$$

  is selected, where G_θ denotes the poloidal grid point number and $\tilde{j}$ an arbitrary integer number, grid points at $\phi = 2\pi$ do match with grid points at $\phi = 0$. This allows to implement the toroidal periodicity condition very effectively while it still allows to align the basis vector $\mathbf{e}_\phi$ to the unperturbed magnetic field lines of the flux surface at which the rotational transform, ι, is equal to ι_c. A helical coordinate system according to Equation (4.24) is depicted in Figure 4.5.

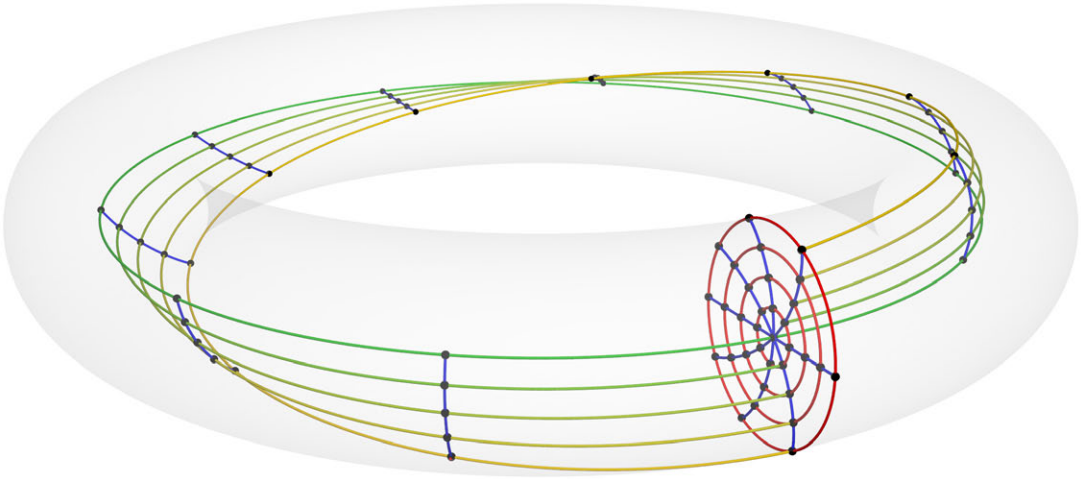

FIGURE 4.5. *The spatial grid structure of a helical coordinate system for the TEXTOR tokamak is illustrated, which is aligned to a $4/3$ island, i.e., $\iota_c = 3/4$. At $\phi = 0$, the grid point positions (black), the radial coordinate lines (blue) and the poloidal coordinate lines (red) are shown. Some toroidal coordinate lines are depicted (greenish) that wind helically around the torus and do not close into themselves after the toroidal turn, but match with different grid points.*

- A constant choice for ι_c different from Equation (4.24) means that the grid points at $\phi = 2\pi$ do not coincide with grid points at $\phi = 0$. Thus, an interpolation in θ-direction is required for the implementation of the toroidal periodicity condition which raises numerical errors as discussed below.

- If ι_c is chosen to be a function of ρ, the coordinate system gets sheared. This distorts the grid when moving once toroidally around the torus from $\phi = 0$ to 2π as the coordinate helicity is different on each flux surface. The grid distortion can be reduced by applying the coordinate transformation independently to toroidal sections (see Appendix A.3). Then, however, the interpolation for the implementation of the toroidal periodicity condition is required not only at $\phi = 2\pi$, but at each boundary between such toroidal sections.

Interpolation Error

Tests show that the numerical errors are increased strongly if an interpolation is required for the implementation of the toroidal periodicity condition or if the grid is distorted due to a sheared helical coordinate system. The interpolation is in fact an interpolation of unknowns: The unknown temperature at a virtual grid point at $\phi = 2\pi$ needs to be expressed by the unknown temperature values of real grid points at $\phi = 0$. Including various different numbers

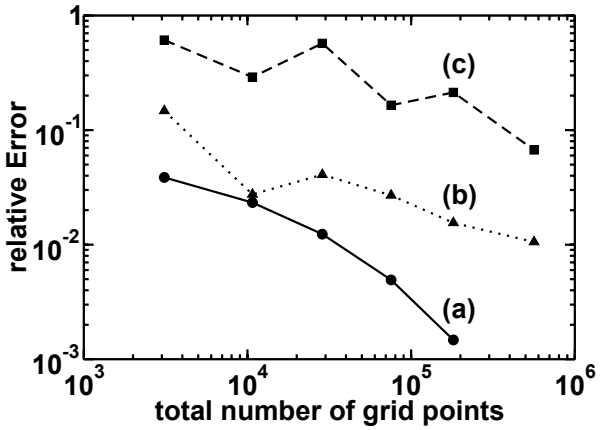

FIGURE 4.6. *The error in the poloidally and toroidally averaged temperature at $\rho = 0.3$ is plotted versus the total number of grid points in a configuration with an island at $\rho = 0.47$. For Case **(a)**, ι_c was chosen according to Equation (4.24). Case **(b)** corresponds to a constant value of ι_c for which an interpolation is necessary and for Case **(c)**, $\iota_c = \iota$ was used as coordinate helicity. Although the chosen heat diffusion anisotropy, $3 \cdot 10^7$, is rather moderate, the interpolation for the toroidal periodicity condition introduces large errors as seen from Case **(b)**. The grid distortion due to the coordinate shear increases the errors even further (Case **(c)**).*

of real grid points in the interpolation (one to eight) were tested. Three neighboring grid points, which turned out to be the best choice, are used for the following discussion.

The numerical errors caused by the interpolation are shown in Figure 4.6. Errors are increased by roughly one order of magnitude already at moderate heat diffusion anisotropies, if a constant value for ι_c is chosen that requires interpolation. When ι_c is chosen equal to the rotational transform, ι, that is a function of the radial coordinate, the coordinate system is aligned to the unperturbed magnetic field lines. This, however, means that the coordinates becomes sheared which increases the numerical error by another order of magnitude as a result of the grid distortion. A separate transformation in toroidal sections was also tried which reduces the distortion of the coordinate system but increases the required number of interpolations and cannot reduce the numerical errors altogether. As the errors caused by the interpolation and distortion turn out to be unacceptably large for realistic values of χ, only values for ι_c according to Equation (4.24) are used in practice.

Helical coordinates according to Equation (4.24) allow to implement the toroidal periodicity condition by virtual grid points as they are discussed in Section 4.2.3 with only slight modifications. The virtual grid points $[i, j, -1]$ are equivalent to the real grid points

$$\left[i, (j + \tilde{j}) \bmod G_\theta, G_\phi - 1\right]$$

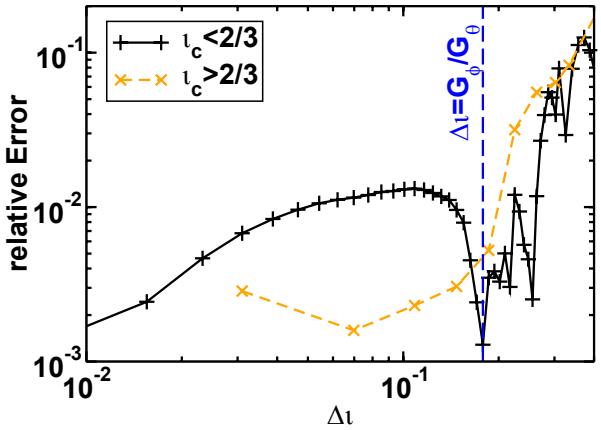

FIGURE 4.7. *The numerical error in the $^3/_2$ component of the temperature perturbation is shown at a large $^3/_2$ magnetic island vs. the misalignment $\Delta\iota$. The error becomes unacceptably large for $\Delta\iota \gtrsim G_\phi/G_\theta$.*

and the virtual grid points $[i, j, G_\phi]$ are equivalent to the real grid points

$$\left[i, (j - \tilde{j}) \bmod G_\theta, 0\right].$$

Such helical coordinates allow to align the coordinate system to the helicity of a magnetic island. In cases with several magnetic islands or stochastic field layers, the coordinate system may be aligned to the mean value of the rotational transforms of the islands which still reduces the toroidal resolution requirement significantly as made plausible in the following.

Misalignment Error

Using an unsheared helical coordinate system means that the coordinate system is exactly aligned to the magnetic field only on one surface, where the rotational transform, ι, coincides with the coordinate helicity, ι_c. For all other flux surfaces, the coordinate system is misaligned by the difference of the helicities,

$$\Delta\iota(\rho) = |\iota_c - \iota(\rho)|. \tag{4.25}$$

To investigate numerical errors, computations for a large $^m/_n = {}^3/_2$ magnetic island ($w = 6.3$ cm and $w/w_c = 7.7$) are performed with different values of ι_c. Figure 4.7 shows the numerical error in the $^3/_2$ Fourier component of the temperature normalized to the unperturbed temperature versus the coordinate misalignment $\Delta\iota$ at the island resonant surface. Fixed numbers of $129 \times 129 \times 23$ radial, poloidal, and toroidal grid points were used. A moderate increase of numerical errors is observed as $\Delta\iota$ increases, but at $\Delta\iota \approx G_\phi/G_\theta$, the error drops again. Here, the magnetic field is oriented exactly diagonally in the grid cells. For values of $\Delta\iota$ beyond

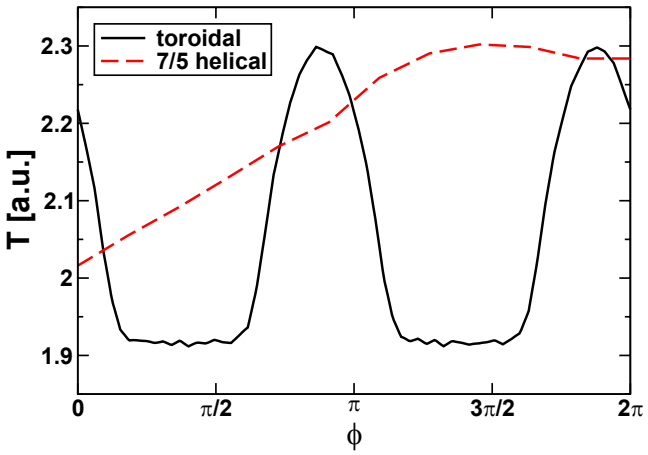

FIGURE 4.8. *Temperature features are shown for a $3/2$ magnetic island in ASDEX Upgrade at a heat diffusion anisotropy of 10^9. The solid curve corresponds to the temperature structures in purely toroidal direction, where steep gradients are visible that are computationally expensive to resolve. The dashed curve represents the temperature structures along a $7/5$ helical coordinate line where the gradient lengths are strongly increased. This allows to reduce the number of grid points in ϕ-direction significantly.*

that, errors increase very strongly, which implies the condition

$$\Delta\iota \lesssim \frac{G_\phi}{G_\theta} \tag{4.26}$$

for resolving magnetic islands well. For instance, when resolving $3/2$ and $4/3$ islands simultaneously, $G_\phi \gtrsim 0.05 \cdot G_\theta$ is the minimum requirement when choosing $\iota_c = 5/7$, while $G_\phi \gtrsim 0.75 \cdot G_\theta$ would be required in a purely toroidal coordinate system with $\iota_c = 0$.

Resolving Toroidal Temperature Structures

The resolution of the narrow temperature structures at magnetic islands leads to the requirement of a high toroidal resolution. However, a rough alignment of the coordinate system to the helicity of the magnetic island can broaden the width of these structures in ϕ-direction such that a considerably lower resolution becomes sufficient. This is demonstrated in Figure 4.8 which shows the temperature structures at a $3/2$ magnetic island in ASDEX Upgrade along the toroidal direction and along a $7/5$ helical coordinate line. The number of toroidal grid points required for resolving the temperature structures is obviously much lower in the helical coordinate system. The $7/5$ coordinate system is misaligned with respect to the island by $\Delta\iota = 0.048$ compared to a misalignment of $\Delta\iota = 0.667$ for the purely toroidal coordinates.

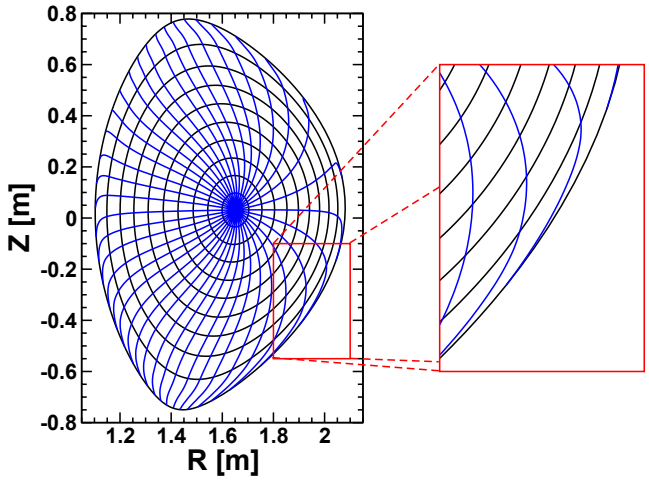

FIGURE 4.9. *The structure of the straight field line coordinate system for an ASDEX Upgrade equilibrium is shown. It can clearly be seen, that the poloidal resolution is reduced at the plasma boundary on the low field side. Additionally, the poloidal and radial coordinate lines become almost parallel close to the separatrix. Due to these drawbacks, the coordinate system is not adequate for examinations at the plasma boundary.*

Many additional details regarding the helical coordinate systems are found in Appendix A.3. Transformations between coordinate systems are frequently required during the evaluation of the numerical data. The transformation from curvilinear to cylindrical coordinates can simply be performed using Equations (4.22), and (4.23). However, no explicit expression can be given for the inverse transformation wherefore it needs to be performed by an iterative method. An algorithm described in Appendix A.4 was implemented for that purpose.

4.3.5. Coordinates for the Plasma Edge

The straight field line coordinate system used for the core plasma is not well-suited for edge computations. At the low field-side close to the separatrix, it has an insufficient poloidal resolution and the radial and poloidal coordinate lines are almost parallel as illustrated in Figure 4.9. At the plasma separatrix, the coordinate system breaks down due to field line stagnation at the X-point of the plasma configuration. Furthermore, the coordinate system does not need to be transformed to a helical one for examinations regarding the plasma boundary as the rotational transform of the field lines is rather small meaning that they are oriented predominantly in toroidal direction. For these reasons, a different coordinate system is used for computations at the plasma boundary.

In these coordinates, θ is taken to be the real poloidal angle with respect to the magnetic axis. The $\rho = \text{const}$ surfaces are flux surfaces up to the radial position $\rho = \rho_{cut}$ (about 1 cm

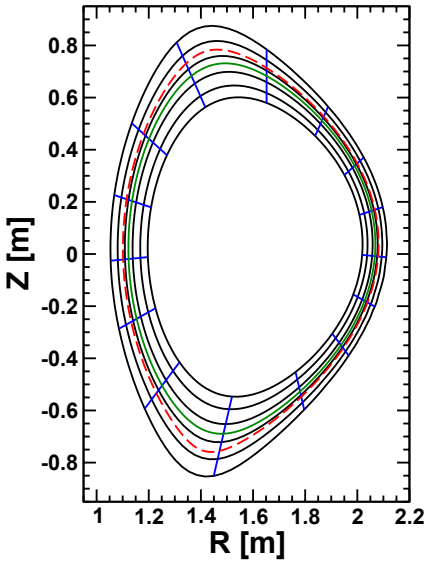

FIGURE 4.10. *The special coordinate system used for computations across the plasma boundary is depicted. In contrast to the straight field line coordinates shown in Figure 4.9, it has a consistent poloidal resolution and the angle between the poloidal and radial coordinate lines is close to a right angle everywhere. The green line indicates the radial surface, from which the coordinate system is continued continuously outwards ($\rho = \rho_{cut}$). Outside this surface, the radial coordinate surfaces do not coincide with flux surfaces any more. The red line corresponds to the last closed magnetic surface of the plasma equilibrium.*

inside the separatrix). Beyond that, a linear extrapolation of the coordinate Fourier modes R_m, $\tilde{R}_m$, Z_m, and $\tilde{Z}_m$ is performed to continue the coordinate system into the vacuum region. The resulting coordinate system for an ASDEX Upgrade equilibrium is shown in Figure 4.10. This special coordinate system is used for the heat diffusion simulations across an ergodic plasma boundary that are presented in Section 8.4.

4.3.6. Minor Radius

In periodic cylindrical geometry, the straight-forward choice for a radial coordinate is the minor radius that is defined as the distance to the magnetic axis. In toroidal plasmas where the radial coordinate surfaces are not concentric due to the Shafranov shift and may additionally be shaped (elongation, triangularity), the radial coordinate choice is not that obvious. There are many possible flux labels that assign a unique number to each flux surface and can be chosen as a radial coordinate. For example, the toroidal flux, Φ, through the area that is enclosed by the magnetic flux surfaces may be used ($\rightarrow$ Figure 2.1). The volume inside the flux surfaces is also a possible choice. For the axi-symmetric tokamak equilibria considered in

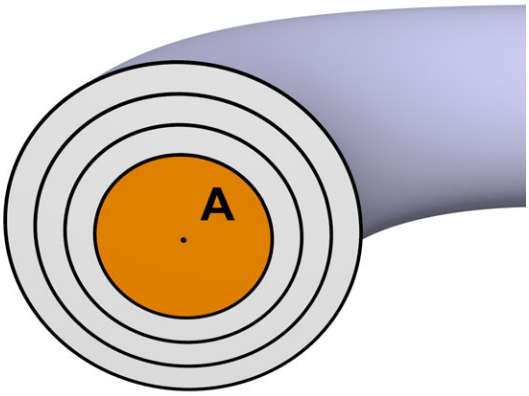

FIGURE 4.11. *The surface A enclosed by a flux surface within a poloidal cross-section can be used as a flux label for tokamak plasmas. Another choice is the toroidal magnetic flux through this surface.*

this work, the surface, A, that is enclosed by the flux surfaces within a poloidal cross-section may be used (→ Figure 4.11). A generalized minor radius,

$$r(\rho) = \sqrt{A(\rho)/\pi}, \tag{4.27}$$

can be deduced. With this definition of the minor radius, effects like heat transport across magnetic islands may be compared directly to cylindrical results. The critical island width for temperature flattening, w_c, can be determined analogously to the cylinder from Equation (2.43). The island width, w, can be determined by

$$w = r^{isl}_{max} - r^{isl}_{min} = r\left(\rho^{isl}_{max}\right) - r\left(\rho^{isl}_{min}\right), \tag{4.28}$$

where ρ^{isl}_{max} and ρ^{isl}_{min}, respectively, denote the maximum and minimum values the radial coordinate, ρ, takes on the island separatrix.

4.4. Implementation

In this Section, some information is given on the implementation of the heat diffusion equation in two different numerical codes. The `TEMPRO` code discussed in Section 4.4.1 solves this equation in periodic cylindrical coordinates, while the `HEATs` code was written for general toroidal geometries and is described in Section 4.4.2. The information given here is kept very concisely and is intended only for a quick overview. A comprehensive documentation is available for the toroidal `HEATs` code with its source code.

These two major codes as well as a variety of auxiliary codes for special purposes are

written in the Fortran 90/95 programming language. The documentation of the HEATs code was created using the open-source tool Doxygen. Different code revisions were managed with the open-source revision control system Subversion. Data evaluation and the generation of figures were performed using Matlab, IDL, Grace, Python and other tools.

4.4.1. Cylindrical Code

For the comparison to analytical theories that are usually valid for the periodic cylinder, the TEMPRO code was implemented. It solves the steady state anisotropic heat diffusion equation in cylindrical coordinates. A Fourier decomposition is applied in "toroidal" direction, i.e., along the cylinder and the finite difference scheme described in Section 4.2 is used in its two-dimensional form for the radial and poloidal directions. For a rough adaptation of the coordinate system to the physical problem, a radial grid meshing as well as a transformation to helical coordinates are implemented. These methods are discussed in Sections 4.3.3 and 4.3.4.

4.4.2. Toroidal Code

More realistic simulations for toroidal devices may be performed with the HEATs code that solves the steady state anisotropic heat diffusion equation in general toroidal geometries. The time-dependent heat diffusion equation was implemented for demonstration purposes (→ Section 4.4.4). For the rest of the work, time-dependencies are, however, neglected as the magnetic field evolution is slow enough in most cases such that the temperature distribution can virtually immediately adapt to these changes due to the fast parallel transport.

In the HEATs code, the three-dimensional version of the finite difference scheme described in Section 4.2 is implemented. The code is written such that it can deal with arbitrary toroidal coordinate systems including non-axisymmetric ones (→ Section 4.3). This work, however, is restricted to axisymmetric tokamak simulations. It is optionally possible to solve the heat diffusion equation for the whole plasma region or for a certain radial region only. With a specially designed coordinate system (→ Section 4.3.5), even simulations across the boundary of divertor plasmas are feasible. A "natural" boundary condition is available for the plasma core. Dirichlet and Neumann boundary conditions were implemented for both radial borders of the computational regime (→ Section 4.2.3).

The linear system of equations that results from the discretization of the heat diffusion equation is solved implicitly with a direct solution technique using the Watson Sparse Matrix Package (WSMP) as discussed in Section 4.2.5. The HEATs code writes out the computational results in a special binary "raw data format" using the Fortran module mod_state that was written for this purpose[2]. The raw computational data needs to be post-processed to extract the relevant physical information that can differ from case to case. For example, temperature cuts along certain lines in the plasma, two-dimensional plots of the heat flux density, or information

[2]For overview of the Fortran modules that were implemented to provide certain datastructures and methods frequently used not only by the HEATs code but also by many auxiliary codes, refer to Appendix B.2.

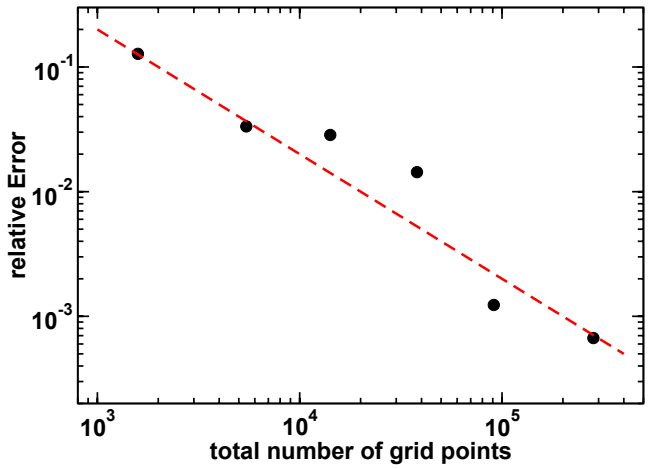

FIGURE 4.12. *The convergence of the numerical scheme is demonstrated for a large 3/2 magnetic island ($w = 8.5$ cm) in ASDEX Upgrade at a heat diffusion anisotropy of $\chi = 3 \cdot 10^8$.*

about the metric tensor can be extracted with the post-processing code `POSTPROC` that was implemented for this task[3].

4.4.3. Convergence

In the following, the convergence of the numerical scheme is demonstrated on the example of a single 3/2 magnetic island in ASDEX Upgrade. The relative error of the core plasma temperature is plotted in Figure 4.12 versus the total number of grid points. For this convergence study, the resolution was increased from $23 \times 23 \times 3$ grid points to $129 \times 129 \times 17$ in steps (radial $\times$ poloidal $\times$ toroidal). An additional reference run was performed at a resolution of $181 \times 181 \times 23$ points for estimating the relative errors for these runs. The error can be seen to decrease by a factor of roughly 200 as the resolution per coordinate direction rises by a factor of about six as it is expected for the second order accurate numerical method.

4.4.4. Time-Dependent Simulations

In this Section, the capability of the numerical scheme to solve time-dependent problems is quickly demonstrated rather as a general prove of principle than a physically relevant application. The computation is performed for a 2/1 island in the TEXTOR tokamak with an island width of 7 cm and a heat diffusion anisotropy of 10^8. The computational regime ranges from $\rho = 0.4$ where Neumann boundary conditions are applied to $\rho = 0.8$ where Dirichlet boundary

[3]This tool has some simple scripting features which allow to easily extract the same kind of information from several computations. Details about this tool are found in Appendix B.3.

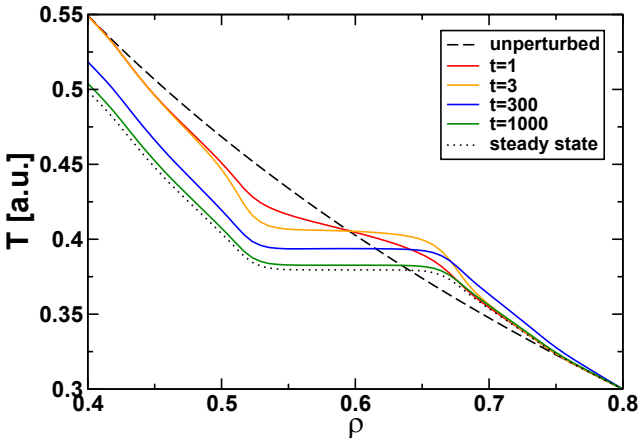

FIGURE 4.13. *The time-evolution of the radial temperature profile across the O-point of a "suddenly" arising magnetic island is shown. Temperatures and times are given in arbitrary units. On a very short time-scale (less than* 10 *time-units), the temperature inside the magnetic island flattens. It takes, however, at least* 1000 *time-units until the core temperature has dropped to the steady-state level.*

conditions are used. It is assumed that the unperturbed equilibrium is suddenly perturbed by a large $^2/_1$ magnetic island at $t = 0$. Subsequently, the magnetic field with the island remains static. In reality, magnetic islands grow on the rather long time scale of several milliseconds.

The evolution of the radial temperature profile across the O-point of the island is shown in Figure 4.13. The temperature distribution adjusts gradually to the new magnetic field structure. It can be seen, that the flattening of the temperature distribution inside the magnetic island takes place very quickly due to the fast parallel transport, while the drop of the core temperature that results from the deteriorated energy confinement takes two to three orders of magnitude longer.

Chapter 5.

Magnetic Islands

In this Chapter, heat diffusion across single magnetic islands is investigated. We first concentrate on islands in cylindrical geometry, which already allows to highlight the most important issues. The basic characteristics of heat transport across magnetic islands and the resulting temperature flattening are discussed in Section 5.1. The temperature flattening brings about a degradation of the energy confinement properties of the plasma which leads to a reduction of the plasma core temperature. This is discussed in Section 5.2. Afterwards, the heat transport across single magnetic islands in cylindrical and toroidal geometries is briefly compared in Section 5.3. The temperature peaking that arises around the O-point of magnetic islands in response to local heating power deposition is discussed in Section 5.4. The driving term of neoclassical tearing modes due to the bootstrap current perturbation caused by magnetic islands is examined in Section 5.5 and the results are compared to analytical predictions. Chapters 6 and 7 are also concerned with heat transport across magnetic islands. There, measurements at the tokamak experiments TEXTOR and ASDEX Upgrade are compared to numerical simulations aiming at the determination of the experimental heat diffusion anisotropy.

Contents

5.1. Basic Heat Transport Properties

The temperature distribution inside magnetic islands flattens to a degree that depends on the ratio between w and w_c as discussed in Section 2.5.3. With increasing values of w/w_c, the temperature flattening occurs first in a region around the island O-point and gradually extends towards the island separatrix for yet larger values of w/w_c. In the following, this is demonstrated for a $3/2$ magnetic island with $w = 0.113a$ in a periodic cylinder, where a denotes the

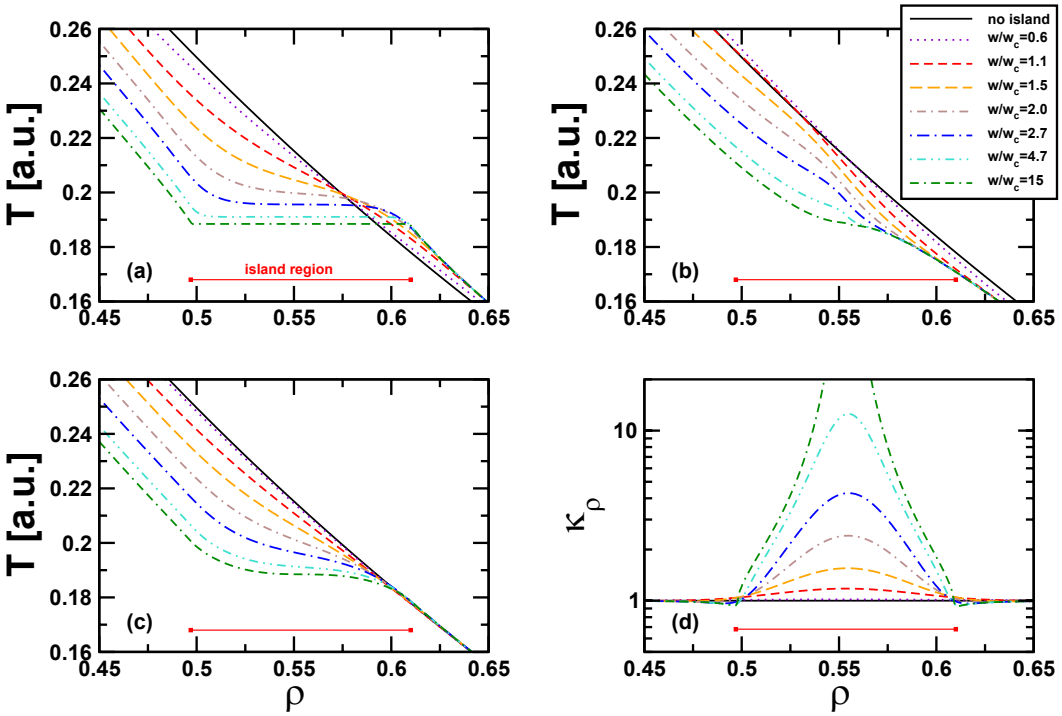

FIGURE 5.1. *Results for heat transport across a* $3/2$ *magnetic island in periodic cylindrical geometry are shown.*
Part ***(a)*** *contains radial temperature profiles across the O-point of the island.*
Part ***(b)*** *contains radial temperature profiles across the island X-point.*
Part ***(c)*** *shows the profile of the poloidally and toroidally averaged temperature.*
Part ***(d)*** *gives the effective normalized radial heat diffusivity.*

minor plasma radius. In this geometry, magnetic islands can be treated as a two-dimensional problem which makes it easier than in the torus to resolve even unrealistically large values of w/w_c. This is useful when the large island limit is considered for comparisons to analytical theories. Furthermore, the absence of poloidal mode coupling (→ Section 2.2.3) allows to concentrate on single island effects as no secondary islands arise and no stochastisation occurs for single helicity magnetic perturbations.

Now, heat transport across a single island is investigated for different values of w/w_c by varying the heat diffusion anisotropy, $\chi_{||}/\chi_{\perp}$, and keeping the island width fixed. Radial temperature profiles across the island O-point are depicted in Figure 5.1a. For $w/w_c \lesssim 1$, almost no temperature perturbation occurs. When $w/w_c \gtrsim 2$, the temperature profile starts to flatten at the O-point and for $w/w_c \gtrsim 4$, the flattening has extended almost till the island separatrix. Figure 5.1b shows radial profiles of the temperature distribution across the X-point of the magnetic island. For increasing values of w/w_c, the radial temperature gradient at the island X-point continuously steepens while the width of the region where the temperature gradient is increased narrows. For a flattening of the temperature distribution around the X-point of the magnetic island, much larger values of w/w_c are required than around the O-point. This results from the field line stagnation described in Section 2.5.3 that renders parallel heat transport less efficient in the vicinity of the island X-point.

The radial profile of the toroidally and poloidally averaged temperature, $T_{0/0}$, is given in Figure 5.1c. The gradient of $T_{0/0}$ is reduced significantly in the island region for $w/w_c \gtrsim 2$ and not affected far from the island. However, $T_{0/0}$ does not flatten completely in the whole island region even for extremely large values of w/w_c. Thus, the magnetic island size could easily be underestimated from the average temperature profile that is measured by diagnostics with a low temporal resolution. The island locally increases the effective radial heat transport which leads to a degradation of the overall energy confinement and a drop of the plasma core temperatures which will be investigated in more detail in Section 5.2.

The radial heat transport across an island can be studied from the values of the normalized effective radial heat diffusivity,

$$\kappa_\rho = \frac{\chi_\rho}{\chi_\perp} = \frac{\partial T_{unpert}/\partial \rho}{\partial T/\partial \rho}. \tag{5.1}$$

The increase of κ_ρ relative to the equilibrium configuration is denoted by

$$\kappa_\rho^+ = \frac{\chi_\rho - \chi_\perp}{\chi_\perp} = \kappa_\rho - 1. \tag{5.2}$$

The value of κ_ρ is plotted in Figure 5.1d. The effective radial heat diffusivity is increased in the whole island region and the strongest enhancement is observed at the resonant surface of the magnetic island. Just outside the island separatrix, κ_ρ takes values slightly below unity which indicates an, at first glance surprising, localized reduction of the effective radial heat transport below the value of the equilibrium configuration. This can be explained by the dis-

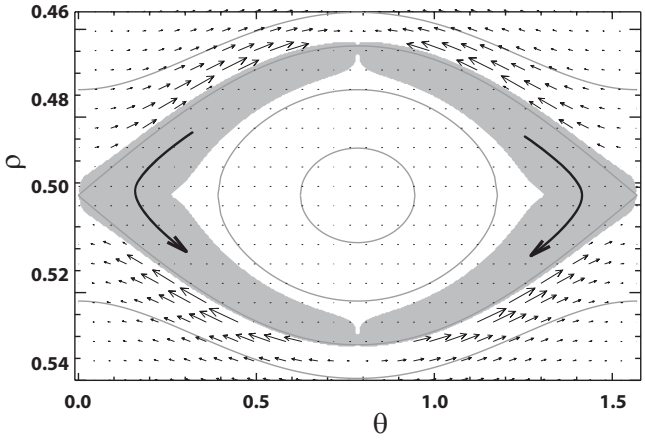

FIGURE 5.2. *The heat conduction layer of a magnetic island is shown, shaded in gray. Heat is transported through it as sketched by the two large arrows. Outside the heat conduction layer, the parallel heat flux is oriented opposite to the direction of the heat conduction layer. There, the parallel transport redistributes the heat flux within the flux surfaces. It has a small component that is directed radially inwards, towards the plasma core. Thus it locally counteracts the perpendicular transport, which leads to a slight reduction of the effective radial heat transport as seen in Figure 5.1d.*

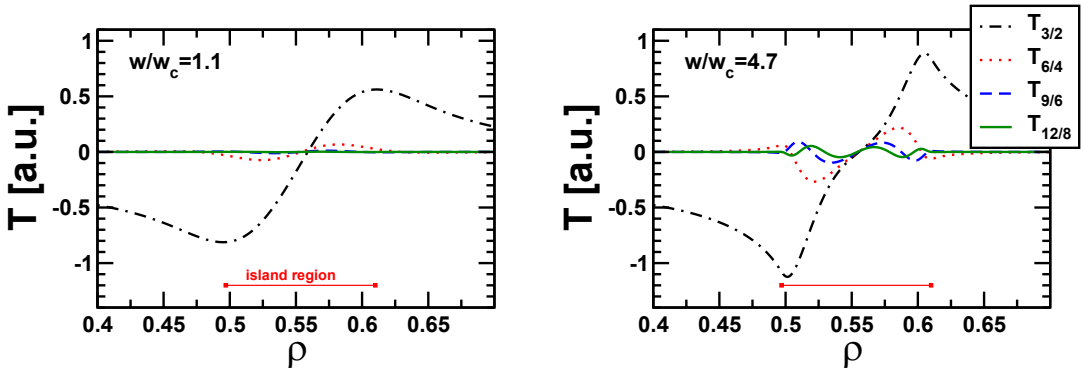

FIGURE 5.3. *The first four temperature harmonics at a $3/2$ magnetic island are shown at two different ratios of w/w_c. The higher harmonics are excited only inside the island region and are very weak for $w/w_c \lesssim 2$.*

tance between flux surfaces outside the island. The distance between the surfaces is smallest in the O-point region and largest in the X-point region (→ Figure 2.5). Thus, perpendicular transport across the surfaces is fastest in the O-point region. As a result, heat is redistributed within the flux surfaces outside the island by parallel transport along magnetic field lines. This parallel heat flux has a small component that is directed radially inwards and thereby locally counteracts the perpendicular transport. This is illustrated in Figure 5.2 for a $3/2$ island with $w/w_c = 6$. Consequently, the effective radial heat diffusivity is slightly reduced below the equilibrium value in this region. This effect is similar on the in- and outboard sides of the magnetic island and becomes significant only for $w/w_c \gtrsim 2$.

Fourier modes of the temperature perturbation to the $T_{0/0}$ profile can be determined from

$$T_{m/n}(\rho) = \frac{1}{4\pi^2} \int_0^{2\pi} d\theta \int_0^{2\pi} d\phi \;\; T(\rho,\theta,\phi) \cdot \cos(m\theta - n\phi). \tag{5.3}$$

The first four temperature harmonics at a $3/2$ magnetic island, $T_{3/2}$, $T_{6/4}$, $T_{9/3}$, and $T_{12/4}$, are presented in Figure 5.3 for two different ratios of w/w_c. The higher harmonics ($6/4$, $9/3$, and $12/4$) are only excited notably, if the temperature profile inside the island flattens significantly ($w/w_c \gtrsim 2$). These higher modes are observed virtually only inside the island while the first temperature harmonic extends far beyond the island separatrix.

5.2. Confinement Degradation

The flattening of the temperature profile at a magnetic island deteriorates the energy confinement properties of the plasma. In the simplest picture, the so-called belt model, the poloidally and toroidally averaged temperature profile flattens completely in the radial domain of the island [Chang90]. The core temperature is therefore reduced by the width of the island multiplied by the value of the unperturbed temperature gradient at the resonant surface,

belt model

$$\Delta T_{core,belt} = w \cdot \left[\frac{\partial T_{unpert}}{\partial r} \right]_s . \tag{5.4}$$

Figure 5.4 gives numerical results for the drop of the core temperature due to a magnetic island normalized to $\Delta T_{core,belt}$ versus the ratio of w/w_c. The numerical simulations show, that the core temperature drop, ΔT_{core}, does not exceed $0.7 \cdot \Delta T_{core,belt}$ even for islands with very large ratios of w/w_c, as the average temperature profile never flattens completely in the whole island region (→ Figure 5.1c). Empirically, the observed reduction of the plasma core temperature due to the magnetic island can be described quite accurately by

$$\Delta T_{core} = 0.7 \cdot \Delta T_{core,belt} \cdot \left[\frac{1}{1 + 0.12(w/w_c)^2 + 0.06(w/w_c)^3} - 1 \right]. \tag{5.5}$$

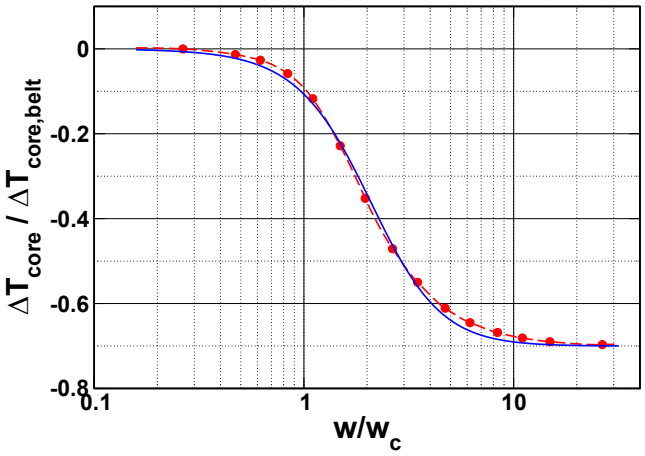

FIGURE 5.4. *Magnetic islands cause a degradation of the energy confinement which leads to a reduction of the plasma core temperature. The drop of the core temperature normalized to the belt model prediction is shown as obtained from numerical simulations for a magnetic island in cylindrical geometry. Even for very large values of w/w_c, the energy confinement degradation does not exceed 70% of the belt model prediction as $T_{0/0}$ does not flatten completely at the island. The solid line corresponds to an empirical fit to the data that is given by Equation (5.5).*

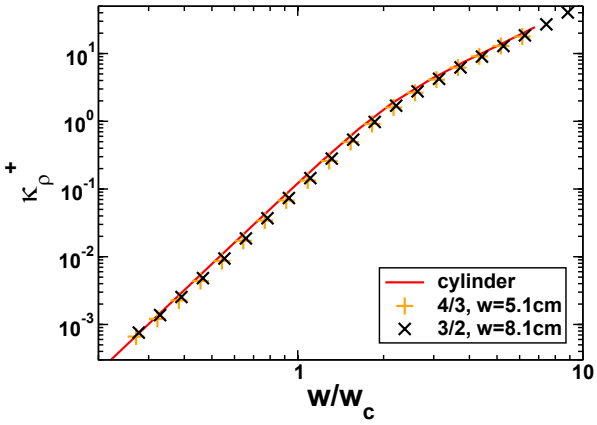

FIGURE 5.5. *The increase of the effective radial heat diffusion coefficient, κ_ρ^+, at the resonant surfaces of several magnetic islands is compared. The two cases for ASDEX Upgrade geometry show almost perfect agreement. They differ from cylindrical computations by up to 25 percent while showing qualitative agreement.*

5.3. Heat Transport in Tokamak Geometry

Heat transport across single magnetic islands is similar in cylindrical and toroidal geometries. To show that, the increase of the normalized effective radial heat diffusivity, κ_ρ^+, caused by an island is considered at its resonant surface. Figure 5.5 shows κ_ρ^+ as a function of w/w_c for two different island cases in toroidal ASDEX Upgrade geometry and compares the results to periodic cylindrical geometry, where κ_ρ^+ is known to depend on w/w_c only. Almost perfect agreement is observed between the two toroidal cases which indicates that island heat transport in toroidal geometry also depends on w/w_c only. The comparison to cylindrical results reveals differences up to 25 percent. These are probably caused by plasma shaping and differing "local" values of w/w_c at the low and high field sides of the torus.

Two different regimes can be identified for, both, cylindrical and toroidal results: $\kappa_\rho^+ \propto [w/w_c]^4$ for small values of w/w_c and $\kappa_\rho^+ \propto [w/w_c]^2$ for large values of w/w_c. Both regimes are separated by a transition region at $w/w_c \approx 1 \ldots 4.5$. These results are in good agreement with previous analytical and numerical observations in cylindrical geometry [Fitzpatrick95, Yu06]. Thus, heat transport across single islands is qualitatively and quantitatively similar in toroidal and cylindrical geometries.

For comparisons to experimental measurements, the differences between the low and high field sides are, however, of importance. Furthermore, in toroidal geometries even a single helicity magnetic perturbation can trigger multiple islands due to the excitation of harmonics by poloidal mode coupling (→ Section 2.2.3). When such islands overlap, ergodization can arise. In these cases, heat transport in toroidal and cylindrical geometries is fundamentally different. These effects are restricted to cases where the magnetic islands lock to each other. Otherwise, plasma currents form in the differentially rotating plasma that shield the magnetic perturbations. For perturbations produced externally by magnetic coils, the shielding by the plasma depends on the rotation of the plasma at the respective resonant surfaces relative to the external perturbation.

The temperature distribution and the heat flux density at a $3/2$ magnetic island in ASDEX Upgrade geometry are shown in Figure 5.6. Two-dimensional (radial and poloidal) contour plots of the temperature distribution and of the associated heat flux density at the magnetic island are given for a large $3/2$ magnetic island with an island width of about 13 percent of the minor radius. Figure 5.6a – c correspond to different values of the heat diffusion anisotropy and thus also of w/w_c. Clearly, at $w/w_c \gtrsim 2$, the temperature profile flattens around the island O-point and the flattened region gradually extends towards the island separatrix with increasing values of w/w_c. Accordingly, the heat flux across the magnetic island chain becomes localized to a thin heat conduction layer which is positioned around the island separatrix for large values of w/w_c. The heat flux intensities are considerably larger at the high field side (around $\theta = \pi$) than at the low field side (around $\theta = 0$) of the torus.

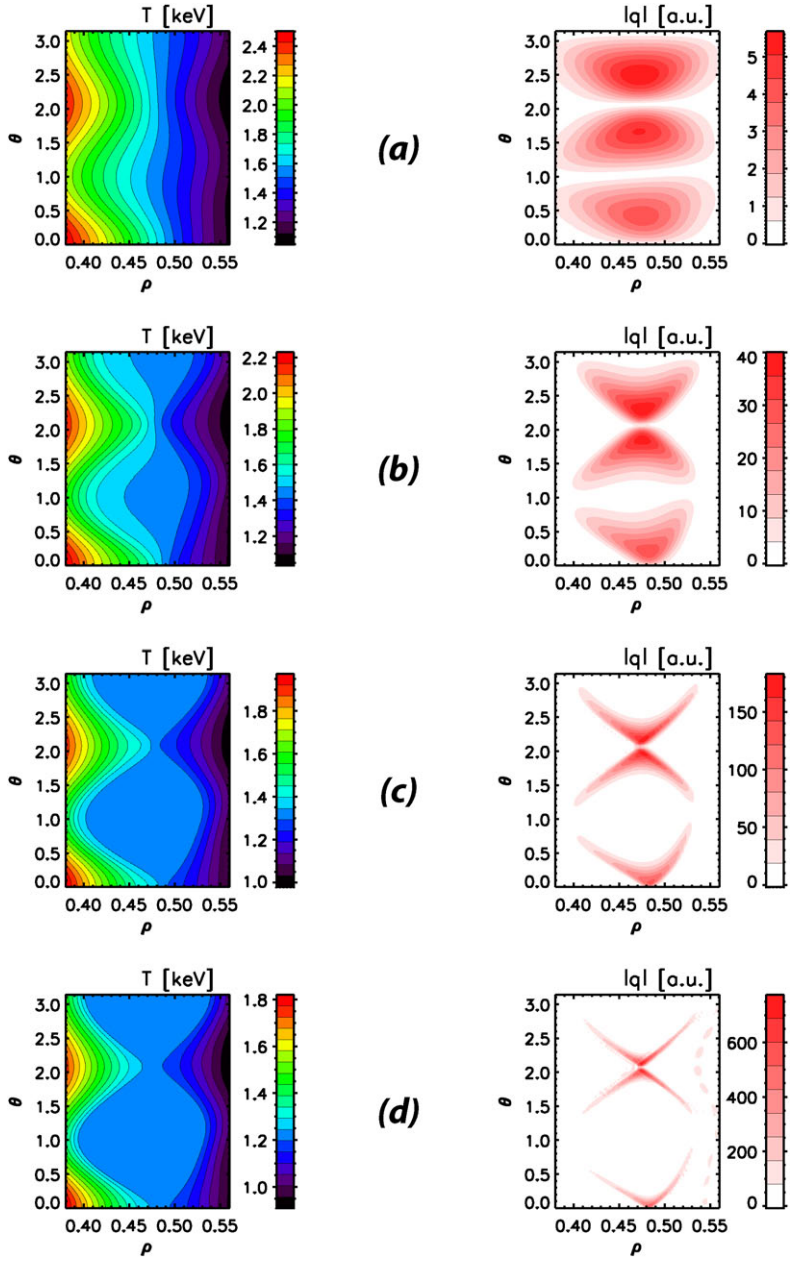

FIGURE 5.6. *Contour plots of the temperature (left) and the heat flux density (right) at a* $3/2$ *island in ASDEX Upgrade with* $w = 8.5$ cm *are shown. Results are given for* ***(a)*** $\chi = 3 \cdot 10^5$ *and* $w/w_c = 1.1$*, for* ***(b)*** $\chi = 4 \cdot 10^6$ *and* $w/w_c = 2.1$*, for* ***(c)*** $\chi = 7 \cdot 10^7$ *and* $w/w_c = 4.2$*, and for* ***(d)*** $\chi = 1 \cdot 10^9$ *and* $w/w_c = 8.4$*. The low and high field sides are located around* $\theta = 0$ *respectively* $\theta = \pi$*.*

5.4. Local Temperature Peaking

Similar to the nested magnetic flux surfaces of tokamak equilibria, magnetic islands can confine heat. Therefore, the temperature distribution peaks at the O-point of a magnetic island in the presence of a local heat source. The degree of peaking depends on the strength of the local heat sources and on the value of the cross-field heat diffusion coefficient, $\chi_\perp$. Ohmic and NBI heat sources are usually rather weak at the position of a magnetic island, but can already cause some temperature peaking. In case of a systematic heat deposition into the island by ECRH, the temperature peaking can get quite pronounced. This is made use of for island suppression as discussed in Section 3.2.2. It also gives the opportunity to determine the perpendicular heat diffusion coefficient inside the island as the peaking is proportional to $\chi_\perp$. For this purpose, analogously to Chapters 6 and 7, numerical simulations could be compared to ECE-measurements at an island with significant temperature peaking. Such an investigation is planned to be carried out in the future (→ Chapter 9).

In the following, the temperature peaking is demonstrated for a $3/2$ magnetic island in ASDEX Upgrade geometry. Simulations are performed for ECRH heat deposition at the resonant surface of the $3/2$ island with $w = 8.5$ cm at a heat diffusion anisotropy of 10^8. Figure 5.7 shows poloidal temperature cuts at different radial positions with an assumed ECRH deposition width of 1.5 cm. The dependency of the temperature peaking on the deposition width is demonstrated in Figure 5.8, where the poloidal temperature distribution at the island resonant surface is given for deposition widths between 0.8 cm and 6 cm. The temperature peaking, i.e., the difference between the temperature at the O- and X-point of the island, is reduced by 40% due to the increased deposition width. In current tokamak experiments, the deposition width can be altered by the toroidal launching angle of the ECRH system and is typically of the order of few centimeters [Maraschek07].

5.5. Neoclassical Tearing Modes

The flattening of the temperature profile inside a magnetic island leads to a helical perturbation of the bootstrap current which enhances the island growth rate in conventional tokamaks. Islands destabilized by this contribution are called neoclassical tearing modes (→ Sections 2.6 and 3.2). The growth rate of an NTM is $dw/dt \propto \Delta' + \Delta_{bs}$, where Δ' is the classical tearing stability index and Δ_{bs} the contribution from the pressure perturbations. Additional contributions that may affect the island stability, e.g., the ion polarization current, are neglected in this Section.

For cylindrical geometry, Fitzpatrick investigated Δ_{bs} analytically in the limiting cases of very large ($w/w_c \to \infty$) and very small islands ($w/w_c \to 0$) and performed an analytical match-

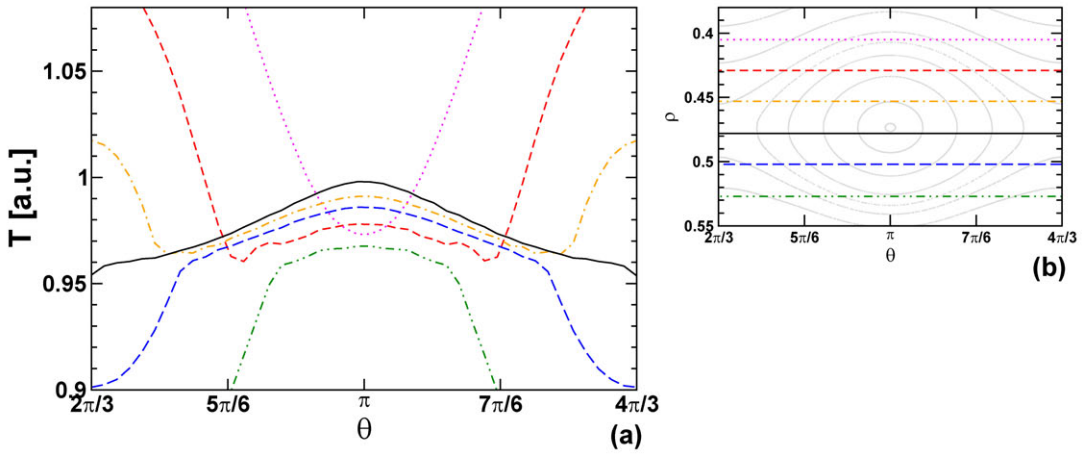

FIGURE 5.7. *The local temperature peaking inside a $^3/_2$ magnetic island in ASDEX Upgrade with $w = 8.5$ cm is shown at a heat diffusion anisotropy of $3 \cdot 10^8$. The peaking is caused by a heat source that is localized to the island resonant surface with a deposition width of 1.5 cm. Part* ***(a)*** *gives poloidal temperature cuts at six different radial positions. Part* ***(b)*** *shows the Poincaré plot of the island structure and the corresponding lines along which the temperature is determined.*

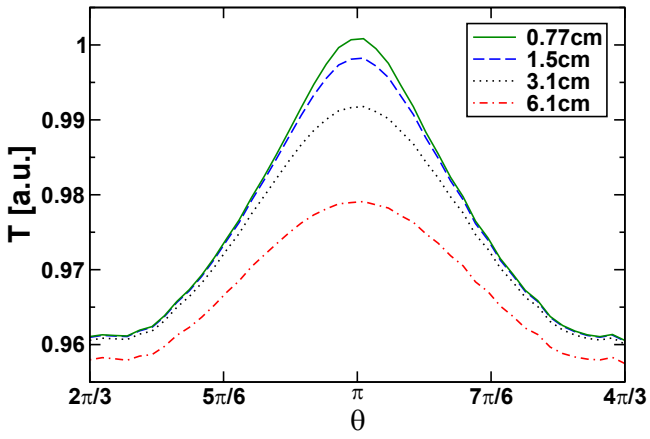

FIGURE 5.8. *The dependence of the temperature peaking at a magnetic island on the deposition width of the heat source is shown. The poloidal temperature distribution at the resonant surface of the island ($\rho = 0.476$) is plotted for four different deposition widths. Apart from the deposition width, all parameters are the same as for the case shown in Figure 5.7.*

ing between these limits leading to the contribution

$$\Delta_{bs} = 9.26\mu_0 \sqrt{\frac{R_0^3}{r_s}} \frac{q_s^3}{q_s'} \frac{p_s'}{B_\phi^2} \frac{w}{w^2 + w_d^2} \tag{5.6}$$

to the island growth rate [Fitzpatrick95]. Here, B_ϕ denotes the toroidal field strength, p_s' the equilibrium pressure gradient at the resonant surface, q_s the resonant value of the safety factor, q_s' its gradient, and $w_d = 1.8 w_c$.

Numerical simulations are presented in the following, that allow to test the validity of Equation (5.6) for realistic island sizes in between of the small and large island limits. For this purpose, the bootstrap current induced contribution to the island drive, Δ_{bs}, is calculated analogously to Fitzpatrick's analytical approach, but from numerically obtained temperature distributions. The computations are performed in periodic cylindrical geometry assuming a flat density profile and cold ions to allow for a direct comparison to analytical theory. Figure 5.9 shows the normalized contribution of the temperature flattening to the island drive versus the ratio of w/w_c for three different $3/2$ and one $4/3$ island case. The island widths are kept fixed in each case while the heat diffusion anisotropy is varied to modify the values of w/w_c. The numerical results agree very well with the analytical theory in the small ($w/w_c \ll 1$) and large island limits ($w/w_c \gg 1$). A large discrepancy of up to 56 percent is, however, observed at realistic values of w/w_c in between. From the numerical results, the empirical correction factor

$$1 + \frac{2.2}{(w/w_d)^2 + 3w_d/w}, \tag{5.7}$$

can be deduced for Equation (5.6), which takes values in the range between 1 and 1.56. As seen from Figure 5.9, very good agreement is obtained between the numerical results and the corrected analytical prediction.

As the correction factor approaches unity for $w/w_d \to 0$ and for $w/w_d \to \infty$, the corrected formula features the same small and large island limits as the original formula by Fitzpatrick. The maximum of Equation (5.6) with respect to w (when w_d is kept constant) is located at $w = w_d$. With the correction factor applied it moves slightly to $w = 1.056 w_d$. With respect to w_d (while w is kept constant), the corrected formula features a maximum at $w_d = 0.461 w$ as seen in Figure 5.9, that is absent in Equation (5.6).

In summary, the contribution of the bootstrap current perturbation to the island drive is underestimated significantly by Fitzpatrick's predictions for realistic island parameters. The empirical correction factor given in Equation 5.7 allows to describe the numerical results accurately.

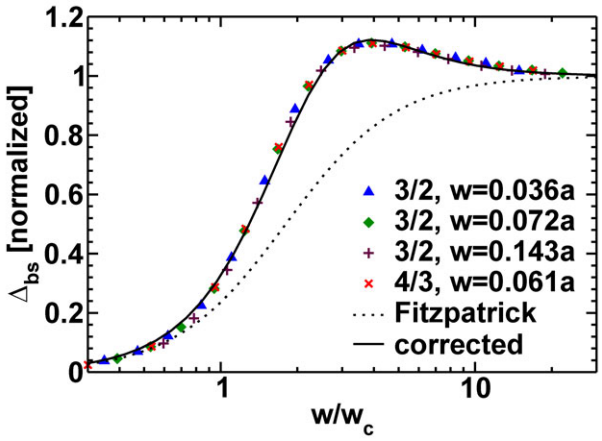

FIGURE 5.9. *The island drive Δ_{bs} caused by bootstrap current perturbations multiplied by the normalization factor $(w\sqrt{r_s}q_s')/(56.4T_s'q_s^3)$ is plotted versus w/w_c. Here, r_s denotes the value of r at the resonant surface, q_s the resonant safety factor, and T_s the resonant temperature value. Fitzpatrick's small and large island limits can be approved while Equation (5.6) underestimates the island drive significantly for realistic values of w/w_c. The discrepancy can be eliminated by the empirical correction factor given in Equation (5.7).*

Chapter 6.

Determination of the Heat Diffusion Anisotropy

The ratio between the heat diffusion coefficients parallel and perpendicular to the magnetic field lines, $\chi_{||}/\chi_{\perp}$, influences the flattening of the temperature profile inside magnetic islands and the driving term of neoclassical tearing modes. The value of this anisotropy is, however, not easily accessible experimentally. In this Chapter, a method is presented to determine it from a systematic comparison of temperature measurements at magnetic islands with numerical heat diffusion simulations. The application of the method is demonstrated for a $^2/_1$ magnetic island in the TEXTOR tokamak where a heat diffusion anisotropy of 10^8 is observed. This is lower by a factor of 40 than predicted by Spitzer and Härm [Spitzer53] and a strong indication that the heat flux limit determines the flattening of the electron temperature across magnetic islands.

Contents

6.1. Introduction

The reduced pressure gradient inside magnetic islands caused by the temperature flattening perturbs the bootstrap current and gives rise to neoclassical tearing modes (NTMs). The am-

plitude of the NTM driving term depends on w and w_c as discussed in Sections 2.6 and 5.5. Despite its important role for the dynamics of NTMs, the heat diffusion anisotropy cannot be determined directly in experiments.

In the following, experimental measurements of the temperature distribution around a magnetic island are systematically compared to numerical heat diffusion simulations in toroidal geometry. A technique is presented to determine the experimental heat diffusion anisotropy and the magnetic island size from this comparison. The application of the method is demonstrated for a $^2/_1$ magnetic island triggered by the dynamic ergodic divertor (DED) coil set in the TEXTOR tokamak. The electron temperature around the island, measured by ECE-Imaging, is compared to the numerical simulation results.

6.2. TEXTOR Experiments

Discharge number 99175 of the TEXTOR tokamak, which is characterized by a magnetic field strength of 2.25 T and a plasma current of about 300 kA, is studied. At the time considered (around $t = 1.6$ s), the plasma is heated by roughly 250 kW of Ohmic (OH) heating and about 300 kW of neutral beam injection (NBI) heating. The volume-averaged value of the normalized plasma pressure, β_N, takes a value of about 0.3. An overview over the most important plasma parameters is given in Figure 6.1.

6.2.1. Magnetic Perturbation Profiles

TEXTOR is equipped with a set of 16 helical perturbation field coils of the dynamic ergodic divertor ($\rightarrow$ Section 3.4.1). The principal component of the perturbation field that can be produced by these coils may be varied between $^3/_1$, $^6/_2$, and $^{12}/_4$ operation. In the considered case, the $^3/_1$ configuration is used with a 1 kHz AC current which raises a magnetic perturbation that rotates around the torus. The amplitude of the coil currents is ramped up from 0 kA to 1.9 kA between $t \approx 1.22$ s and 1.74 s. The magnetic perturbation has a strong $^2/_1$ sideband that creates a rotating $^2/_1$ magnetic island. As the DED coil currents only modify the boundary condition for the perturbed poloidal flux, $\tilde{\Psi}$, "DED-islands" are not different from "usual" magnetic islands in most respects.

The considered island starts to grow at about $t = 1.55$ s and locks to the external perturbation field at $t = 1.58$ s. The comparison will be performed during the island growth phase after the mode has locked. The radial profiles of the $^2/_1$ magnetic perturbation required for the calculations are derived from nonlinear cylindrical two-fluid MHD simulations. These are performed for typical TEXTOR parameters analogous to Reference [Yu09] and do not rely on the so-called vacuum assumption but include the full plasma interaction with the external magnetic perturbation. The obtained profiles are depicted in Figure 6.2 for two different perturbation amplitudes that lead to different island sizes. Only the $^2/_1$ magnetic perturbation excited by the DED coils is taken into account in the simulations. By performing vacuum

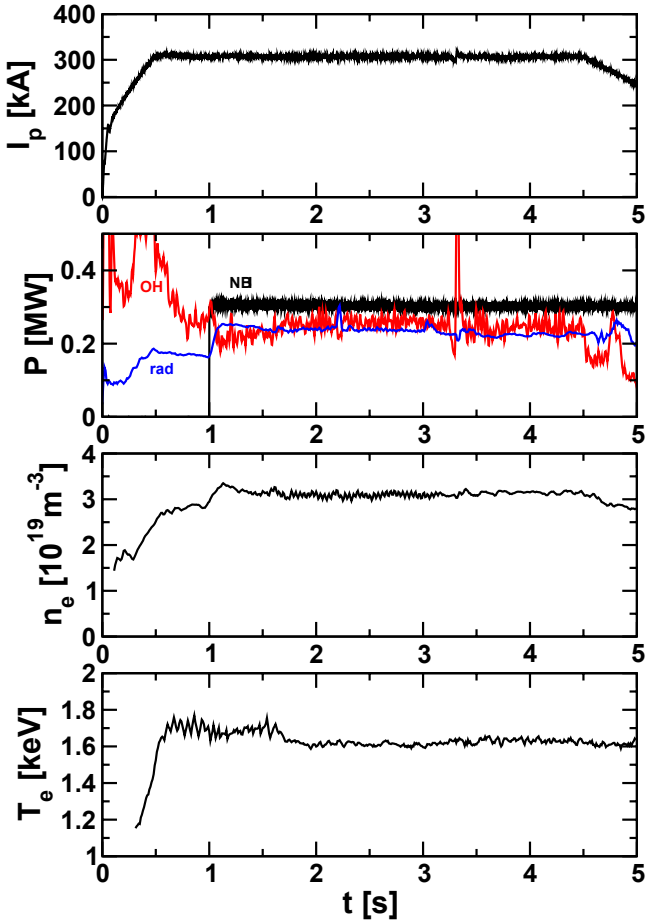

FIGURE 6.1. *The most important plasma parameters of TEXTOR discharge number 99175 are shown. From top to bottom, time-traces of the total plasma current, the heat source (Ohmic and NBI powers) and drain powers (radiated power), the core electron density, and the core electron temperature are given.*

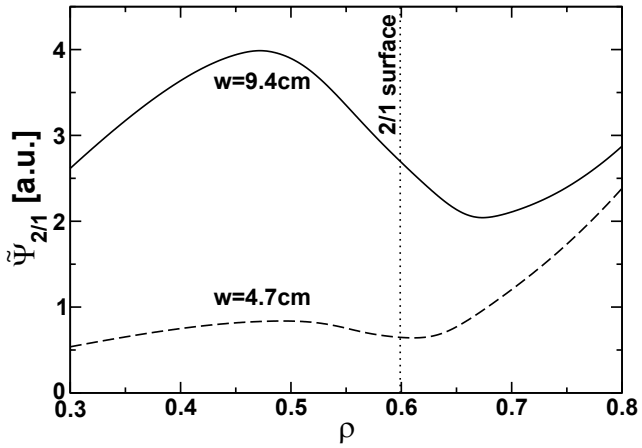

FIGURE 6.2. *Radial profiles of the $2/1$ magnetic perturbation are shown for two different perturbation amplitudes.*

magnetic field calculations, it has been checked that the full DED spectrum does not lead to a significant stochastisation at the island separatrix in the considered case at the considered perturbation amplitudes such that this assumption can not affect the obtained results for the heat diffusion anisotropy. Stochastisation due to the poloidal mode coupling, in fact, starts to arise already at perturbation amplitudes where the effect of the full DED spectrum is still rather weak.

6.2.2. Temperature Measurements

The electron temperature around the island is measured by TEXTOR's ECE-Imaging diagnostic that consists of an array of 8 radial times 16 vertical channels, which are located around the outer mid-plane for this shot (→ Section 3.5). Thermal noise intrinsic to any ECE measurement is suppressed by applying singular value decomposition (SVD) to the measured data array and keeping the 10 most significant eigenvector pairs. Incoherent data can be removed this way, allowing to resolve temperature fluctuations of small scales and amplitudes. SVD ensures that the statistics of all 128 channels contribute to the noise suppression although only some of the channels are actually used for the comparison.

The average electron temperature within a volume of roughly 1 cm^3 is measured by each ECE-Imaging channel. Assuming rigid body rotation, the time-trace of each channel provides data corresponding to a toroidal temperature profile at a different radial position in the vicinity of the $2/1$ resonant surface. From the channels that are located at the vertical position $Z = 0$, six were selected that are situated sufficiently close to the $2/1$ resonant surface to be relevant for the comparison. The channels, which will be referred to as $E_1 \ldots E_6$ in the following, are located between $R = 2.05$ m and 2.10 m. The measurements determine the temperature dis-

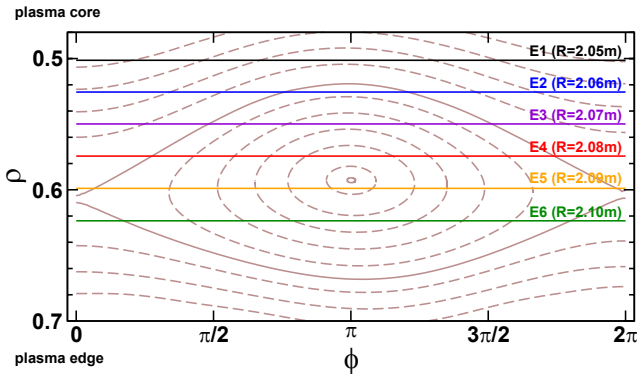

FIGURE 6.3. *For the reconstructed magnetic field topology at $t = 1.598$ s with an 8 cm wide $^2/_1$ island, a Poincaré plot that displays the magnetic flux surfaces is shown together with the lines along which the temperature is measured by the six ECE-Imaging channels $E_1 \ldots E_6$.*

tribution at the magnetic island on the low-field side of the plasma. For an island width of 8 cm, the position of the channels relative to the island is illustrated in Figure 6.3. The spatial resolutions of the ECE-Imaging measurement in radial and vertical directions are limited by the distance of the individual ECE-Imaging channels and by the size of the volume over which each channel "averages" the temperature. Both length scales are about one centimeter. The measurement was carried out with a sample frequency of 200 kHz and down-sampled to 100 kHz. This results in about 100 data points per mode transit around the torus which corresponds to a toroidal resolution of about 11 cm.

The ECE-Imaging signals are first cross-calibrated against the 1D ECE diagnostic. Successively, a careful relative calibration between the channels is performed that is determined using the measurements at a large magnetic island, where the temperature inside the island is known, e.g., from the time-traces of the ECE-Imaging signals themselves, to be largely flattened. The calibration is kept fixed for all cases considered. The experimental data is cut into time-fragments that correspond to one mode-transit around the torus, each (X-point to X-point of the island)[1]. These segments will be compared to numerical simulations later on.

6.3. Physics Model

The island evolution is slow enough such that the temperature distribution can be assumed to follow changes of the magnetic topology instantaneously. The electron heat transport is

[1] For cutting the signals into segments corresponding to single mode-transits, an adequate channel is selected and smoothed by applying running averages. The range between two adjacent maxima of the smoothed signal then corresponds to a single mode-transit.

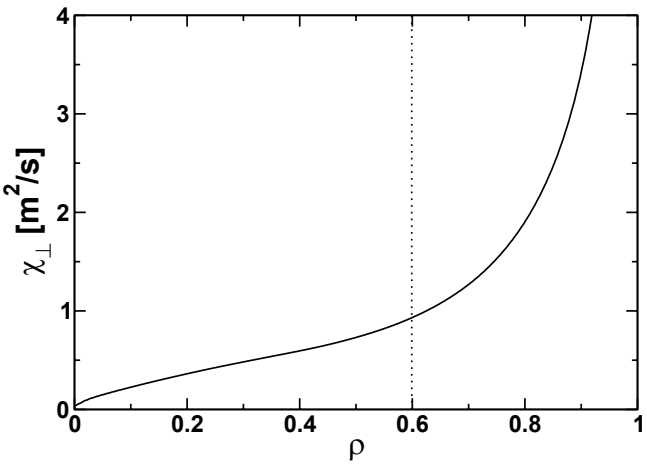

FIGURE 6.4. *The profile of the unperturbed cross-field heat diffusion coefficient, $\chi_{\perp,e}$, is given. It is determined by a numerical simulation from the unperturbed temperature profile prior to the mode onset and the heat deposition profile.*

therefore modeled by the steady-state anisotropic heat diffusion equation,

$$\nabla \cdot \mathbf{q}_e = P_e, \quad \text{where} \quad \mathbf{q}_e = -n_e \left[\chi_{||,e} \nabla_{||} T_e + \chi_{\perp,e} \nabla_\perp T_e \right] \tag{6.1}$$

is the electron heat flux density, n_e denotes the electron particle density, T_e the electron temperature, P_e the electron energy source (and sink) term, $\nabla_{||} T_e = \hat{\mathbf{b}}(\hat{\mathbf{b}} \cdot \nabla T_e)$ the temperature gradient parallel to the magnetic field lines, $\nabla_\perp T_e = \nabla T_e - \nabla_{||} T_e$ the cross-field temperature gradient, and $\hat{\mathbf{b}} = \mathbf{B}/B$ the magnetic field direction vector.

The local heating power density at the magnetic island does not play an important role for the investigations, as the temperature distribution is not peaked significantly around the O-point of the island. It is assumed that the electrons are effectively heated by half of the sum of Ohmic and NBI heating powers. Radiative losses that probably originate mostly from carbon ions at the plasma boundary are neglected[2]. The profile of the unperturbed cross-field heat diffusion coefficient, $\chi_{\perp,e}$, can be determined from the heating power deposition profile and the temperature profile measured prior to the onset of the magnetic island. The resulting profile is plotted in Figure 6.4 and is used for the successive simulations. At the $^2/_1$ resonant surface, $\chi_{\perp,e}$ takes a value of about $0.9\,\mathrm{m}^2/\mathrm{s}$. It is assumed that the island does not alter the $\chi_{\perp,e}$

[2]Moderate inaccuracies in the heating power density can not affect the obtained value of the heat diffusion anisotropy but only the profile of the cross-field diffusivity, which leads, in turn, only to a marginal error in the calculation of the analytic anisotropy predictions to which the results are compared. This error may be neglected as it is much smaller than the uncertainty of the heat diffusion anisotropy obtained from the comparison between measured and simulated temperature profiles.

profile significantly. Inside magnetic islands, the perpendicular heat diffusion coefficient may, however, be different from its value outside the island [Inagaki04, Spakman08]. The value of $\chi_{\perp,e}$ inside the island influences how strongly the temperature peaks around the O-point due to local heat sources. In the considered TEXTOR discharge, the small amount of local Ohmic and NBI heating inside the magnetic island leads only to a very moderate peaking. Comparing it to the simulations indicates a cross-field diffusivity inside the island that is of a similar order as outside the island. However, the uncertainties regarding the low local heating power density does not allow to investigate this issue in detail. Examinations with electron cyclotron resonance heating into the magnetic island are planned to be considered for this purpose in the future. The computations are performed in toroidal geometry with the numerical scheme described in Section 4.2. The coordinate system chosen is aligned to the $^2/_1$ magnetic island to reduce the necessary toroidal resolution ($\iota_c = {}^1/_2$, $\rightarrow$ Section 4.3).

6.4. Comparison of Simulations and Measurements

The method is now applied to TEXTOR discharge number 99175. Equipped with profiles for heating power density, electron density, the $^2/_1$ magnetic perturbation, and the equilibrium cross-field heat diffusivity, Equation (6.1) is solved for various values of the island width,

$$w = 4.0\,\text{cm},\ 4.5\,\text{cm},\ 5.0\,\text{cm},\ \ldots,\ 11.0\,\text{cm}$$

and heat diffusion anisotropy,

$$\chi_{||}/\chi_{\perp} = 1\times10^7,\ 1.5\times10^7,\ 2\times10^7,\ 3\times10^7,\ 5\times10^7,\ 7\times10^7,\ 1\times10^8,\ \ldots,\ 1\times10^9.$$

The simulations were carried out with 91 radial, 129 poloidal and 17 toroidal grid points. The radial range between $\rho = 0.35$ and $\rho = 0.8$ was resolved. For each mode-transit, the numerical simulation is selected that reproduces the experimental temperature measurements best as indicated by the smallest quadratic deviations[3].

"Numerical temperature signals", separated by $\Delta R = 0.25$cm, are determined as toroidal profiles ($\phi = 0\ldots2\pi$) at the outer mid-plane ($Z = 0$). As the distance between the ECE-Imaging channels is approximately 1 cm, every fourth numerical signal has to be compared to an experimental channel. An integer number, i, is introduced, such that the numerical signals $N_i, N_{i+4}, \ldots, N_{i+20}$ are matched to the experimental channels $E_1, E_2, \ldots, E_6$. The most reasonable value for i is selected automatically in every matching procedure to account for a possible slight variation of the safety factor profile due to the growing magnetic island. For the considered discharge, i remains virtually constant which corresponds to a fixed mapping between experimental channels and numerical signals and indicates that the position of the $^2/_1$ resonant surface does not vary by more than 0.5 cm.

[3]The matching algorithm is described in detail in Appendix B.4.

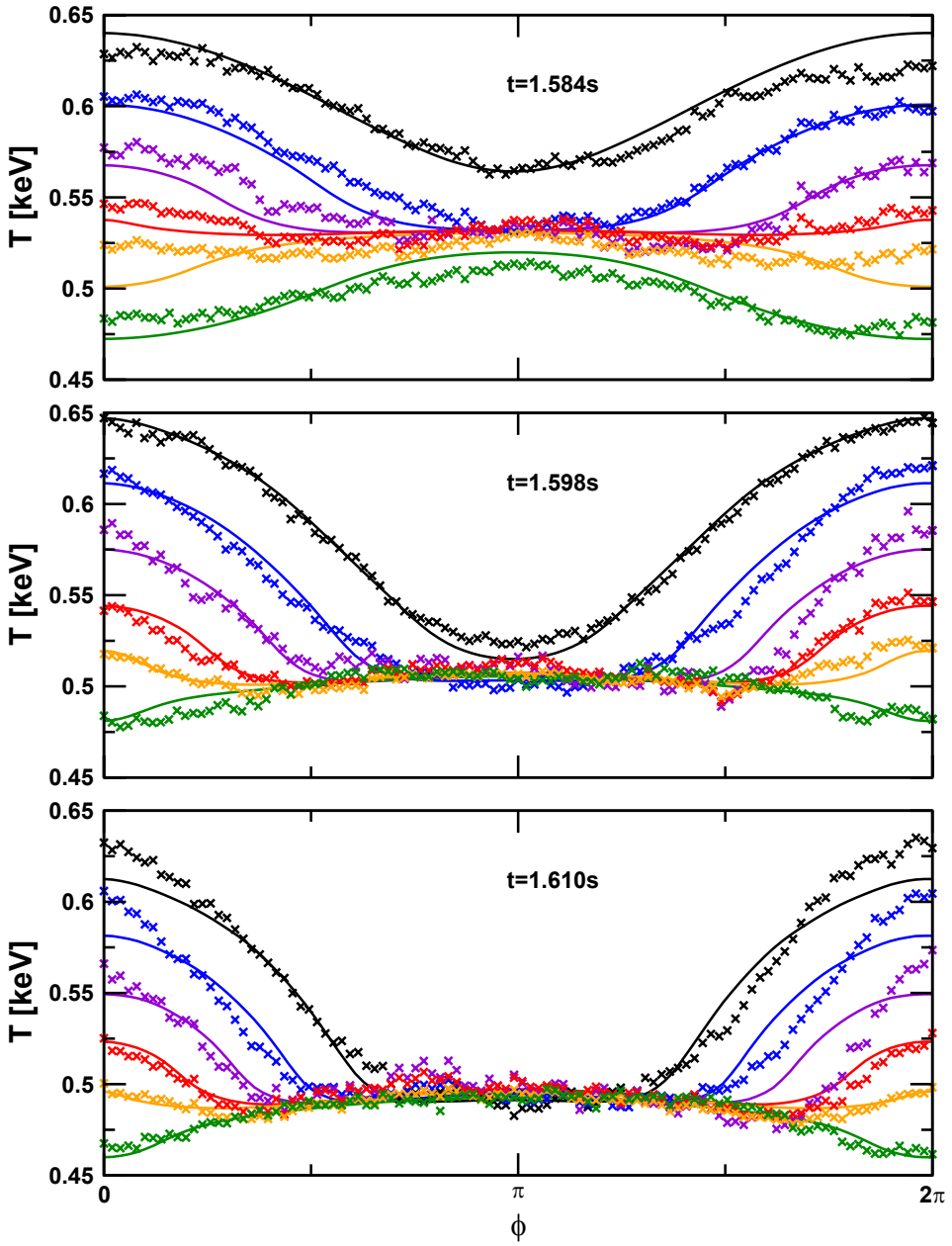

FIGURE 6.5. *Comparison of experimental temperature measurements ("×") and numerical simulation results (solid lines) for three different times. The island X-point is located at $\phi = 0$ and $\phi = 2\pi$ while the O-point is positioned at $\phi = \pi$.*

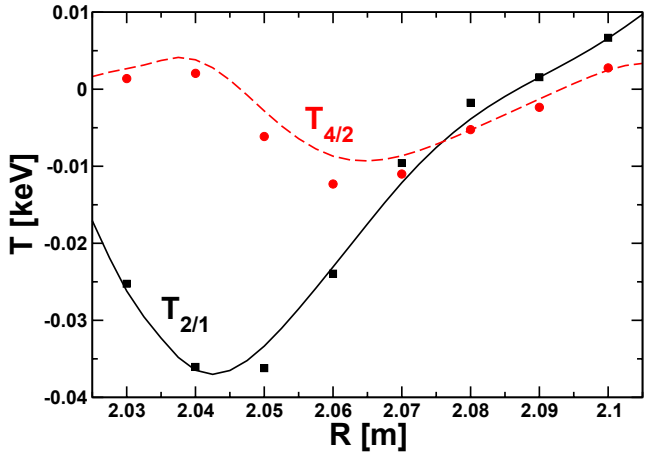

FIGURE 6.6. *Comparison of the first two experimental (circles) and numerical (solid lines) temperature harmonics for the mode transit at* $t = 1.610$ s.

6.4.1. Matching of measured and calculated temperature profiles

For $t = 1.598$ s, Figure 6.3 shows a Poincaré plot of the reconstructed magnetic field structure together with the lines along which the temperature is measured by the six considered ECE-Imaging channels. Very good agreement between numerical simulations and experimental data is obtained in the time-interval between $t = 1.584$ s and 1.610 s. For three representative time-points in this interval, the experimental and numerical data sets are compared in Figure 6.5. The deviation seen around the X-point at $t = 1.584$ s is probably caused by two factors. Firstly, the distance between the ECE-Imaging channels is not exactly 1 cm as assumed for the comparison, but varies between 0.9 cm and 1.2 cm. Secondly, the calculations are performed in steps of $\Delta w = 0.5$ cm for the magnetic island size, only, which are quite large at small magnetic islands. The asymmetry observed in some of the experimental measurements, especially at $t = 1.610$ s, that causes some deviations in the comparison might result from a shearing force opposed onto the island by the plasma.

For $t = 1.610$ s, Figure 6.6 compares the first two harmonics of the experimental temperature measurements to these determined from numerical data. Good agreement is observed. This comparison has the advantage that the relative calibration between the experimental ECE channels does not enter into the harmonics. For the determination of the heat diffusion anisotropy from the temperature harmonics, one would need to consider more temperature harmonics. The radial structure of the higher harmonics can, however, not be resolved by the given distance between the ECE-Imaging channels.

The time-trace of the matching error, i.e., the quadratic difference between the measured and calculated temperature profiles, is plotted in Figure 6.7. For the determination of $\chi_{||}/\chi_{\perp}$, the time-interval between $t = 1.584$ s and 1.610 s is used where the numerical simulations

are able to reproduce the experimental measurements very accurately. The strongly increased error prior to this time-interval originates from distinct irregularities in the ECE-Imaging signals. These probably arise as the island is not yet locked completely to the external perturbation field and fluctuates between locking and unlocking. After $t = 1.61$ s, the island has become larger than 20 percent of the minor radius. Higher harmonic magnetic perturbations ($1/1$, $3/1$, $3/2$, $5/2$, ...), that are excited by the poloidal mode coupling, arise in the simulations at this point and start to cause stochastisation of the island separatrix. The neglect of all modes of the DED-spectrum except the $2/1$ component has only a very small influence onto the stochastisation that does not play a role here.

It is, however, not clear if the stochastisation is also present in the experiment. The temporal resolution of CXRS measurements[4] is not sufficient to tell if the plasma is still rotating differentially at the time of interest right after the $2/1$ mode locking or if the differential rotation has already vanished. In case of differential rotation, the higher harmonics would not be coupled and the stochastisation removed by shielding currents.

6.4.2. Sensitivity of the simulated temperature signals on w and $\chi_{||}/\chi_{\perp}$

In the following, the sensitivity of the simulated temperature signals on variations of the island width and the heat diffusion anisotropy will be demonstrated. This allows to give an estimate for the accuracy of the values determined by the matching procedure between experimental and numerical data. For this purpose, results for $t = 1.598$ s will be analyzed in detail, where an island width of 8.0 cm and a heat diffusion anisotropy of $\chi_{||}/\chi_{\perp} = 1 \cdot 10^8$ are detected.

As seen from Figure 6.8a, the numerical temperature signals close to the resonant surface (numbered (4), (5), and (6) in Figure 6.8a) remain virtually unchanged, when the island width is varied between 7 cm and 9 cm. In contrast, temperature signals far from the resonant surface (e.g., number (1) in Figure 6.8a) are affected very strongly. The measured temperature distribution is not reproduced reasonably by simulations with island widths of 7 respectively 9 cm, but very well by $w = 8$ cm. The detected island widths are therefore reliable to ± 0.5 cm.

As expected, the heat diffusion anisotropy affects the temperature signals far from the resonant surface only slightly except for some offset shift. However, the signals close to the resonant surface are changed quite significantly in the X-point region (around $\phi = 0$), as seen from Figure 6.8b. Clearly, the computations performed for $\chi_{||}/\chi_{\perp} = 2 \cdot 10^7$ and $\chi_{||}/\chi_{\perp} = 5 \cdot 10^8$ reproduce the measured temperature distribution much worse than the simulation with $\chi_{||}/\chi_{\perp} = 1 \cdot 10^8$. The detected values of the heat diffusion anisotropy for each mode-transit around the torus are therefore reliable within a factor smaller than 5.

[4] Charge exchange recombination spectroscopy (CXRS) takes advantage of charge exchange events that occur between fast neutrals from NBI heating and C^{6+} ions in the plasma (different ion species are also possible). Excited C^{5+} ions are produced that emit characteristic radiation when recombining into the C^{5+} ground state. By measuring the Doppler-shift of this line, the toroidal ion rotation velocity can be determined at a typical time-resolution of 50 ms.

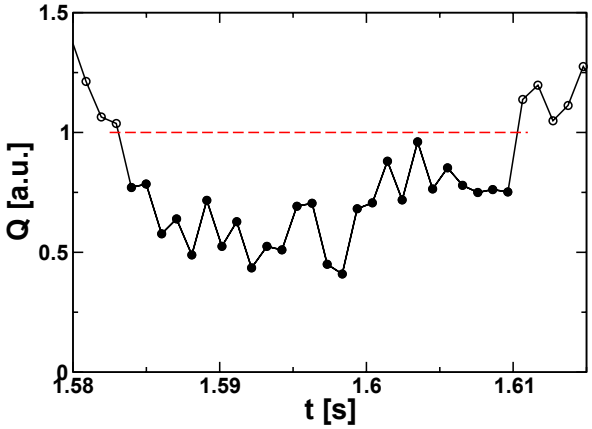

FIGURE 6.7. *The quadratic difference between measurements and simulations are given for each mode-transit. This allows to identify the time-window where the experimental data can be reproduced well by the numerical simulations. For the determination of* $\chi_{||}/\chi_{\perp}$, $t = 1.584 \ldots 1.610$ s *is considered.*

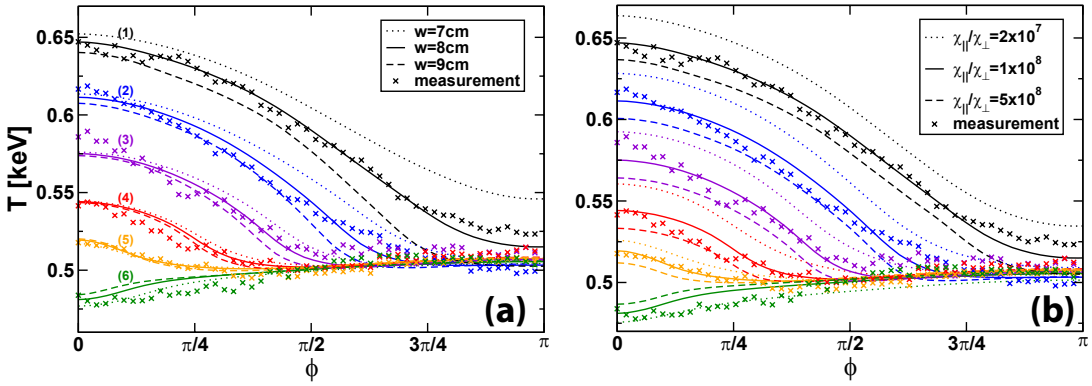

FIGURE 6.8. *In Part* ***(a)****, the sensitivity of the temperature signals on the island width is shown for* $t = 1.598$ s *with* $\chi_{||}/\chi_{\perp} = 1 \cdot 10^8$. *Numerical temperature signals for* $w = 7$ cm *(dotted lines),* 8 cm *(solid lines), and* 9 cm *(dashed lines) are compared. Only the temperature signals far from the resonant surface are affected significantly by small changes of the island width. A width of about* 8 cm *is required to reproduce the measured temperature distribution. In Part* ***(b)****, the dependence of the temperature signals on the heat diffusion anisotropy is shown. Temperature signals for* $\chi_{||}/\chi_{\perp} = 2 \cdot 10^7$ *(dotted lines),* $1 \cdot 10^8$ *(solid lines), and* $5 \cdot 10^8$ *(dashed lines) are compared. The value of* $\chi_{||}/\chi_{\perp}$ *mostly affects the temperature distribution around the X-point (green, orange and red curves around* $\phi = 0$*). An anisotropy around* $1 \cdot 10^8$ *is required to reproduce the measurements.*

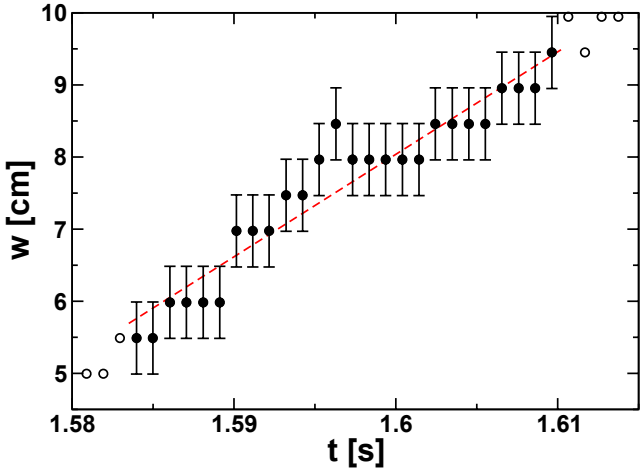

FIGURE 6.9. *The evolution of the island size is shown. During the considered time-interval, the island width grows from about* 5.5 cm *to* 9.5 cm.

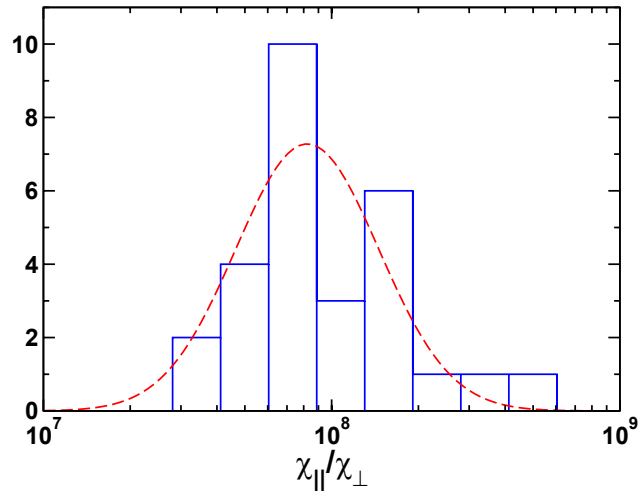

FIGURE 6.10. *The obtained values for the heat diffusion anisotropy roughly form a Gaussian distribution (dashed line). This allows to estimate the statistical uncertainty of the obtained values.*

6.4.3. Results

The procedure explained in the previous Section is now applied to measurements of many mode transits around the torus. Thus, time-traces of the island width and the heat diffusion anisotropy are obtained. From Figure 6.9, the magnetic island width can be seen to increase from about (5.5 ± 0.5) cm to (9.5 ± 0.5) cm within the considered interval of 26 ms corresponding to a growth rate of about (1.5 ± 0.3) m/s. The heat diffusion anisotropy fluctuates around a value of 10^8 which corresponds to $w_c \approx 2$ cm. Thus, w/w_c rises roughly from 3 to 5.

The distribution of the obtained values for $\chi_{||}/\chi_{\perp}$ is analyzed in Figure 6.10. It is seen to agree quite well with a Gaussian distribution which allows to approximate the statistical uncertainty. The value $\chi_{||}/\chi_{\perp} \approx 8 \cdot 10^7$ is obtained with an uncertainty factor of about 2. Due to the large number of "measurements" of the heat diffusion anisotropy, the uncertainty is significantly smaller than that of one single mode-transit which was estimated in Section 6.4.2. The assumed systematical error of 30 percent in the value of $dq/d\rho$ at the $2/1$ resonant surface results in an additional factor of 2. Altogether, the observed heat diffusion anisotropy at the considered $2/1$ magnetic island is

$$\chi_{||}/\chi_{\perp} = 10^{7.9 \pm 0.5}. \tag{6.2}$$

6.4.4. Discussion

In a typical tokamak plasma, the temperature gets constant on flux surfaces irrespective of the exact value of the heat diffusion anisotropy except for those surfaces that belong to the heat conduction layer of a magnetic island which is located at the island's separatrix [Fitzpatrick95]. Only in this region, the temperature distribution is sensitive to the heat diffusion anisotropy. It is consequently the effective heat diffusion anisotropy in the heat conduction layer that is determined by the comparison. Spitzer and Härm derived the expression

$$\chi_{||}^{SH} = 3.16 \cdot v_{th,e} \cdot \lambda_e \approx 3.6 \cdot 10^{29} \frac{T_e[\mathrm{keV}]^{5/2}}{n_e[\mathrm{m}^{-3}]} \mathrm{m}^2/\mathrm{s} \tag{6.3}$$

for the parallel heat diffusivity assuming free-streaming electrons, where $v_{th,e}$ denotes the electron thermal velocity, λ_e the collisional electron mean free path, T_e the electron temperature given in keV, and n_e the electron density given in m^{-3} [Spitzer53, Braginskii65]. According to the Spitzer-Härm formula, a heat diffusion anisotropy of $10^{9.6 \pm 0.3}$ would be expected at the considered $2/1$ island in TEXTOR. In the calculation of this prediction, the cross-field diffusivity of Figure 6.4 enters[5]. The temperature at the magnetic island changes by 8 percent

[5] This assumption seems to be reasonable as the cross-field diffusivity is relevant only in the heat conduction layer around the island separatrix and not further inside the island. A deviation of the cross-field diffusivity from the background plasma would not affect the value obtained for the heat diffusion, but only the calculation of the Spitzer-Härm prediction. A reduced cross field diffusivity would lead to an even higher anisotropy prediction such that the qualitative conclusion would not be altered.

in the considered time-interval which corresponds to a change of the anisotropy prediction of about 20 percent which is negligible. Inaccuracies in the perpendicular heat diffusion coefficient caused by uncertainties in the electron heating power profile may affect the calculated anisotropy prediction only slightly and can be neglected as well.

The predicted heat diffusion anisotropy is by 1.7 ± 0.6 orders of magnitude larger than what is observed in the comparison which is an indication for the heat flux limit [Malone75]. It predicts the same heat diffusion anisotropy as Spitzer and Härm in a very thin layer ($\lesssim 1$ mm) around resonant surfaces and the separatrices of magnetic islands, but values reduced by 1 or 2 orders of magnitude apart from these. In the considered discharge, the width of the heat conduction layer around the $^2/_1$ island is roughly between 0.5 cm and 2 cm according to the analytical estimate given in Reference [Fitzpatrick95]. Thus, the heat diffusion anisotropy is predicted to be much lower than the Spitzer-Härm level over most of the heat conduction layer according to heat flux limit theory. Qualitatively, this prediction agrees very well with the observation that the effective heat diffusion anisotropy in the heat conduction layer is much lower than the Spitzer-Härm level. An indication for the heat flux limit has recently also been found using an analytical approach in Reference [Tokar07].

6.5. Summary

A method for the determination of the magnetic island size and the heat conduction anisotropy in the experiment by comparing results of numerical heat diffusion computations to experimental temperature measurements has been developed. An algorithm automatically detects these numerical temperature profiles across a magnetic island that reproduce the measurements for every mode transit around the torus best. As the heat diffusion anisotropy is a key parameter for the understanding of NTMs but cannot be measured directly in the experiment, the demonstrated method might help to improve the understanding of island dynamics.

The scheme has been applied to a $^2/_1$ magnetic island in the TEXTOR tokamak that grows from about $w = 5.5$ cm to 9.5 cm at a growth rate of 1.5 m/s. The ratio between the island width, w, and the scale island width for temperature flattening, w_c, changes, accordingly, from 3 to 5. A heat diffusion anisotropy of 10^8 is observed with an uncertainty factor of 3. This is lower than the Spitzer-Härm prediction by a factor of roughly 40 and strongly supports the heat flux limit theories. In the following Chapter, the method is also applied to a neoclassical tearing mode in ASDEX Upgrade.

Chapter 7.

NTMs in ASDEX Upgrade

In this Chapter, a similar comparison of heat transport simulations to experimental electron temperature profiles is performed as in Chapter 6. Here, however, a neoclassical tearing mode in ASDEX Upgrade is considered. Analogously to the previous Chapter, the size of the island and the heat diffusion anisotropy at the island are determined from the comparison of experimental and numerical temperature signals.

Contents

7.1. Experimental Situation

ASDEX Upgrade discharge number 25174 is considered, where a rotating $2/1$ neoclassical tearing mode is visible in the Mirnov coil signals between $t = 2.005$ s and 2.203 s. The mode also exists before and after this time-period, but there it is locked to the vacuum vessel meaning that it does not rotate relative to the lab frame[1]. Thus, it is neither visible in the Mirnov

[1] Mode locking is essentially caused by two effects: By currents induced in the conducting vacuum vessel due to mode rotation and by error fields due to the misalignment of the poloidal field coils.

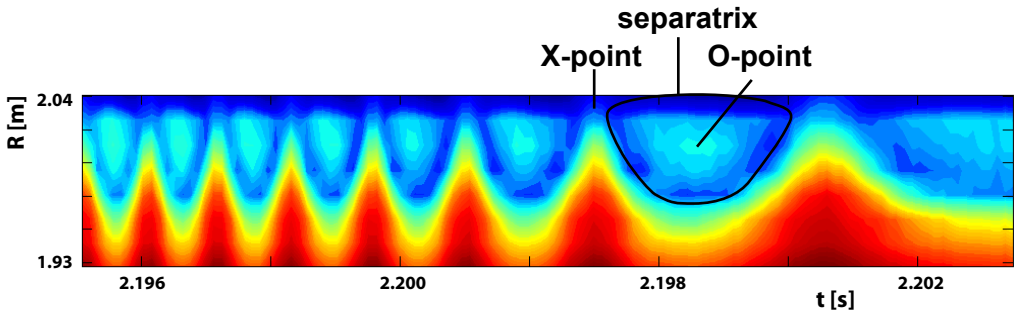

FIGURE 7.1. *Electron temperature at an NTM in ASDEX Upgrade [Classen09].*

signals, nor can the toroidal structure of the mode be detected by the ECE-Imaging diagnostic which has been installed very recently in ASDEX Upgrade and is used for this comparison. A contour plot of the electron temperature from ECE-Imaging is shown in Figure 7.1 right before the mode locks such that the mode-frequency continuously decreases.

In the relevant time-period, the electron temperature at the island is determined by 1D ECE measurements to be about $T_e = (1.1 \pm 0.1)$ keV. The ECE-Imaging signals are cross-calibrated with 1D ECE. The electron density[2] is approximately $n_e = (4 \pm 1) \cdot 10^{19}$ /m^3. Assuming Spitzer-Härm diffusivity according to Equation (6.3) and with $\chi_\perp = (1 \pm 0.5)$ m/s, the heat diffusion anisotropy is predicted to be

$$\chi_{||}^{SH}/\chi_\perp = 10^{10.0 \pm 0.5}. \tag{7.1}$$

This is slightly higher than the value predicted for the island in TEXTOR which was investigated in the previous Chapter.

Figure 7.2 depicts the position of the considered NTM in ASDEX Upgrade along with the positions of the ECE-Imaging channels. The comparison is carried out for the time period between $t = 2.037$ s and 2.142 s, during which 540 mode-transits around the torus take place. In this period, the mode frequency rises from about 4 kHz to 5.5 kHz while the ECE-Imaging data is sampled at 100 kHz. In addition to the application of singular value decomposition analogously to the previous Chapter, the slower island evolution also allows to perform averages of several mode-transits for further noise suppression. Therefore, by averaging ten mode-transits at a time, 54 averaged mode-transits are determined and are eventually compared to numerical simulations. A sudden change of the mode structure at about 2.145 s, which might be related to the coupling to different MHD activity, does not allow to continue with the comparison beyond this time. Six ECE-Imaging channels located in the range between $R = 1.943$ m and 2.023 m and at $Z = 0.195$ m are selected for the comparison, which cover the whole radial extent of the magnetic island.

7.2. Comparison

Numerical simulations are performed covering the radial range between $\rho = 0.35$ and 0.9 as indicated by the blue dashed lines in Figure 7.2. Neumann boundary conditions are applied at the inner and Dirichlet boundary conditions at the outer edge of the computational regime. The simulations are able to reproduce the experimental data very accurately as shown for two representative samples in Figure 7.3. The virtually constant value of i ($\rightarrow$ Section 6.4 and Appendix B.4) indicates that the position of the resonant surface remains constant within an uncertainty of 0.3 cm during the considered time-period of about 105 ms.

[2] The density-profile is not known well in this discharge due to a minor disruption occurring at about 1.5 s that distracts the relevant diagnostics. This causes some uncertainties regarding the heating power deposition profile which does, however, only have a small impact on the results of the comparison as discussed in Section 6.3.

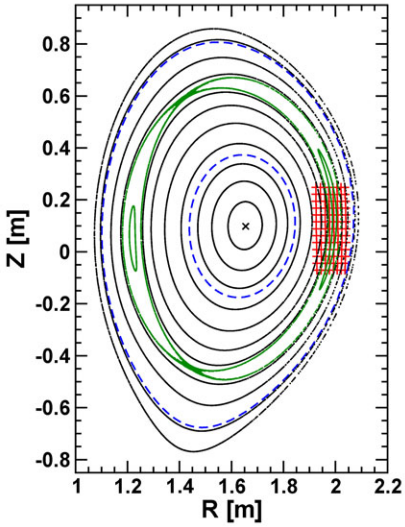

FIGURE 7.2. *The magnetic field structure of ASDEX Upgrade discharge 25174 at about* 2.1 s *with a* $2/1$ *NTM present in the plasma is shown. The positions of the ECE-Imaging channels is marked in red. The blue dashed lines indicate the radial domain that is resolved in the heat transport simulations.*

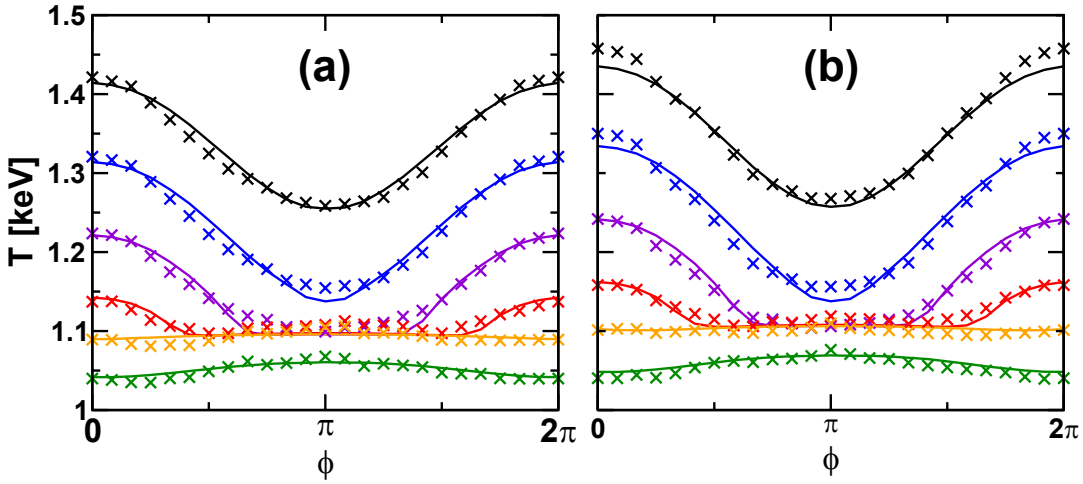

FIGURE 7.3. *Experimental measurements ("×") and numerical simulation results (solid lines) are compared for* ***(a)*** $t = (2.0595 - 2.0616)$ s *and* ***(b)*** $t = (2.1222 - 2.1240)$ s. *The simulations are able to reproduce the experimental measurements very accurately.*

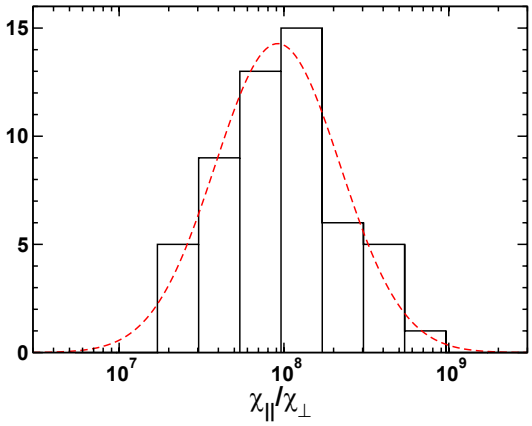

FIGURE 7.4. *A histogram of the distribution of the obtained values for the heat diffusion anisotropy is shown, which agrees very well with a Gaussian distribution peaked at a value of* $1 \cdot 10^8$.

The comparison of experimental and numerical temperature signals gives a value for the heat diffusion anisotropy, $\chi_{||}/\chi_{\perp}$, and for the island width, w, for each of the 54 averaged mode-transits. The island width is observed to increase slowly from about 7 cm to roughly 8 cm. The distribution of the values obtained for $\chi_{||}/\chi_{\perp}$ is shown in Figure 7.4. It agrees very well with a Gaussian distribution such that the heat diffusion anisotropy in the experiment is found to be

$$\chi_{||}/\chi_{\perp} = 10^{8.0 \pm 0.5} \tag{7.2}$$

in this case. The given error bar already includes the uncertainty in the safety factor profile. This value corresponds to a scale island width for temperature flattening of

$$w_c = (1.8 \pm 0.5)\ \text{cm} \tag{7.3}$$

and to

$$w/w_c = 4.2 \pm 1.2. \tag{7.4}$$

The observed heat diffusion anisotropy is by 2.0 ± 0.7 orders of magnitude lower than the prediction by Spitzer and Härm. Within the error bars, this agrees very well with the observations for the island in TEXTOR presented in the previous Chapter. It is planned to perform additional examinations for ASDEX Upgrade with different plasma parameters, where a significantly higher heat diffusion anisotropy can be expected at the island location.

Chapter 8.

Ergodic Layers

Overlapping magnetic islands lead to an ergodization of the magnetic field structure as discussed in Section 2.7. The degree of stochastization is commonly measured by the so-called Chirikov parameter, σ_{Ch}. For two adjacent islands, this parameter is defined as the average island width divided by the distance between the resonant surfaces. Ergodization occurs for $\sigma_{Ch} \gtrsim 1$. Field line trajectories in this case do not remain on flux surfaces as it is the case in equilibrium magnetic configurations or at magnetic islands but rather move stochastically through the volume of the ergodic layer.

The field lines in an ergodic field layer connect regions closer to the plasma core with ones further outwards which gives rise to a parallel contribution to the radial heat transport. Similar to magnetic islands, the parallel connection length is much longer than the linear distance across the ergodic layer. Therefore, a competition arises between parallel and perpendicular transport. The temperature (partially) flattens in the ergodic field layer when the parallel contribution becomes dominant.

In this Chapter, numerical simulation results for heat transport across ergodic field layers are shown and discussed. First, the basic properties are addressed in Section 8.1. Similarities and differences between ergodic heat transport and single island heat transport are highlighted. Then, a highly ergodic region with $\sigma_{Ch} \gg 1$ is considered in Section 8.2. The results are compared to analytical predictions. Successively, the possible connection between the rapid amplitude drop of neoclassical tearing modes in the frequently interrupted regime with magnetic field ergodization is discussed in Section 8.3. Finally, the effect of an ergodic plasma boundary, which is produced by resonant magnetic perturbation coils, onto the edge temperature profile is investigated in Section 8.4.

Contents

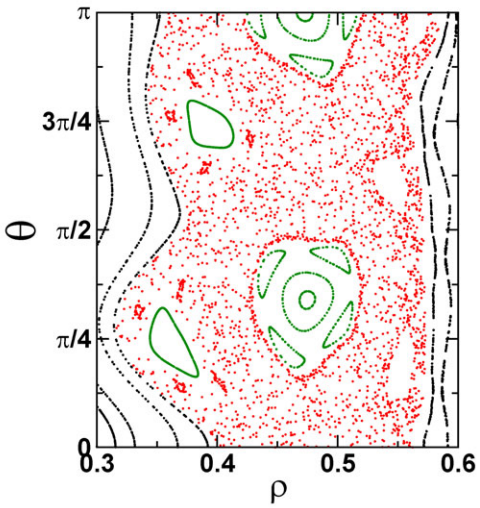

FIGURE 8.1. *A Poincaré plot of an ergodic layer with $\sigma_{Ch} = 1.6$ produced by overlapping $3/2$ and $4/3$ magnetic islands in ASDEX Upgrade geometry is shown. The Poincaré plot is equivalent to Figure 2.10 but shows the magnetic field structure in ρ-θ coordinates instead of cylindrical coordinates.*

8.1. Basic Heat Transport Properties

This Section investigates the basic properties of heat transport across ergodic layers in toroidal geometry. For this purpose, two overlapping $3/2$ and $4/3$ magnetic islands in ASDEX Upgrade geometry are considered. The widths of the islands are $w_{3/2} = 8.5$ cm respectively $w_{4/3} = 5.3$ cm. The resonant surfaces of the islands are located at $\rho_{3/2} = 0.492$ respectively $\rho_{4/3} = 0.419$ which corresponds to minor radii of $r_{3/2} = 0.300$ m respectively $r_{4/3} = 0.256$ m. Thus, the Chirikov parameter,

$$\sigma_{Ch} = \frac{w_{3/2} + w_{4/3}}{2 \cdot (r_{3/2} - r_{4/3})}, \tag{8.1}$$

takes a value of 1.6 which is larger than unity and thus indicates stochastisation. The magnetic configuration which results from the two overlapping magnetic islands is shown in the Poincaré plot of Figure 8.1. Embedded in the ergodic layer, some island remnants are visible where the island flux surfaces are still intact. At higher values of the σ_{Ch}, such remnants vanish as seen in the examinations of Section 8.2.

The scale island width for temperature flattening of the two islands, which is defined by

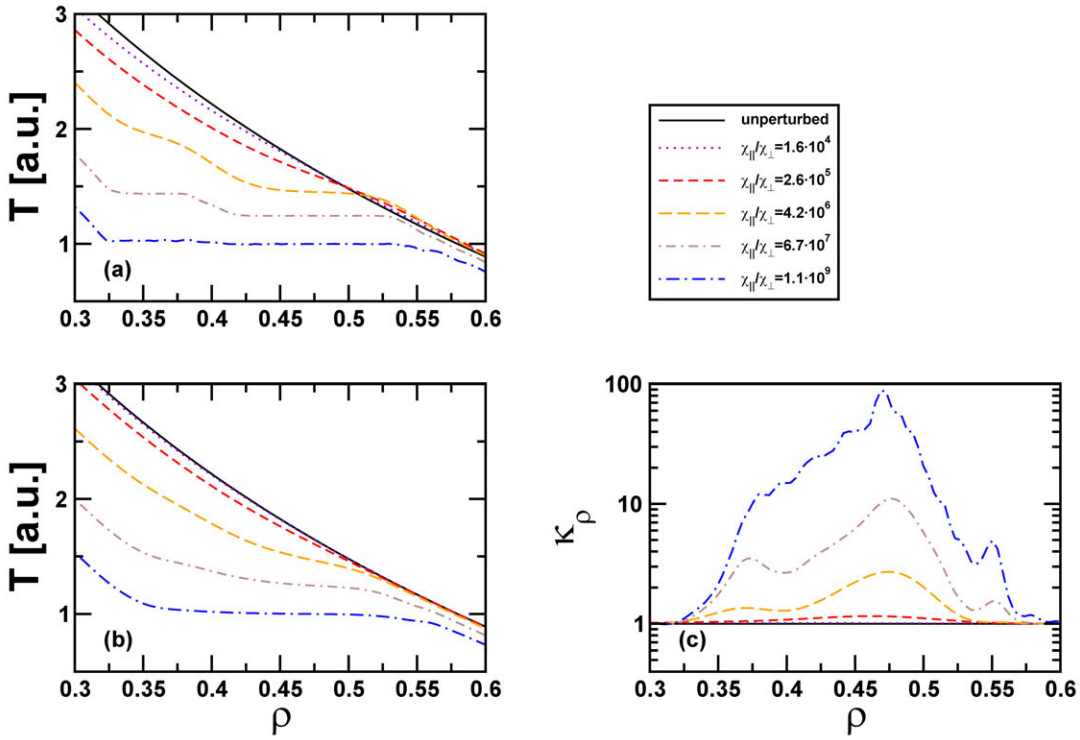

FIGURE 8.2. *Results for the heat transport across the ergodic layer of Figure 8.1 are shown.* ***(a)*** *The radial temperature distribution across the O-point of the 3/2 magnetic island is given for various different heat diffusion anisotropies. The temperature flattening occurs first in the individual island regions and extends to the whole ergodic layer for large values of $\chi_{||}/\chi_{\perp}$.* ***(b)*** *The radial profile of the poloidally and toroidally averaged temperature distribution is given.* ***(c)*** *The normalized effective radial heat diffusion coefficient is shown.*

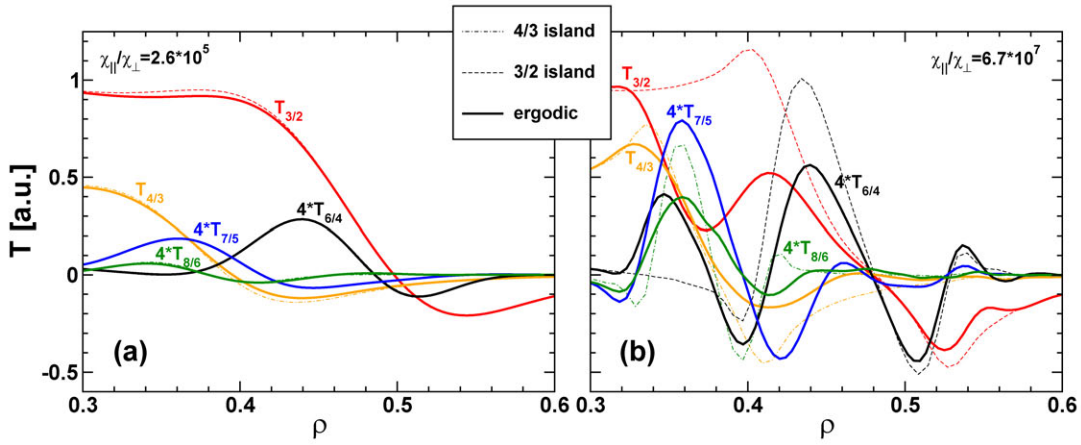

FIGURE 8.3. *The radial distribution of some temperature Fourier harmonics at the ergodic layer are compared to magnetic island results.* ***(a)*** *At a moderate heat diffusion anisotropy, the temperature harmonics at the ergodic layer and at single islands are very similar except for coupled modes like $T_{7/5}$ that are not excited in the single island cases.* ***(b)*** *At higher heat diffusion anisotropies, the temperature harmonics at the ergodic layer differ significantly from the single island cases.*

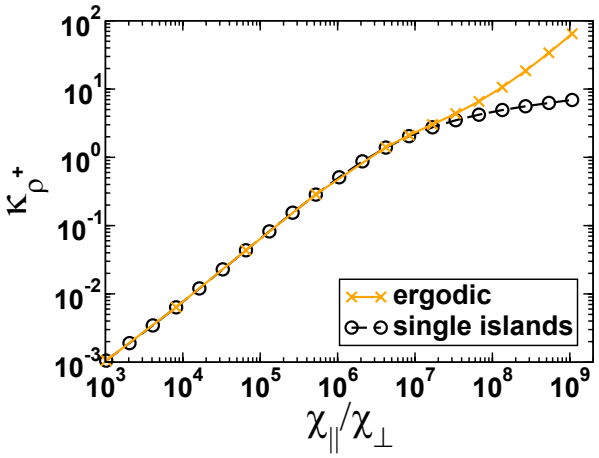

FIGURE 8.4. *The normalized increase, κ_ρ^+, of the effective radial heat diffusivity at the $q = 7/5$ surface is shown. Radial heat transport is strongly enhanced for large heat diffusion anisotropies compared to the sum of single island effects, while both are equal for small values of $\chi_{||}/\chi_\perp$.*

Equation (2.43), is given by

$$w_{c,3/2} = 1.74\ \mathrm{m} \cdot \left(\frac{\chi_{||}}{\chi_{\perp}}\right)^{-1/4} \quad \text{and} \quad w_{c,4/3} = 1.56\ \mathrm{m} \cdot \left(\frac{\chi_{||}}{\chi_{\perp}}\right)^{-1/4}, \tag{8.2}$$

such that

$$\left[\frac{w}{w_c}\right]_{3/2} = 0.047 \cdot \left(\frac{\chi_{||}}{\chi_{\perp}}\right)^{1/4} \quad \text{and} \quad \left[\frac{w}{w_c}\right]_{4/3} = 0.033 \cdot \left(\frac{\chi_{||}}{\chi_{\perp}}\right)^{1/4}. \tag{8.3}$$

The simulations for the heat transport across the ergodic layer produced by the overlapping $3/2$ and $4/3$ magnetic islands are carried out in a coordinate system that is aligned to the $7/5$ helicity ($\iota_c = 5/7$, $\rightarrow$ Section 4.3). The temperature distribution across the ergodic layer is investigated in Figure 8.2. In Part (a) of the Figure, the radial temperature distribution across the O-point of the $3/2$ island ($\theta = \pi/3$ in the Poincaré plot) is given for various different values of the heat diffusion anisotropy. It can be seen that the temperature flattens in the individual island regions first and a flattening over the whole ergodic region is only observed for pronounced heat diffusion anisotropies. Part (b) of the Figure depicts the radial profile of the poloidally and toroidally averaged temperature distribution, $T_{0/0}$. For large $\chi_{||}/\chi_{\perp}$, the temperature flattens almost over the whole ergodic layer. This is different from single magnetic islands where the flattening of $T_{0/0}$ is incomplete in parts of the island region even for very large anisotropies as shown in Section 5.1. In Part (c) of Figure 8.2, the effective normalized radial heat diffusivity, κ_ρ, is considered. For low to moderate heat diffusion anisotropies, separate peaks of κ_ρ corresponding to the individual islands are visible. However, for large values of $\chi_{||}/\chi_{\perp}$, the effective heat diffusivity is strongly increased in the whole ergodic layer.

For a cylindrical plasma, heat transport across ergodic layers has been shown in Reference [Yu06] to be determined by the superposition of single island effects for values of w/w_c up to about unit for the individual islands. This will be demonstrated in the following. The radial distribution of some temperature harmonics ($T_{3/2}$, $T_{4/3}$, $T_{6/4}$, $T_{7/5}$, and $T_{8/6}$) are considered in Figure 8.3 for two different heat diffusion anisotropies[1]. Part (a) corresponds to a moderate heat diffusion anisotropy of $\chi_{||}/\chi_{\perp} = 2.6 \cdot 10^5$, which leads to values of w/w_c equal to 1.1 and 0.75 for the $3/2$ and $4/3$ islands, respectively. Part (b) shows computational results for $\chi_{||}/\chi_{\perp} = 6.7 \cdot 10^7$ which corresponds to values of w/w_c equal to 4.3 and 3.0, respectively. Indeed, the temperature harmonics at the ergodic layer differ only slightly from the single island results in the low anisotropy case (except for coupled modes like the $7/5$ mode which are not present in either island case) and are fundamentally different in the case with a more pronounced heat diffusion anisotropy.

The influence of an ergodic layer on the radial heat transport is shown in Figure 8.4. The relative increase of the normalized effective radial heat diffusivity, κ_ρ^+ ($\rightarrow$ Equation (5.2)), at the $7/5$ rational surface ($\rho_{7/5} = 0.419$) is plotted and compared to the sum of the single island

[1] Refer to Equation (5.3) for the definition of the $T_{m/n}$ Fourier modes.

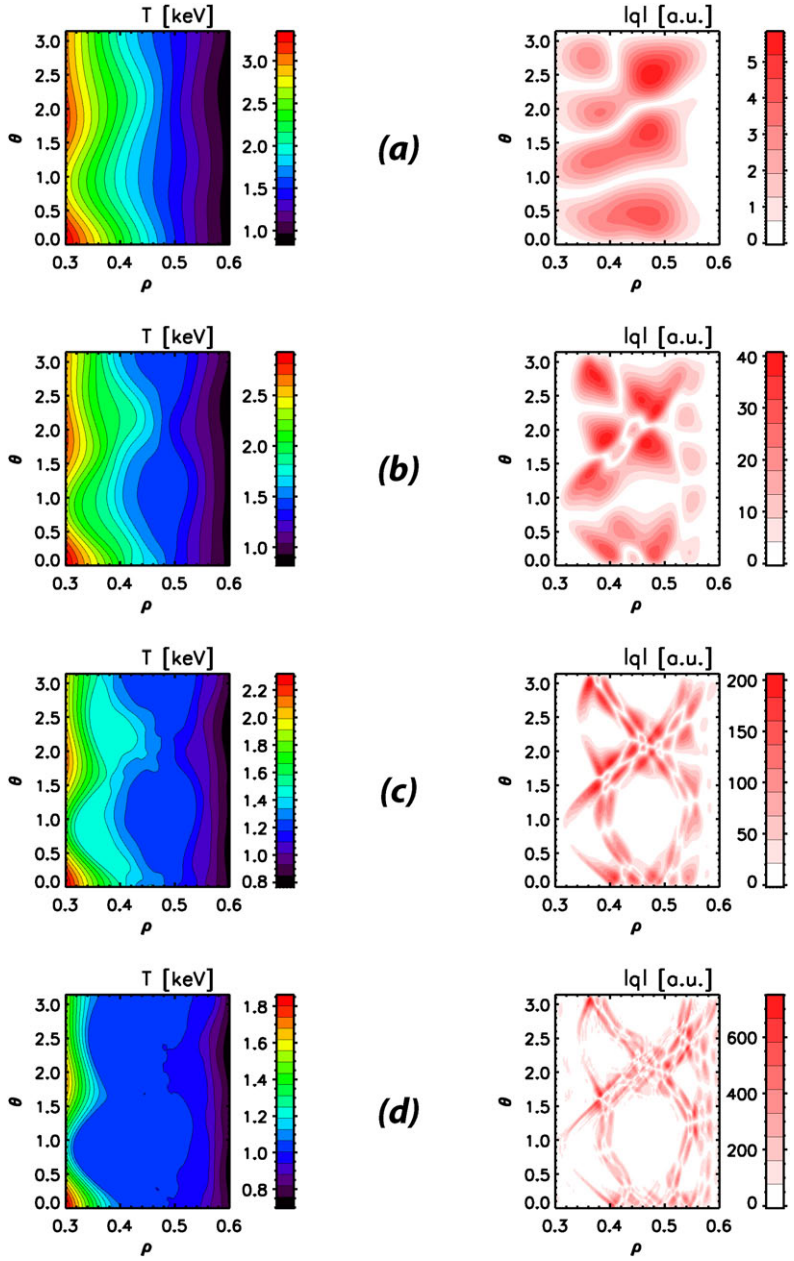

FIGURE 8.5. *Contour plots of the temperature (left) and the heat flux density $|\vec{q}|$ (right) at the ergodic layer produced by overlapping $3/2$ and $4/3$ islands are shown. Results for* **(a)** $\chi = 3 \cdot 10^5$, **(b)** $\chi = 4 \cdot 10^6$, **(c)** $\chi = 7 \cdot 10^7$, *and* **(d)** $\chi = 1 \cdot 10^9$ *are shown. Low and high field sides are located at* $\theta = 0$ *respectively* $\theta = \pi$.

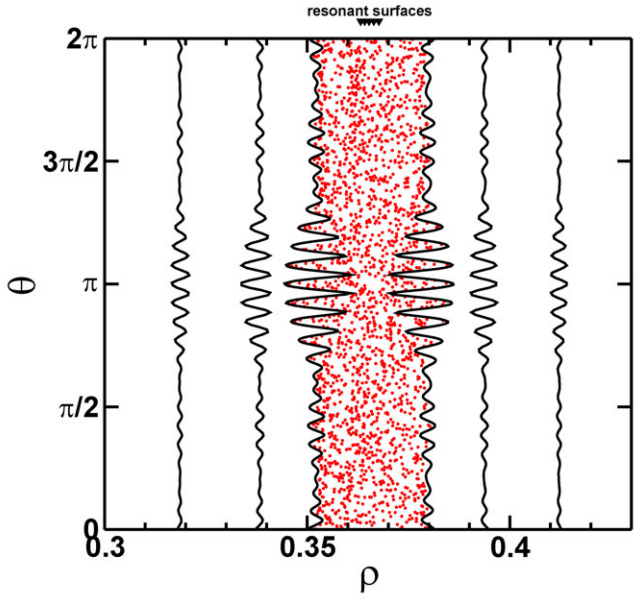

FIGURE 8.6. *Poincaré plot of the magnetic field structure of the highly ergodic case considered.*

effects. For $\chi_{||}/\chi_{\perp} \lesssim 10^7$, the heat transport across the ergodic layer is virtually equivalent to the single island effects. This corresponds to $[w/w_c]_{3/2} \lesssim 2.5$ respectively $[w/w_c]_{4/3} \lesssim 2$. For heat diffusion anisotropies beyond that, a strong increase of the radial heat diffusivity compared to single islands is observed which corresponds to the flattening of the whole ergodic region as it can be seen in Figure 8.5 that contains the heat flux densities and the corresponding temperature distributions at the ergodic layer for various heat diffusion anisotropies. The flattening of the temperature distribution starts at the individual island locations and extends over the whole ergodic layer for strong anisotropies.

8.2. Highly Stochastic Layer

In this Section, the heat transport across a highly stochastic layer produced by five magnetic perturbations ($i = 1 \ldots 5$) is examined in cylindrical geometry. The overlapping magnetic islands have the following helicities, normalized island widths, and positions of the resonant surfaces:

$$\begin{aligned} q_i &= {}^{24}/_{23}, \quad {}^{25}/_{24}, \quad {}^{26}/_{25}, \quad {}^{27}/_{26}, \quad {}^{28}/_{27}, \\ w_i/a &= 0.01876, \; 0.01841, \; 0.01808, \; 0.01777, \; 0.01747, \\ \rho_{s,i} &= 0.36767, \; 0.36642, \; 0.36526, \; 0.36418, \; 0.36317. \end{aligned}$$

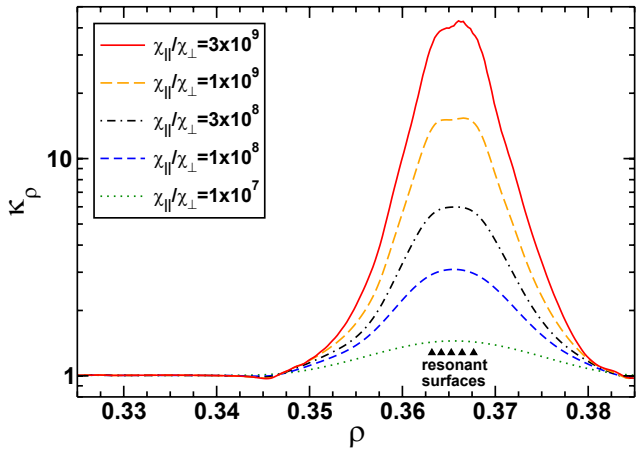

FIGURE 8.7. *The normalized effective radial heat diffusivity κ_ρ at a highly ergodic layer produced by five magnetic perturbations with very similar helicities.*

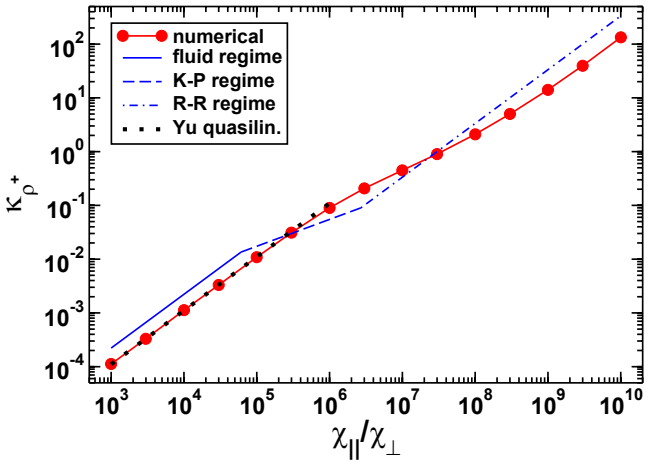

FIGURE 8.8. *κ_ρ^+ is shown at the center of the highly ergodic layer. Qualitative agreement of the numerical simulations with the classical analytical theories is observed. However, the ranges of validity of the regimes and the absolute values do not coincide. For moderate heat diffusion anisotropies, very good agreement is obtained with the quasilinear theory derived in Reference [Yu06].*

A Poincaré plot of the magnetic configuration is shown in Figure 8.6. The Chirikov parameter for two magnetic perturbations i and j is defined as

$$\sigma_{i,j} = \frac{w_i + w_j}{2|r_{s,i} - r_{s,j}|} \tag{8.4}$$

and takes values between 4 and 17.5 in the considered case depending on the choices for i and j. A "total" Chirikov parameter is defined by

$$\sigma_{tot} = \sum_{i \neq 3} \sigma_{i,3} = 48.5 \tag{8.5}$$

to characterize the total stochasticity produced by the several overlapping islands.

The numerical computations are performed in cylindrical geometry to allow for a direct comparison to the analytical predictions that were reviewed in Section 2.7. A helical coordinate system with $\iota_c = {}^{25}/_{26}$ aligned to the middle resonant surface is used. Figure 8.7 shows that the normalized effective radial heat diffusivity, κ_ρ, is increased over the whole ergodic layer. The positions of the rational surfaces are indicated. At the edge of the layer, κ_ρ drops slightly below unity due to the deformation of the flux surfaces that leads to a parallel redistribution of the heat flux within the flux surfaces. This is the same effect as is discussed in Section 5.1 for magnetic islands.

In Figure 8.8, the dependence of κ_ρ^+ on $\chi_{||}/\chi_\perp$ is shown at the position of the middle resonant surface. For small and large values of $\chi_{||}/\chi_\perp$, a linear dependence $\kappa_\rho^+ \propto \chi_{||}$ can be seen, while for intermediate values of $\chi_{||}/\chi_\perp \approx 3 \cdot 10^5 \ldots 10^9$ a reduced slope is observed in the log-log plot. Basically, these are similar dependencies as predicted by the analytical expressions given in Equations (2.57) – (2.59), which are also plotted in Figure 8.8. There are, however, two major differences:

- The ranges of validity of the regimes do not coincide. The regime boundaries found numerically are at significantly higher ratios of $\chi_{||}/\chi_\perp$ than the predicted ones.
- The analytically predicted values are larger than the numerical results by a factor of roughly two.

For the fluid regime, this is not surprising, as the more recent analytical derivation by Yu corrects the fluid regime just by this factor of two [Yu06]. This theory assumes that the heat transport across the ergodic layer is just determined by the superposition of single magnetic island effects for small ratios of w/w_c of the individual islands. Perfect agreement with this prediction is found for $w \lesssim w_c$, i.e., for $\chi_{||}/\chi_\perp \lesssim 6 \cdot 10^6$ in this case.

For the Rechester-Rosenbluth regime, an exponential field line diffusion has been assumed by the original authors [Rechester78]. Rover et. al., however, performed numerical examinations and concluded that the field line diffusion is substantially different from an exponential behavior [Rover99]. This might well be the reason for the observed deviations between the numerical results and the analytical predictions.

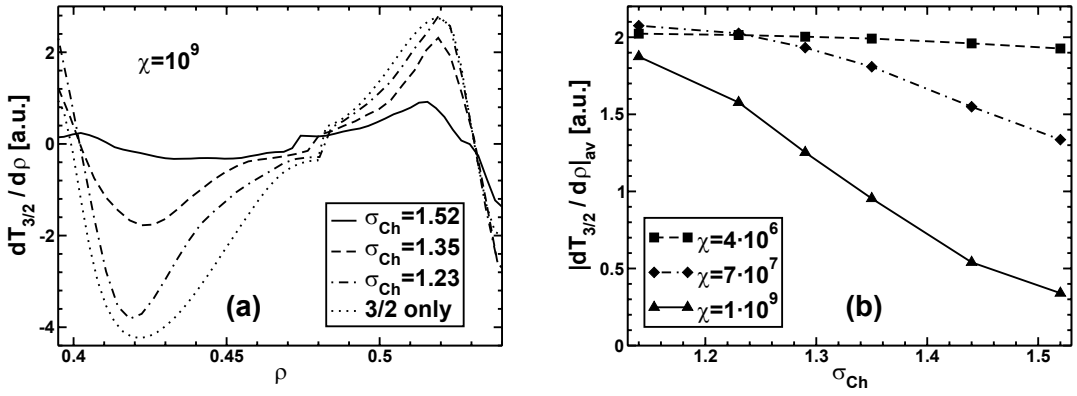

FIGURE 8.9. *(a) Radial profiles of the derivative $dT_{3/2}/d\rho$ of the first temperature harmonic are shown for a single $3/2$ island and for cases with an additional $4/3$ perturbation of increasing amplitude at $\chi = 10^9$. The $3/2$ and $4/3$ resonant surfaces are located at $\rho = 0.478$ respectively $\rho = 0.381$. (b) The average of $|dT_{3/2}/d\rho|$ in the island region is plotted. Its dependence on the Chirikov-Parameter is shown for three different heat diffusion anisotropies.*

8.3. NTMs in the Frequently Interrupted Regime

As discussed in Section 2.6, FIR-NTMs are neoclassical tearing modes which are frequently interrupted by a sudden drop of the mode amplitude. Field ergodization due to the interaction with different modes might be the reason for the fast reduction of the island size. Although it is unlikely that the mode responsible for the field ergodization is a resistive mode that creates an island at its rational surface, for simplicity the overlapping of two magnetic islands is discussed in the following. The results are easily portable to ideal modes as the ergodization is virtually the same in both cases. A $3/2$ NTM is considered with an additional $4/3$ perturbation which causes ergodization. The temperature flattening in the ergodic region reduces the resonant bootstrap current perturbation of the $3/2$ NTM significantly and therefore also the island drive. This effect is examined for a $3/2$ NTM with $w = 8.5$ cm and an additional $4/3$ perturbation of variable amplitude which corresponds to a scan of different σ_{Ch} values. Part **(a)** of Figure 8.9 shows the first derivative of the temperature mode $T_{3/2}$ for different values of σ_{Ch} at $\chi = 10^9$. It can be seen, that $dT_{3/2}/d\rho$ is strongly reduced for $\sigma_{Ch} \gtrsim 1.2$. In part **(b)** of this figure, the dependence of the averaged absolute value

$$\left|\frac{dT_{3/2}}{d\rho}\right|_{av} = \frac{\int_{0.4}^{0.54} d\rho \left|\frac{dT_{3/2}}{d\rho}\right|}{0.54 - 0.4} \tag{8.6}$$

in the island region is shown for three different values of the heat diffusion anisotropy. This quantity is suppressed strongly by stochastization for $\sigma_{Ch} \gtrsim 1.2$ and large $\chi_{||}/\chi_{\perp}$. It can be

concluded, that the resonant bootstrap current perturbation $j_{b,3/2} \propto dT_{3/2}/d\rho$ is strongly reduced due to field ergodization. This can happen on a timescale much faster than the typical resistive timescale as the stochastization enables a fast decay of the bootstrap current perturbation along magnetic field lines.

8.4. Ergodic Plasma Boundary

Coils for the production of resonant magnetic perturbation fields have been installed at several tokamak devices like DIII-D and TEXTOR which can be used to ergodize the plasma boundary (→ Section 3.4). An ergodic plasma boundary has been shown to be capable of ELM mitigation (→ Section 3.4.3). The transport of electrons along stochastic field lines is an important element in this process and may lead, e.g., to an increased heat conduction [Bécoulet04]. At the example of the active coil set projected for ASDEX Upgrade (→ Section 3.4.1), the possibility of the effect of an ergodic magnetic field on temperature gradients is investigated. The magnetic field generated by the "n=4 plus/minus phasing" of the coil set is used neglecting the plasma response to the perturbation. To account for the partial shielding of the external field by the plasma, the coil currents are reduced in return by a factor of about 5. In addition to the ergodization of the field close to the edge over a range of about 10 percent of the minor radius, some impact on the plasma shape is observed in the Poincaré plot of Figure 8.10. The plasma "grows" somewhat towards the upper divertor region.

The large gradients in the pedestal region and the separatrix geometry make heat diffusion simulations in this configuration computationally very demanding. The straight field line coordinate system used for plasma core examinations is not well-suited for the plasma edge. Computations for realistic plasma parameters are possible only with a special coordinate system which uses the real angle as poloidal coordinate (→ Section 4.3 for details). As only the pedestal region is of interest here, $\chi_\perp$ is chosen unrealistically large in the scrape-off layer to simplify convergence. From Figures 8.11 and 8.12, a clear reduction of pedestal temperature gradients is observed which reduces the pedestal height by about 20 percent. It must be noted, that these computations presume Spitzer conductivity. In Chapter 6 an indication was found that the heat diffusion anisotropy at an island in the plasma bulk is significantly smaller than the Spitzer prediction. In case this is true for the plasma boundary as well, the reduction of the temperature pedestal height would be correspondingly smaller. For an anisotropy that is lower than the Spitzer prediction by a factor of 10 or more, the ergodization of the plasma boundary does virtually not affect the temperature pedestal at all.

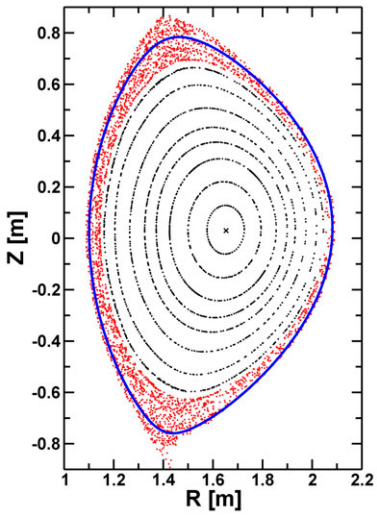

FIGURE 8.10. *Poincaré plot of the ergodic plasma boundary at ASDEX Upgrade that may be produced by the external perturbation coils. The magnetic field structure becomes stochastic in the outermost 10 percent of the minor radius. The solid line indicates the last closed magnetic surface of the unperturbed equilibrium.*

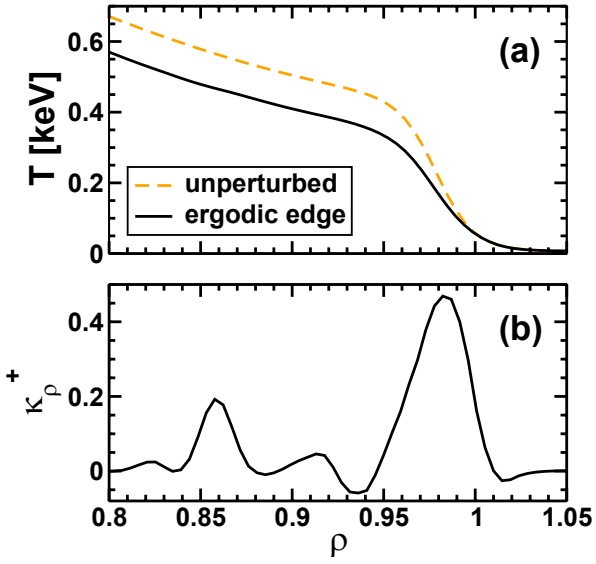

FIGURE 8.11. ***(a)*** *Radial profile of the poloidally and toroidally averaged temperature both for the equilibrium magnetic field and for the ergodized plasma boundary.* ***(b)*** *Relative increase of the normalized effective radial heat diffusivity, κ_ρ^+, due to edge stochastization.*

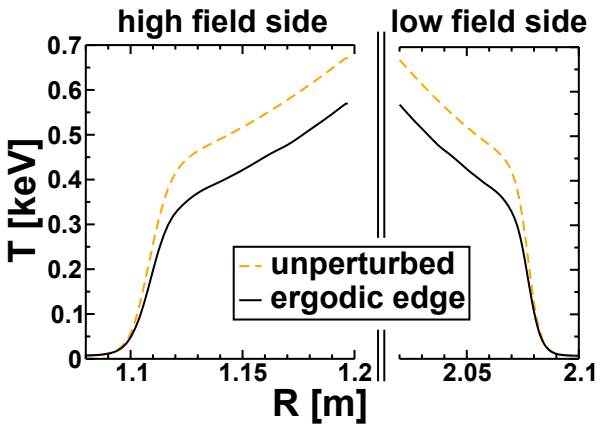

FIGURE 8.12. *Temperature cuts along the major radius at the mid-plane ($Z = 0$) of the low and high field sides for the equilibrium magnetic field configuration and for the ergodized plasma boundary.*

Chapter 9.

Summary and Conclusions

In the course of this PhD project, a novel numerical tool has been implemented that allows to examine the strongly anisotropic diffusive heat transport in realistic tokamak plasmas across magnetic islands and stochastic magnetic field layers. The employed finite difference scheme does not require an exact alignment of the coordinate system to the magnetic field lines. Computations were carried out and compared to analytical predictions as well as experimental measurements to improve the understanding of important phenomena in magnetized plasmas like magnetic islands, neoclassical tearing modes, stochastic layers, and an ergodic plasma boundary.

Code Development

The anisotropic heat diffusion equation has been presented in tensor notation to allow for large flexibility regarding the choice of coordinates. For the numerical solution of this equation in realistic toroidal geometries with realistic plasma parameters, a completely new code was developed using a finite difference approach that allows to use coordinate systems which are not aligned to the magnetic field lines despite the huge heat diffusion anisotropy. For simulations concerning the plasma core, coordinate systems were used with flux coordinate and straight field line properties. These can be transformed to unsheared helical coordinate systems which are roughly aligned to the physical problem under consideration for relaxing the toroidal resolution requirements. For computations regarding the plasma boundary, a different approach has been chosen which allows to describe the plasma and vacuum regions in a single, purely toroidal coordinate system.

Magnetic Islands and NTMs

The temperature flattening inside magnetic islands has been investigated in cylindrical and toroidal geometries. It was shown that there is a significant difference between the low and high field sides of the torus, while the basic mechanisms are very similar in both geometries. The energy confinement degradation caused by magnetic islands was examined revealing that it solely depends on the island width, w, the scale island width for temperature flattening, w_c, and the unperturbed temperature gradient at the resonant surface of the island.

The driving term of neoclassical tearing modes caused by the perturbation of the bootstrap current was computed analogously to analytical predictions, but from numerical simulation results. The analytical small and large island limits could be recovered, while a significantly higher island drive than predicted was observed at realistic ratios of w/w_c. An empirical correction factor for these predictions was derived.

The dependence of the temperature flattening at magnetic islands on the heat diffusion anisotropy, $\chi_{||}/\chi_{\perp}$, has been exploited for the determination of the experimental anisotropy values. Simulations for magnetic islands in TEXTOR and ASDEX Upgrade geometries were performed for this purpose and the resulting temperature distributions were compared to experimental measurements from ECE-Imaging. The matching of numerical and experimental signals allows to determine the island width and the heat diffusion anisotropy for individual transits of the considered mode around the torus. The uncertainty of the obtained anisotropy values is determined from the statistics of many mode transits. In both tokamak devices, heat diffusion anisotropies were detected that are lower than the Spitzer-Härm predictions by 1.7 ± 0.6 respectively 2.0 ± 0.7 orders of magnitude. This indicates that heat transport across magnetic islands is governed by the heat flux limit.

Ergodic Layers and FIR-NTMs

Heat transport across ergodic layers has been investigated. It was shown that single island effects dominate for low to moderate heat diffusion anisotropies such that the temperature flattens in the individual island regions first. At higher anisotropies, the temperature distribution flattens in the whole ergodic layer which further decreases the global energy confinement. For a highly ergodic layer produced by five overlapping magnetic islands, the effective radial heat diffusivity was compared to classical analytical predictions by Rechester and Rosenbluth, Kadomtsev and Pogutse, and others. The predicted values could not be recovered while qualitative agreement is observed. However, in the regime where w/w_c of the individual islands is small, the numerical results coincide very accurately with the more recently developed quasi-linear theory by Yu.

It was demonstrated that the resonant helical perturbation of the bootstrap current that constitutes the island drive of neoclassical tearing modes is strongly reduced when ergodization arises at the position of the NTM due to a different mode. Therefore, the sudden amplitude drop observed at NTMs in high pressure experiments (FIR-NTMs), may be caused by an ergodization of the magnetic field structure due to the interaction with an ideal MHD mode.

Heat transport was simulated in ASDEX Upgrade geometry across a plasma boundary that is ergodized by resonant magnetic perturbation coils. A considerable drop of the temperature pedestal height was observed under the assumption that Spitzer-Härm diffusivity determines the parallel heat conduction. In case the heat diffusion anisotropy is significantly lower than this prediction, as it was observed for magnetic islands in the bulk plasma in this work, the ergodization does not have a significant influence on the edge temperature profile.

Outlook

An efficient framework for simulations of heat transport in realistic tokamak geometries and an algorithm for the direct comparison to experimental temperature measurements have been developed and successfully applied to magnetic islands in different tokamak experiments. As further measurements of the temperature distribution at magnetic islands in ASDEX Upgrade will become available, the method is planned to be applied to islands at different plasma parameters, where even higher heat diffusion anisotropies are expected. The approach can easily be extended to cases with strong local heating into a magnetic island which causes a significant temperature peaking at the O-point. From such a comparison, the question could be answered, if the cross-field transport coefficient is different inside than outside the island as has been argued for.

Furthermore, it is planned to implement an improved numerical treatment of the anisotropic heat conduction equation, similar to the one used for this work, into a nonlinear MHD code to enhance its capabilities for treating realistic values of the heat diffusion anisotropy. This will lead, e.g., to an improved description of the nonlinear evolution of neoclassical tearing modes in this code or a more realistic picture for the effect of edge ergodization on ELMs. On a longer term, this enhancement might also open the door for realistic simulations of plasma disruptions, which are a major concern for ITER.

Appendix

Appendix A.

Coordinate Systems

This Chapter gives some additional information related to coordinate systems beyond the scope of Sections 4.1 and 4.3. First a brief general introduction to tensor analysis is given in Section A.1. The notation is then, in Section A.2, applied to the basic cylindrical coordinate system (R, Z, Φ). Successively, information regarding the toroidal coordinate systems is given in Section A.3. This includes details about the transformation to helical coordinates. The basis vectors and metric tensors for the general helical coordinates are derived and expressions for the divergence, gradient, curl, and the absolute value of vector quantities are given. The differential elements required for one-, two-, and three-dimensional integrals are given. Section B.4 briefly explains the iterative transformation of cylindrical coordinate values to the helical coordinate system.

Contents

A.1. Tensor Analysis

Some basics of tensor analysis are sketched briefly, here. For a comprehensive introduction to tensor notation and the most important coordinate systems used in magnetically confined fusion research, refer to Reference [D'haeseleer91]. In a curvilinear coordinate system with the coordinates (u^1, u^2, u^3), a set of basis vectors tangential to the coordinate lines is given by

$$\mathbf{e}_i = \frac{\partial \mathbf{R}}{\partial u^i}, \tag{A.1}$$

where the curvilinear coordinate system is defined by the transformation

$$\begin{pmatrix} x \\ y \\ z \end{pmatrix} = \mathbf{R}(u^1, u^2, u^3). \tag{A.2}$$

A second important coordinate system is given by

$$\mathbf{e}^i = \frac{\mathbf{e}_j \times \mathbf{e}_k}{\mathbf{e}_i \cdot (\mathbf{e}_j \times \mathbf{e}_k)}, \tag{A.3}$$

where the basis vectors $\mathbf{e}^i$ are perpendicular to the $u^i = const$ surfaces and (i, j, k) is a cyclic permutation of $(1, 2, 3)$. Any vector can be expressed in either coordinate system by

$$\mathbf{A} = \sum_i A_i \mathbf{e}^i = \sum_i A^i \mathbf{e}_i. \tag{A.4}$$

The components A_i are the covariant components of the vector $\mathbf{A}$, while A^i denotes contravariant components. The so-called Einstein summation convention can be applied, according to which an implicit summation is carried out over any index that appears as a sub- and a superscript within the same term. Sub- and superscripts in the denominator are regarded as the opposite in this context. This allows to omit summation signs in many cases. For example, $a_i b^i \equiv \sum_i a_i b^i$ and $a^i / b^i \equiv \sum_i a^i / b^i$ imply a summation, while $a_i b_i$ and a_i / b^i do not.

The components $g_{ij} = \mathbf{e}_i \cdot \mathbf{e_j}$ respectively $g^{ij} = \mathbf{e}^i \cdot \mathbf{e^j}$ of the metric tensors are called metric coefficients. The determinants of the matrices g_{ij} respectively g^{ij} are denoted g and g^{-1}. Vector components can be transformed between the co- and contravariant components utilizing the metric tensors by

$$A_i = g_{ij} A^j \tag{A.5}$$

respectively

$$A^i = g^{ij} A_j. \tag{A.6}$$

Using this, the dot product of two vectors can be expressed in four different ways by

$$\mathbf{A} \cdot \mathbf{B} = A^i B_i = A_i B^i = g_{ij} A^i B^j = g^{ij} A_i B_j. \tag{A.7}$$

With the Levi-Civita symbol,

$$\varepsilon^{ijk} = \varepsilon_{ijk} = \begin{cases} +1, & \text{if } (i, j, k) \text{ form an even permutation of } (1, 2, 3) \\ -1, & \text{if } (i, j, k) \text{ form an odd permutation of } (1, 2, 3) \\ 0, & \text{otherwise,} \end{cases} \tag{A.8}$$

components of the cross product of two vectors **A** and **B** can be written in the forms

$$(\mathbf{A}\times\mathbf{B})_k = \varepsilon_{ijk}\sqrt{g}A^iB^j \tag{A.9}$$

respectively

$$(\mathbf{A}\times\mathbf{B})^k = \frac{\varepsilon^{ijk}}{\sqrt{g}}A_iB_j. \tag{A.10}$$

A.2. Cylindrical Coordinates

Cylindrical coordinates, which form the basis coordinate system for the definition of the toroidal coordinate systems required in this work, are defined by $x = R\cos\Phi$, $y = R\sin\Phi$, and $z = Z$. These are right-handed, orthogonal, and unnormalized. The covariant basis vectors $\mathbf{e}_\alpha = \partial\mathbf{R}/\partial u^{\alpha,cyl}$ are

$$\mathbf{e}_R = (\cos\Phi,\ \sin\Phi,\ 0), \qquad |\mathbf{e}_R| = 1, \tag{A.11}$$
$$\mathbf{e}_\Phi = (-R\sin\Phi,\ R\cos\Phi,\ 0), \qquad |\mathbf{e}_\Phi| = R, \tag{A.12}$$
$$\mathbf{e}_Z = (0,\ 0,\ 1), \qquad |\mathbf{e}_Z| = 1. \tag{A.13}$$

The contravariant basis vectors are $\mathbf{e}^R = \mathbf{e}_R$, $\mathbf{e}^\Phi = \mathbf{e}_\Phi/R^2$, and $\mathbf{e}^Z = \mathbf{e}_Z$. The metric tensor takes the form $g_{\alpha\beta} = \mathbf{e}_\alpha\cdot\mathbf{e}_\beta = \mathrm{diag}(1,\ R^2,\ 1)$ respectively $g^{\alpha\beta} = \mathrm{diag}(1,\ 1/R^2,\ 1)$. Its determinant is $g = \det\left(g_{\alpha\beta}\right) = R^2$. The vector operations gradient, divergence and curl are defined as

$$\nabla U = \frac{\partial U}{\partial R}\mathbf{e}^R + \frac{\partial U}{\partial\Phi}\mathbf{e}^\Phi + \frac{\partial U}{\partial Z}\mathbf{e}^Z, \tag{A.14}$$
$$\nabla\cdot\mathbf{V} = \frac{1}{R}\frac{\partial(RV^R)}{\partial R} + \frac{\partial V^\Phi}{\partial\Phi} + \frac{\partial V^Z}{\partial Z}, \tag{A.15}$$
$$\nabla\times\mathbf{V} = \left[\frac{1}{R}\frac{\partial V_Z}{\partial\Phi} - \frac{\partial V_\Phi}{\partial Z}\right]\mathbf{e}_R + \left[\frac{\partial V_R}{\partial Z} - \frac{\partial V_Z}{\partial R}\right]\mathbf{e}_\Phi + \frac{1}{R}\left[\frac{\partial RV_\Phi}{\partial R} - \frac{\partial V_R}{\partial\Phi}\right]\mathbf{e}_Z. \tag{A.16}$$

A.3. Toroidal Coordinate Systems

A transformation between cylindrical coordinates and toroidal coordinates $(\rho,\tilde{\theta},\phi)$, which are usually chosen to be, both, flux coordinates[1] and straight field line coordinates[2] for our

[1] In flux coordinate systems, magnetic flux surfaces coincide with $\rho = const$ coordinate surfaces.
[2] Magnetic field lines simplify to straight lines in straight field line coordinate systems.

purposes, can be written in Fourier expanded form as

$$R = \sum_{m,n} \left[R_{m,n}(\rho) \sin(m\tilde{\theta} + n\phi) + \tilde{R}_{m,n}(\rho) \cos(m\tilde{\theta} + n\phi) \right], \tag{A.17}$$

$$\Phi = \phi + \sum_{m,n} \left[V_{m,n}(\rho) \sin(m\tilde{\theta} + n\phi) + \tilde{V}_{m,n}(\rho) \cos(m\tilde{\theta} + n\phi) \right], \tag{A.18}$$

$$Z = \sum_{m,n} \left[Z_{m,n}(\rho) \sin(m\tilde{\theta} + n\phi) + \tilde{Z}_{m,n}(\rho) \cos(m\tilde{\theta} + n\phi) \right]. \tag{A.19}$$

It is uniquely determined for given profiles of the Fourier coefficients $R_{m,n}(\rho)$, $\tilde{R}_{m,n}(\rho)$, $V_{m,n}(\rho)$, $\tilde{V}_{m,n}(\rho)$, $Z_{m,n}(\rho)$ and $\tilde{Z}_{m,n}(\rho)$. The coefficients $R_{m,n}(\rho)$, $\tilde{R}_{m,n}(\rho)$, $Z_{m,n}(\rho)$ and $\tilde{Z}_{m,n}(\rho)$ have the unit $[m]$, while $V_{m,n}(\rho)$ and $\tilde{V}_{m,n}(\rho)$ are unit-less. A simplified version of this transformation that is restricted to axi-symmetric coordinate systems with $\phi = \Phi$, as they are exclusively used in this work, is discussed in Section 4.3.2. A radial grid meshing can be applied to locally enhance the radial resolution wherever this may be required, for example at magnetic islands. The grid meshing is explained in Section 4.3.

Helical Coordinate System

Straight field line coordinates can be further transformed in sections according to

$$\theta = \tilde{\theta} - \iota_c(\rho) \cdot (\phi - \phi_p), \text{ for } \phi_p \leq \phi < \phi_{p+1}, \tag{A.20}$$

which changes Equations (A.17) – (A.19) to

$$R = \sum_{m,n} \left[R_{m,n} S_{m,n} + \tilde{R}_{m,n} C_{m,n} \right], \tag{A.21}$$

$$\Phi = \phi + \sum_{m,n} \left[V_{m,n} S_{m,n} + \tilde{V}_{m,n} C_{m,n} \right], \tag{A.22}$$

$$Z = \sum_{m,n} \left[Z_{m,n} S_{m,n} + \tilde{Z}_{m,n} C_{m,n} \right]. \tag{A.23}$$

Here,

$$\begin{aligned} p &= 0 \ldots P-1, \\ \phi_p &= 2\pi p / P, \\ S_{m,n} &= \sin\left[m\theta + m\iota_c(\phi - \phi_p) + n\phi \right], \\ C_{m,n} &= \cos\left[m\theta + m\iota_c(\phi - \phi_p) + n\phi \right]. \end{aligned}$$

The effect of the transformation depends on the choice of ι_c:

- If $\iota_c(\rho) = \iota(\rho)$, the coordinates $u^\alpha = \rho, \theta, \phi$ are field aligned, meaning $\mathbf{e}_\phi \mid\mid \mathbf{B}_0$ ("full" alignment).

- For $\iota_c = const$, field alignment is achieved at one rational surface where $\iota(\rho) = \iota_c$ only ("partial" alignment).

- For $\iota_c = 0$, the coordinates remain unchanged (no alignment).

The advantages and disadvantages of full and partial coordinate alignment are discussed in Section 4.3.4 leading to the use of coordinate systems that are only roughly aligned to the physical problem by choosing an adequate fixed value of ι_c in this work. Additionally, the numerical errors turned out to be smallest for $P = 1$, i.e., for a transformation of the full toroidal range of the coordinate system in one section.

Basis Vectors and Metric Tensors

The, in general non-orthogonal and unnormalized, covariant basis vectors

$$\mathbf{e}_{\alpha,hel}\ [m] = \mathbf{e}_{\beta,cyl} \frac{\partial u^{\beta,cyl}}{\partial u^{\alpha,hel}} \tag{A.24}$$

of the helical coordinate system are

$$\begin{aligned}
\mathbf{e}_\rho = {} & \mathbf{e}_R \sum_{m,n} \left[(R'_{m,n} - m(\phi - \phi_p)\iota'_c \tilde{R}_{m,n}) S_{m,n} + (\tilde{R}'_{m,n} + m(\phi - \phi_p)\iota'_c R_{m,n}) C_{m,n} \right] \\
& + \mathbf{e}_\Phi \sum_{m,n} \left[(V'_{m,n} - m(\phi - \phi_p)\iota'_c \tilde{V}_{m,n}) S_{m,n} + (\tilde{V}'_{m,n} + m(\phi - \phi_p)\iota'_c V_{m,n}) C_{m,n} \right] \\
& + \mathbf{e}_Z \sum_{m,n} \left[(Z'_{m,n} - m(\phi - \phi_p)\iota'_c \tilde{Z}_{m,n}) S_{m,n} + (\tilde{Z}'_{m,n} + m(\phi - \phi_p)\iota'_c Z_{m,n}) C_{m,n} \right],
\end{aligned} \tag{A.25}$$

$$\begin{aligned}
\mathbf{e}_\theta = {} & \mathbf{e}_R \sum_{m,n} m \left[-\tilde{R}_{m,n} S_{m,n} + R_{m,n} C_{m,n} \right] + \mathbf{e}_\Phi \sum_{m,n} m \left[-\tilde{V}_{m,n} S_{m,n} + V_{m,n} C_{m,n} \right] \\
& + \mathbf{e}_Z \sum_{m,n} m \left[-\tilde{Z}_{m,n} S_{m,n} + Z_{m,n} C_{m,n} \right],
\end{aligned} \tag{A.26}$$

$$\begin{aligned}
\mathbf{e}_\phi = {} & \mathbf{e}_R \sum_{m,n} (m\iota_c + n) \left[-\tilde{R}_{m,n} S_{m,n} + R_{m,n} C_{m,n} \right] \\
& + \mathbf{e}_\Phi \left(1 + \sum_{m,n} (m\iota_c + n) \left[-\tilde{V}_{m,n} S_{m,n} + V_{m,n} C_{m,n} \right] \right) \\
& + \mathbf{e}_Z \sum_{m,n} (m\iota_c + n) \left[-\tilde{Z}_{m,n} S_{m,n} + Z_{m,n} C_{m,n} \right].
\end{aligned} \tag{A.27}$$

In the following "*hel*" will be dropped in the notation. The determinant of the covariant metric tensor,

$$\begin{aligned} g_{\alpha\beta}\,[m^2] = \mathbf{e}_\alpha \cdot \mathbf{e}_\beta &= \frac{\partial R}{\partial u^\alpha}\frac{\partial R}{\partial u^\beta}(\mathbf{e}_R)^2 + \frac{\partial \Phi}{\partial u^\alpha}\frac{\partial \Phi}{\partial u^\beta}(\mathbf{e}_\Phi)^2 + \frac{\partial Z}{\partial u^\alpha}\frac{\partial Z}{\partial u^\beta}(\mathbf{e}_Z)^2 \\ &= \frac{\partial R}{\partial u^\alpha}\frac{\partial R}{\partial u^\beta} + R^2\frac{\partial \Phi}{\partial u^\alpha}\frac{\partial \Phi}{\partial u^\beta} + \frac{\partial Z}{\partial u^\alpha}\frac{\partial Z}{\partial u^\beta}, \end{aligned} \tag{A.28}$$

is given by

$$g\,[m^6] = g_{11}g_{22}g_{33} + 2g_{12}g_{13}g_{23} - g_{11}(g_{23})^2 - g_{22}(g_{13})^2 - g_{33}(g_{12})^2, \tag{A.29}$$

where $g_{ij} = g_{ji}$ was used. From matrix inversion, the contravariant metric tensor is found to be

$$(g^{\alpha\beta})\,[m^{-2}] = -\frac{1}{g}\begin{pmatrix} (g_{23})^2 - g_{22}g_{33} & -g_{13}g_{23} + g_{12}g_{33} & g_{13}g_{22} - g_{12}g_{23} \\ -g_{13}g_{23} + g_{12}g_{33} & (g_{13})^2 - g_{11}g_{33} & -g_{12}g_{13} + g_{11}g_{23} \\ g_{13}g_{22} - g_{12}g_{23} & -g_{12}g_{13} + g_{11}g_{23} & (g_{12})^2 - g_{11}g_{22} \end{pmatrix}. \tag{A.30}$$

The contravariant basis vectors can be determined from $\mathbf{e}^i\,[m^{-1}] = g^{ij}\cdot\mathbf{e}_j$.

Divergence, Gradient, Curl, and Absolute Value

Expression for the divergence of the heat flux density and the gradient of the temperature in tensor notation are given by

$$\nabla\cdot\mathbf{q}\,[Js^{-1}m^{-3}] = \frac{1}{\sqrt{g}}\frac{\partial}{\partial u^\alpha}(\sqrt{g}\mathbf{q}\cdot\mathbf{e}^\alpha) = \frac{1}{\sqrt{g}}\frac{\partial}{\partial u^\alpha}(\sqrt{g}q^\alpha), \tag{A.31}$$

$$\nabla T\,[Jm^{-1}] = (\nabla T)_\alpha\cdot\mathbf{e}^\alpha = \frac{\partial T}{\partial u^\alpha}\mathbf{e}^\alpha. \tag{A.32}$$

The parallel temperature gradient (parallel to the magnetic field direction) is given by

$$\nabla_{||}T\,[Jm^{-1}] = \mathbf{b}\,(\mathbf{b}\cdot\nabla T) = b^\alpha b^\beta\frac{\partial T}{\partial u^\alpha}\mathbf{e}_\beta = \left[\nabla_{||}T\right]^\beta\mathbf{e}_\beta. \tag{A.33}$$

The curl of the magnetic field vector is expressed by

$$\nabla\times\mathbf{B} = \frac{\partial B_\beta}{\partial u^\alpha}\mathbf{e}^\alpha\times\mathbf{e}^\beta = \frac{\varepsilon^{\alpha\beta\gamma}}{\sqrt{g}}\frac{\partial B_\beta}{\partial u^\alpha}\mathbf{e}_\gamma, \tag{A.34}$$

where

$$\varepsilon^{\alpha\beta\gamma} = \begin{cases} +1 & \text{if } (\alpha,\beta,\gamma) \text{ forms an even permutation of } (1,2,3), \\ -1 & \text{if } (\alpha,\beta,\gamma) \text{ forms an uneven permutation of } (1,2,3), \\ 0 & \text{otherwise.} \end{cases} \tag{A.35}$$

The absolute value of any vector quantity $\mathbf{v}$ is given by

$$|\mathbf{v}| = \sqrt{(\mathbf{v})^2} = |v^\alpha \sqrt{g_{\alpha\alpha}}| = |v_\alpha \sqrt{g^{\alpha\alpha}}|. \tag{A.36}$$

Differential Elements and Integration

The differential elements of the helical coordinates are given by

$$dl(\alpha) = h_\alpha du^\alpha, \tag{A.37}$$

$$dS(\alpha) = h_\beta h_\gamma du^\beta du^\gamma, \tag{A.38}$$

$$d^3R = \sqrt{g} d\rho d\theta d\phi. \tag{A.39}$$

Here, the Einstein summation convention is *not* applied and $h_\alpha = |\mathbf{e}_\alpha| = \sqrt{g_{\alpha\alpha}}$ denotes the scale factor, $dl(\alpha)$ the one-dimensional differential element in direction u^α, $dS(\alpha)$ the two-dimensional differential element in the $u^\alpha = const$ surface, and d^3R the three-dimensional differential element. The three-dimensional differential element is, e.g., required for the integration over the plasma density to determine the total number of plasma particles

$$\begin{aligned} N &= \int_V d^3R\, n(\rho,\theta,\phi) = \int_0^{2\pi} d\phi \int_0^{2\pi} d\theta \int_{\rho_{min}}^{\rho_{max}} d\rho \sqrt{g}\, n(\rho,\theta,\phi) \\ &\approx \sum_{p,k,j,i} \Delta\phi\ \Delta\theta\ \Delta\rho\ \sqrt{g_{pkji}}\, n_{pkji}. \end{aligned} \tag{A.40}$$

In the same way, but with the two-dimensional differential element, the poloidally and toroidally averaged temperature profile

$$\begin{aligned} T_{\%}(\rho) &= \frac{\int_{S(\rho)} dS(\rho)\, T(\rho,\theta,\phi)}{\int_{S(\rho)} dS(\rho)} = \frac{\int_0^{2\pi} d\phi \int_0^{2\pi} d\theta \sqrt{g_{\theta\theta}} \sqrt{g_{\phi\phi}} T(\rho,\theta,\phi)}{\int_0^{2\pi} d\phi \int_0^{2\pi} d\theta \sqrt{g_{\theta\theta}} \sqrt{g_{\phi\phi}}} \\ &\approx \frac{\sum_{p,k,j} \Delta\theta\Delta\phi \sqrt{g_{\theta\theta,pkji}\ g_{\phi\phi,pkji}}\, T_{pkji}}{\sum_{p,k,j} \Delta\theta\Delta\phi \sqrt{g_{\theta\theta,pkji}\ g_{\phi\phi,pkji}}} \end{aligned} \tag{A.41}$$

is determined.

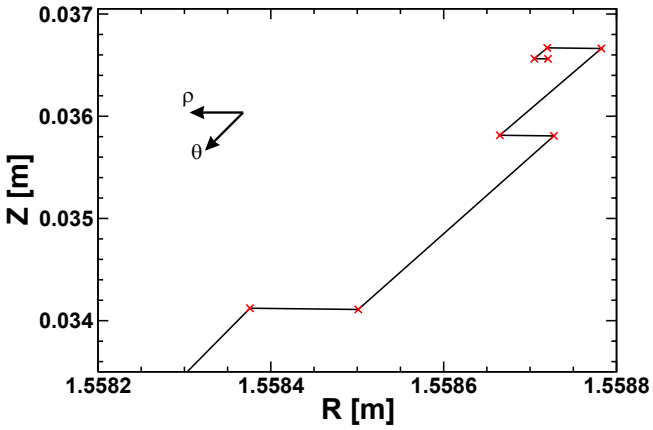

FIGURE A.1. *Convergence of the coordinate transformation algorithm for an example point in TEXTOR geometry.*

A.4. Coordinate Transformations

The transformation from helical to cylindrical coordinates can easily be performed using Equations (A.17) – (A.19). For the opposite transformation, an algorithm has been implemented, which iteratively finds the array of (ρ, θ) coordinates corresponding to a given array of (R, Z) coordinates at a given value of ϕ and a given accuracy. For instance, this allows to transform a Poincaré plot to helical coordinates (e.g., → Figure 8.1). The algorithm is given in the following in pseudo-code notation:

```
for every point that needs to be transformed, do
    > Select an initial guess for rho.
    > Select the best out of five initial guesses for theta.
    while the transformation error is too large, do
        > Select the largest i for which the transformation
          error decreases with rho = rho + drho * 2^i.
        > Select the largest j for which the transformation
          error decreases with theta = theta + dtheta * 2^j.
  done
done
```

The convergence of the algorithm by alternating iteration steps in ρ and θ directions is shown for an example point in Figure A.1.

Appendix B.

Implementation

This Chapter gives some additional information beyond the scope of Section 4.4 on the implementation of the heat transport codes used in this work. First, the interplay with existing numerical codes that were used for this work is illustrated by a flow-chart in Section B.1. Then, Section B.2 describes the Fortran modules that were implemented for use by the heat diffusion codes and several auxiliary codes. Successively, Section B.3 gives information about the postprocessing tool that was implemented for the extraction of the relevant information from the results of heat diffusion simulations. Finally, the algorithm applied for the matching of numerical simulations results to experimental temperature measurements in Chapters 6 and 7 is described in Section B.4.

Contents

B.1. Code Interplay

Figure B.1 gives an overview of the interplay between the code package for MHD equilibrium reconstruction (e.g., `VACFIELD`, `VMEC/NEMEC`, `COTRANS`, `MFBE`, `GOURDON`), which is described in Section 4.3.1, and some of the codes that were implemented for heat diffusion simulations in this work (`chi_par_det`, `MESH_TRAFO`, `EXPANDER`, `HEATs`, `POSTPROC`).

B.2. Fortran Modules

In the following, the most important multi-purpose modules that were implemented to be used, e.g., by the `HEATs` and `POSTPROC` codes, are listed in alphabetical order. The module names are given along with a short description of the module purpose. A comprehensive documentation is available for this library of Fortran modules with its source code.

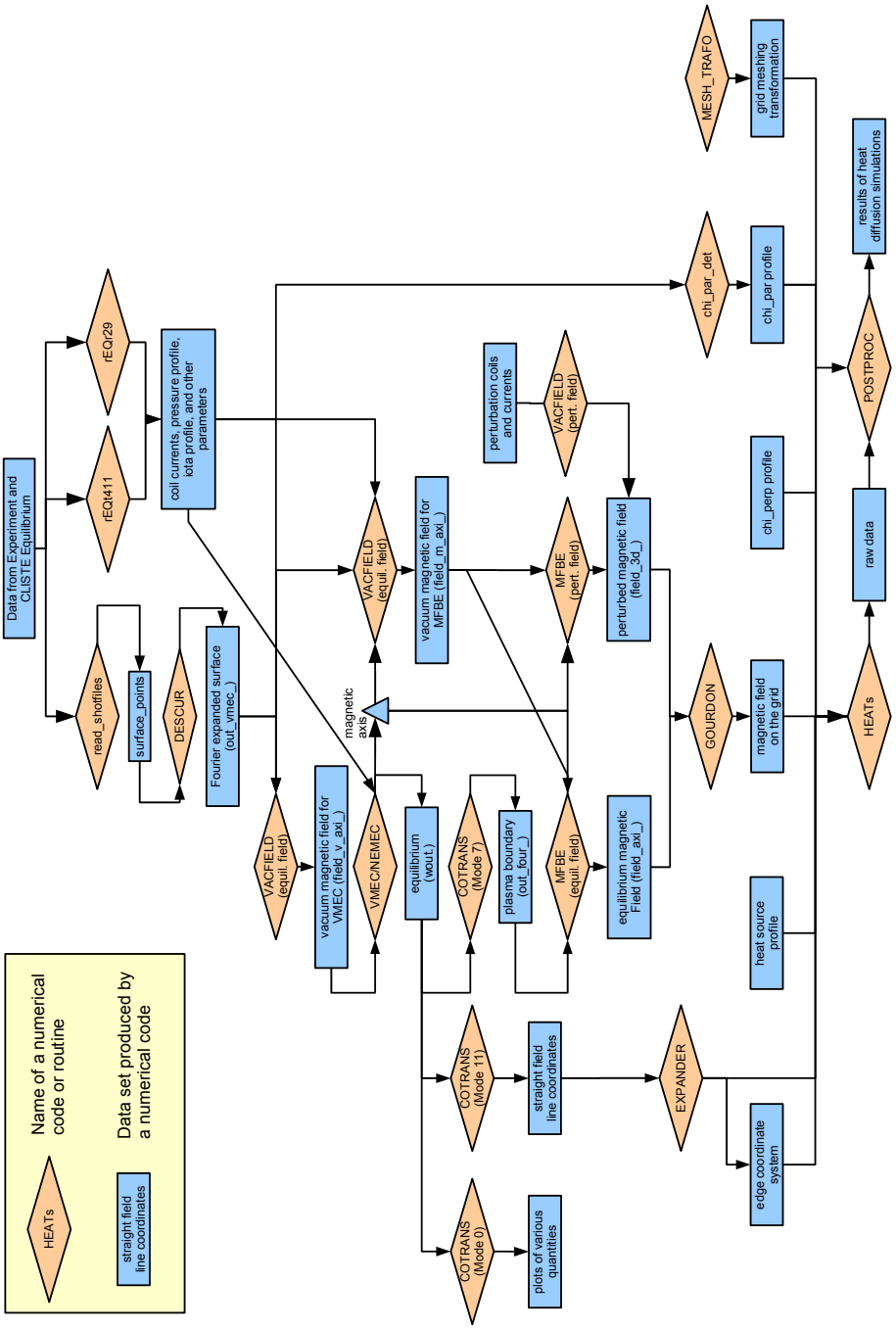

FIGURE B.1. *The flow-chart shows the interplay of the various codes required for the steps from equilibrium reconstruction to heat diffusion simulations.*

- `mod_const`
  Contains physical and mathematical constants.

- `mod_coord`
  Definition of toroidal coordinate systems.

- `mod_grid`
  Discretization grid for a toroidal coordinate system.

- `mod_io`
  Data structures and routines for data input and output.

- `mod_list`
  Routines for handling lists (one-dimensional arrays).

- `mod_logfile`
  Routines dealing with the logfile.

- `mod_metric`
  Metric tensors and related quantities for toroidal coordinates.

- `mod_prof`
  One-dimensional profiles of scalar quantities.

- `mod_qtty`
  Scalar, vectorial or tensorial quantities on a toroidal coordinate grid.

- `mod_solve`
  Solving systems of equations using, e.g., the `WSMP` package.

- `mod_sparse`
  Routines for dealing with sparse matrices.

- `mod_state`
  Input/Output of a set of physical quantities. Information from a state written out by the `HEATs` code can be processed by the `POSTPROC` code for data extraction.

- `mod_tostr`
  Conversion of various data into character strings.

- `mod_trafo`
  One dimensional coordinate transformations, e.g., for grid meshing.

B.3. Postprocessing Tool

The HEATs code writes out the computational data in a raw data format using the module mod_state mentioned in the previous Section. The raw data needs to be post-processed for an extraction of the required data, e.g., the temperature along a certain line in the plasma. The POSTPROC code that was implemented for this purpose allows to perform this task either interactively or using its basic scripting capabilities. Some explanations on the usage are available in interactive mode upon entering the "help" command. In the following, an example script for post-processing is listed which can be applied to the raw data of several HEATs code runs without modifications.

```
! Read the data corresponding to time-step 1:
READSTATE
  1

! Write out the 0/0 mode of the temperature:
GETQTTY
  T
WRITMODE
  0 0

! Write out the temperature along the line from
! (R,Phi,Z)=(1.6,0.15,0.) to (2.0,0.15,0.) on 50 points:
WRITCUT
  1.6 0.15 0.
  2.0 0.15 0.
  50

! Write out the parallel heat flux density for IDL plotting:
GETQTTY
  qpar
WRIT4IDL

EXIT
```

B.4. Matching of Experimental and Numerical Data

For the comparison between temperature measurements and numerical heat diffusion simulations that is described in Chapter 6, an automatic matching between experimental temperature signals $E_1, E_2, \ldots E_6$ and the numerical signals $N_i, N_{i+4}, \ldots N_{i+20}$ is required. In this Section, the corresponding algorithm that was implemented for this purpose is briefly described.

For every matching attempt between the measurements of a mode-transit and a numerical computation, the quadratic differences between numerical signals $N_i, N_{i+4}, \ldots N_{i+20}$ and experimental channels $E_1, E_2, \ldots E_6$ are pair-wisely integrated over the full transit ($\phi = 0 \ldots 2\pi$) giving the quadratic differences $Q_1 \ldots Q_6$ for each channel-pair. The total quadratic difference between the measured mode-transit and the numerical simulation is then given by $Q = \sum_{k=1\ldots6} Q_k$. The small deviations between the average experimental and numerical temperatures resulting from fluctuations in the experiment are removed prior to the determination of the quadratic differences. The cross-calibration between the channels is naturally not altered by this procedure and remains constant during the whole comparison.

The most reasonable value for the index i that determines which numerical signals are matched to the experimental channels is chosen for any combination of an experimental measurement and a numerical computation by minimizing Q. Then, for every mode-transit, again by minimizing Q, the numerical computation is selected that reproduces the measured temperature distribution during the mode-transit best. This way, an estimate for w and $\chi_{||}/\chi_{\perp}$ is obtained for each mode-transit independently. In summary, the algorithm is as follows written in pseudo-code:

```
for every measured mode-transit, do
    for every numerical computation, do
        for every value of i, do
            Determine the quadratic difference Q
            between measurement and simulation.
        done;
        Select the value for i with minimal Q.
    done;
    Select the numerical simulation with minimal Q.
done;
```

Index

Bibliography

[Bécoulet04] Bécoulet, M., Huysmans, G., Ghendrih, P., et al. Non-linear heat transport modelling with edge localized modes and plasma edge control in tokamaks. In *20th IAEA Fusion Energy Conference, TH/1-3Rc* (2004). URL http://www-pub.iaea.org/MTCD/Meetings/PDFplus/fusion-20-preprints/TH_1-3Rc.pdf.

[Boozer80] Boozer, A.H. Guiding center drift equations. *Phys. Fluids*, **23**, 904 (1980). doi:10.1063/1.863080.

[Boyd03] Boyd, T.J.M. and Sanderson, J.J. *The Physics of Plasmas*. Cambridge University Press (2003). ISBN 0-521-45912-5.

[Braginskii65] Braginskii, S.I. *Reviews of Plasma Physics*, volume 1, pages 205–311. Consultants Bureau, New York (1965).

[Callen92] Callen, J.D. Transport processes in magnetically confined plasmas. *Phys. Fluids B*, **4**(7), 2142 (1992). doi:10.1063/1.860021.

[Carrera86] Carrera, R., Hazeltine, R.D., and Kotschenreuther, M. Island bootstrap current modification of the nonlinear dynamics of the tearing mode. *Phys. Fluids*, **29**(4), 899 (1986). doi:10.1063/1.865682.

[Chang90] Chang, Z. and Callen, J.D. Global energy confinement degradation due to macroscopic phenomena in tokamaks. *Nucl. Fusion*, **30**(2), 219–233 (1990).

[Chang92] Chang, Z. and Callen, J.D. Unified fluid/kinetic description of plasma microinstabilities. Part II: Applications. *Phys. Fluids B*, **4**(5), 1182 (1992). doi:10.1063/1.860126.

[Chang94] Chang, Z., Fredrickson, E., Callen, J., et al. Transport effects of low (m,n) MHD modes on TFTR supershots. *Nuclear Fusion*, **34**(10), 1309–1336 (1994). doi:10.1088/0029-5515/34/10/I03.

[Chang95] Chang, Z., Callen, J.D., Fredrickson, E.D., Budny, R.V., Hegna, C.C., McGuire, K.M., Zarnstorff, M.C., and TFTR group. Observation of nonlinear neoclassical pressure-gradient-driven tearing modes in TFTR. *Phys. Rev. Lett*, **74**, 4663 (1995). doi:10.1103/PhysRevLett.74.4663.

[Chapman53] Chapman, S. and Cowling, T.G. *Mathematical theory of non-uniform gases*. Cambridge University Press (1953).

[Chirikov79] Chirikov, B.V. A universal instability of many-dimensional oscillator systems. *Phys. Rep.*, **52**(5), 263–379 (1979). doi:10.1016/0370-1573(79)90023-1.

[Classen07] Classen, I. *Imaging and Control of Magnetic Islands in Tokamaks*. Ph.D. thesis, Technische Universiteit Eindhoven, Netherlands (2007). URL http://alexandria.tue.nl/extra2/200710705.pdf.

[Classen09] Classen, I. (2009). Private Communication.

[Coelho04] Coelho, R., Lazzaro, E., and Zanca, P. Mode coupling effects on the triggering of neoclassical tearing modes and plasma momentum braking. In *Proceedings of the 20th IAEA Fusion Energy Conference*, pages TH/P5–2. IAEA, Vienna (2004). URL http://www-pub.iaea.org/MTCD/Meetings/PDFplus/fusion-20-preprints/TH_P5-2.pdf.

[Connor85] Connor, J.W. and Hastie, R.J. *The Effect of Shaped Plasma Cross Sections on the Ideal Kink Mode in a Tokamak*. Rep. CLM-M106, Culham Laboratory, Abingdon (1985).

[Connor98] Connor, J.W., Hastie, R.J., and Wilson, H.R. Magnetohydrodynamic stability of tokamak edge plasmas. *Phys. Plasmas*, **5**, 2687 (1998). doi:10.1063/1.872956.

[D'haeseleer91] D'haeseleer, W.D., Hitchon, W.N.G., Callen, J.D., and Shohet, J.L. *Flux Coordinates and Magnetic Field Structure: A Guide to a Fundamental Tool of Plasma Theory*. Springer (1991). ISBN 978-0387524191.

[Evans04] Evans, T.E., Moyer, R.A., Thomas, P.R., et al. Suppression of large edge-localized modes in high-confinement DIII-D plasmas with a stochastic magnetic boundary. *Phys. Rev. Letters*, **92**(23), 235003 (2004). doi:10.1103/PhysRevLett.92.235003.

[Evans08] Evans, T., Fenstermacher, M., Moyer, R., et al. RMP ELM suppression in DIII-D plasmas with ITER similar shapes and collisionalities. *Nuclear Fusion*, **48**(2), 024002 (2008). doi:10.1088/0029-5515/48/2/024002.

[Finken97] Finken, K.H. Special issue. *Fusion Eng. Design*, **37**(3), 335–448 (1997). doi:10.1016/S0920-3796(97)00073-2.

[Fitzpatrick93] Fitzpatrick, R., Hastie, R., Martin, T., and Roach, C. Stability of coupled tearing modes in tokamaks. *Nuclear Fusion*, **33**(10), 1533–1576 (1993).

ISSN 0029-5515. doi:10.1088/0029-5515/33/10/I11.

[Fitzpatrick95] Fitzpatrick, R. Helical temperature perturbations associated with tearing modes in tokamak plasmas. *Phys. Plasmas*, **2**(3), 825 (1995). doi:10.1063/1.871434.

[Fitzpatrick09] Fitzpatrick, R. Introduction to plasma physics: A graduate level course (2009). URL http://farside.ph.utexas.edu/teaching/plasma/plasma.html.

[Furth63] Furth, H.P., Killeen, J., and Rosenbluth, M.N. *Phys. Fluids*, **6**(4), 459 (1963). doi:10.1063/1.1706761.

[Ghendrih96] Ghendrih, P., Grosman, A., and Capes, H. Theoretical and experimental investigations of stochastic boundaries in tokamaks. *Plasma Phys. Control. Fusion*, **38**, 1653–1724 (1996). doi:10.1088/0741-3335/38/10/002.

[Gourdon] Gourdon, C. *Programme Optimise de Calculs Numeriques Dans le Configurations Magnetique Toroidales*. CEN, Fontenay aux Roses.

[Grad71] Grad, H. In *Plasma Physics and Controlled Nuclear Fusion Research*, volume 3, page 229. IAEA, Vienna (Madison, 1971).

[Gude99] Gude, A., Günter, S., Sesnic, S., and ASDEX Upgrade Team. Seed island of neoclassical tearing modes at ASDEX Upgrade. *Nucl. Fusion*, **39**, 127 (1999). doi:10.1088/0029-5515/39/1/308.

[Gude02] Gude, A., Günter, S., Maraschek, M., Zohm, H., and ASDEX Upgrade Team. Temporal evolution of neoclassical tearing modes and its effect on confinement reduction in ASDEX Upgrade. *Nucl. Fusion*, **42**, 833–840 (2002). doi:10.1088/0029-5515/42/7/306.

[Günter98] Günter, S., Gude, A., Maraschek, M., Sesnic, S., Zohm, H., and ASDEX Upgrade Team. Beta scaling for the onset of neoclassical tearing modes at ASDEX Upgrade. *Nucl. Fusion*, **38**(10), 1431–1434 (1998). doi:10.1088/0029-5515/38/10/102.

[Günter01] Günter, S., Gude, A., Maraschek, M., Sesnic, S., Zohm, H., ASDEX Upgrade Team, and Howell, D.F. High-confinement regime at high β_N values due to a changed behavior of the neoclassical tearing modes. *Phys. Rev. Letters*, **87**(27), 275001 (2001). doi:10.1103/PhysRevLett.87.275001.

[Günter03] Günter, S., Gantenbein, G., Gude, A., et al. Neoclassical tearing modes on ASDEX Upgrade: improved scaling laws, high confinement at high β_N and new stabilization experiments. *Nuclear Fusion*, **43**(3), 161–167 (2003).

doi:10.1088/0029-5515/43/3/301.

[Günter04] Günter, S., Maraschek, M., de Baar, M., Howell, D.F., Poli, E., Strumberger, E., Tichmann, C., and ASDEX Upgrade Team. The frequently interrupted regime of neoclassical tearing modes (FIR-NTMs): required plasma parameters and possibilities for its active control. *Nucl. Fusion*, **44**, 524–532 (2004). doi:10.1088/0029-5515/44/4/006.

[Günter05] Günter, S., Yu, Q., Krüger, J., and Lackner, K. Modelling of heat transport in magnetised plasmas using non-aligned coordinates. *J. Comput. Phys.*, **209**(1), 354–370 (2005). doi:10.1016/j.jcp.2005.03.021.

[Günter07] Günter, S., Lackner, K., and Tichmann., C. Finite element and higher order difference formulations for modelling heat transport in magnetised plasmas. *J. Comput. Phys.*, **226**(2), 2306–2316 (2007). doi:10.1016/j.jcp.2007.07.016.

[Günter08] Günter, S. and Lackner, K. A mixed implicit-explicit finite difference scheme for heat transport in magnetised plasmas. *J. Comput. Phys.*, **228**, 282 (2008). doi:10.1016/j.jcp.2008.09.012.

[Gupta00] Gupta, A. and Joshi, M. WSMP: Watson sparse matrix package, Part II – direct solution of general sparse systems. IBM Research Report RC 21888 (98472), IBM T. J. Watson Research Center, 1101 Kitchawan Road, Yorktown Heights, NY 10598 (2000). URL `http://www.alphaworks.ibm.com/tech/wsmp`.

[Hartfuss97] Hartfuss, H.J., Geist, T., and Hirsch, M. Heterodyne methods in millimetre wave plasma diagnostics with applications to ECE, interferometry and reflectrometry. *Plasma Phys. Control. Fusion*, **39**(11), 1693–1769 (1997). doi:10.1088/0741-3335/39/11/001.

[Hegna97] Hegna, C.C. and Callen, J.D. On the stabilization of neoclassical magnetohydrodynamic tearing modes using localized current drive or heating. *Phys. Plasmas*, **4**, 2940 (1997). doi:10.1063/1.872426.

[Hender92] Hender, T.C., Fitzpatrick, R., Morris, A., et al. Effect of resonant magnetic perturbations on COMPASS-C tokamak discharges. *Nucl. Fusion*, **32**, 2091 (1992). doi:10.1088/0029-5515/32/12/I02.

[Hender07] Hender, T., Wesley, J., Bialek, J., et al. Chapter 3: MHD stability, operational limits and disruptions. *Nuclear Fusion*, **47**(6), S128–S202 (2007). doi:10.1088/0029-5515/47/6/S03.

[Hermann03] Hermann, A. Special issue on ASDEX Upgrade. *Fusion Science and Tech-*

nology, **44**(3) (2003). URL http://www.new.ans.org/pubs/journals/fst/v_44:3.

[Hirshman86a] Hirshman, S.P. and Lee, D.K. MOMCON: A spectral code for obtaining three-dimensional magnetohydrodynamic equilibria. *Comput. Phys. Commun.*, **39**(2), 161–172 (1986). doi:10.1016/0010-4655(86)90127-X.

[Hirshman86b] Hirshman, S.P., van Rij, W.I., and Merkel, P. Three-dimensional free boundary calculations using a spectral green's function method. *Comput. Phys. Commun.*, **43**(1), 143–155 (1986). doi:10.1016/0010-4655(86)90058-5.

[Inagaki04] Inagaki, S., Tamura, N., Ida, K., Nagayama, Y., Kawahata, K., Sudo, S., T.Morisaki, Tanaka, K., Tokuzawa, T., and LHD Experimental Group. Observation of reduced heat transport inside the magnetic island O point in the Large Helical Device. *Phys. Rev. Lett*, **92**(5), 055002 (2004). doi:10.1103/PhysRevLett.92.055002.

[Isayama00] Isayama, A., Kamada, Y., Ide, S., et al. Complete stabilization of a tearing mode in steady state high-β_p H-mode discharges by the first harmonic electron cyclotron heating/current drive on JT-60U. *Plasma Phys. Control. Fusion*, **42**, L37 (2000). doi:10.1088/0741-3335/42/12/102.

[Kadomtsev79] Kadomtsev, B.B. and Pogutse, O.P. Proceedings of the 7th international conference. In *Plasma Physics and Controlled Nuclear Fusion Research*, volume 1, page 649. International Atomic Energy Agency, Vienna (1979).

[Krommes83] Krommes, J.A., Oberman, C., and Kleva, R.G. Plasma transport in stochastic magnetic fields. Part 3. kinetics of test particle diffusion. *Journal of Plasma Physics*, **30**(1), 11–56 (1983). doi:10.1017/S0022377800000982.

[La Haye00] La Haye, R.J., Buttery, R.J., Günter, S., Huysmans, G.T.A., Maraschek, M., and Wilson, H.R. Dimensionless scaling of the critical beta for onset of a neoclassical tearing mode. *Physics of Plasmas*, **7**(8), 3349–3359 (2000). doi:10.1063/1.874199.

[La Haye06] La Haye, R.J. Neoclassical tearing modes and their control. *Phys. Plasmas*, **13**(5), 055501 (2006). doi:10.1063/1.2180747.

[Lang03] Lang, P., Neuhauser, J., Horton, L., et al. ELM frequency control by continuous small pellet injection in ASDEX Upgrade. *Nuclear Fusion*, **43**(10), 1110–1120 (2003). doi:10.1088/0029-5515/43/10/012.

[Liewer85] Liewer, P.C. Measurements of microturbulence in tokamaks and comparisons with theories of turbulence and anomalous transport. *Nuclear Fusion*, **25**(5), 543 (1985).

[Malone75] Malone, R.C., McCrory, R.L., and Morse, R.L. Indications of strongly flux-limited electron thermal conduction in laser-target experiments. *Phys. Rev. Lett.*, **34**, 721 (1975). doi:10.1103/PhysRevLett.34.721.

[Maraschek03] Maraschek, M., Sauter, O., Günter, S., Zohm, H., and ASDEX Upgrade Team. Scaling of the marginal β_p of neoclassical tearing modes during power ramp-down experiments in ASDEX Upgrade. *Plasma Physics and Controlled Fusion*, **45**(7), 1369–1384 (2003). doi:10.1088/0741-3335/45/7/322.

[Maraschek07] Maraschek, M., Gantenbein, G., Yu, Q., Zohm, H., Günter, S., Leuterer, F., Manini, A., ECRH Group, and ASDEX Upgrade Team. Enhancement of the stabilization efficiency of a neoclassical magnetic island by modulated electron cyclotron current drive in the ASDEX Upgrade tokamak. *Phys.Rev.Lett.*, **98**(2), 025005 (2007). doi:10.1103/PhysRevLett.98.025005.

[McCarthy99a] McCarthy, P.J. Analytical solutions to the Grad-Shafranov equation for tokamak equilibrium with dissimilar source functions. *Phys. Plasmas*, **6**(9), 3554 (1999). doi:10.1063/1.873630.

[McCarthy99b] McCarthy, P.J., Martin, P., and Schneider, W. The CLISTE interpretive equilibrium code. Technical Report IPP-Report 5/85, Max-Planck-Institut für Plasmaphysik, Boltzmannstraße 2, 85748 Garching, Germany (1999). URL `http://edoc.mpg.de/display.epl?mode=doc&id=413804&col=33&grp=1311#cb`.

[Meskat01] Meskat, J.P., Zohm, H., Gantenbein, G., Günter, S., Maraschek, M., Suttrop, W., Yu, Q., and ASDEX Upgrade Team. Analysis of the structure of neoclassical tearing modes in ASDEX Upgrade. *Plasma Phys. Control. Fusion*, **43**, 1325–1332 (2001). doi:10.1088/0741-3335/43/10/304.

[Neubauer05] Neubauer, O., Czymek, G., Finken, K.H., Giesen, B., Huttemann, P.W., Lambertz, H.T., Schruff, J., and TEXTOR Team. The dynamic ergodic divertor in TEXTOR – a novel tool for studying magnetic perturbation field effects. *Fusion Engineering and Design*, **75–79**, 495–498 (2005). doi:10.1016/j.fusengdes.2005.06.208.

[Park03] Park, H., Chang, C.C., Deng, B.H., et al. Recent advancements in microwave imaging plasma diagnostics. *Rev. Sci. Instrum.*, **74**(10), 4239 (2003). doi:10.1063/1.1610781.

[Poli02] Poli, E., Peeters, A.G., Bergmann, A., Günter, S., and Pinches, S.D. Reduction of the ion drive and ρ_θ^* scaling of the neoclassical tearing mode. *Phys. Rev. Letters*, **88**(7), 075001 (2002). doi:10.1103/PhysRevLett.88.075001.

[Rechester78] Rechester, A.B. and Rosenbluth, M.N. Electron heat transport in a tokamak with destroyed magnetic surfaces. *Phys. Rev. Lett.*, **40**(1), 38–41 (1978). doi:10.1103/PhysRevLett.40.38.

[Rover99] Rover, M., Schilham, A.M.R., Montvai, A., and Cardozo, N.J.L. Test particle transport in perturbed magnetic fields in tokamaks. *Phys. Plasmas*, **6**(6), 2443–2451 (1999). doi:10.1063/1.873516.

[Rutherford73] Rutherford, P.H. Nonlinear growth of the tearing mode. *Phys. Fluids*, **16**(11), 1903 (1973). doi:10.1063/1.1694232.

[Sauter97] Sauter, O., Haye, R.J.L., Chang, Z., et al. Beta limits in long-pulse tokamak discharges. *Phys. Plasmas*, **4**(5), 1654 (1997). doi:10.1063/1.872270.

[Scott85] Scott, B.D., Drake, J.F., and Hassam, A.B. Nonlinear stability of drift-tearing modes. *Phys. Rev. Lett.*, **54**(10), 1027–1030 (1985). doi:10.1103/PhysRevLett.54.1027.

[Spakman08] Spakman, G., Hogeweij, G., Jaspers, R., et al. Heat pulse propagation studies around magnetic islands induced by the dynamic ergodic divertor in textor. *Nucl. Fusion*, **48**, 115005 (2008). doi:10.1088/0029-5515/48/11/115005.

[Spitzer53] Spitzer, L. and Härm, R. Transport phenomena in a completely ionized gas. *Phys. Rev.*, **89**(5), 977–981 (1953). doi:10.1103/PhysRev.89.977.

[Stix78] Stix, T.H. *Nucl. Fusion*, **18**, 353 (1978).

[Strumberger02] Strumberger, E., Merkel, P., Schwarz, E., and Tichmann, C. MFBE 2001: Computation of magnetic fields of ideal MHD equilibria. Technical Report IPP-Report 5/100, Max-Planck-Institut für Plasmaphysik, Boltzmannstraße 2, 85748 Garching, Germany (2002). URL `http://edoc.mpg.de/display.epl?mode=doc&id=250778&col=33&grp=1311#cb`.

[Strumberger04] Strumberger, E., Günter, S., Hobirk, J., Igochine, V., Merkl, D., Schwarz, E., Tichmann, C., and ASDEX Upgrade Team. Numerical investigations of axisymmetric equilibria with current holes. *Nucl. Fusion*, **44**, 464–472 (2004). doi:10.1088/0029-5515/44/3/012.

[Strumberger05] Strumberger, E. and Schwarz, E. Vacfield code: Computation of the vacuum magnetic field and its first derivatives for various coil types. Technical Report IPP-Report 5/112, Max-Planck-Institut für Plasmaphysik, Boltzmannstraße 2, 85748 Garching, Germany (2005). URL `http://edoc.mpg.de/display.epl?mode=doc&id=222046&col=33&grp=1311#cb`.

[Suttrop07] Suttrop, W., Bertoncelli, T., Bobkov, V., et al. Active in-vessel coils and a conducting wall for MHD control in ASDEX upgrade. In *Europhysics Conference Abstracts (CD-ROM), Proc. of the 34th EPS Conference on Controlled Fusion and Plasma Physics, Warsaw, Poland, 2007*, volume 31F, page P5.119. EPS, Geneva (2007).

[Tokar07] Tokar, M.Z. and Gupta, A. Elucidation of the heat-flux limit from magnetic-island heating. *Phys. Rev. Lett.*, **99**(22), 225001 (2007). doi:10.1103/PhysRevLett.99.225001.

[Wagner82] Wagner, F. Recent results of H-mode studies on ASDEX. In *Proceedings of the Thirteenth Conference on Plasma Physics and Controlled Nuclear Fusion Research*, volume I, page 277. IAEA, Vienna (1982).

[Wesson04] Wesson, J. *Tokamaks*. Clarendon Press, Oxford, 3rd edition (2004). ISBN 978-0198509226.

[Yu00] Yu, Q., Günter, S., Giruzzi, G., Lackner, K., and Zabiego, M. Modeling of the stabilization of neoclassical tearing modes by localized radio frequency current drive. *Phys. Plasmas*, **7**(1), 312 (2000). doi:10.1063/1.873799.

[Yu06] Yu, Q. Numerical modeling of diffusive heat transport across magnetic islands and local stochastic field. *Phys. Plasmas*, **13**(6), 062310 (2006). doi:10.1063/1.2206788.

[Yu09] Yu, Q., Günter, S., and Finken, K.H. Effect of resonant helical magnetic fields on plasma rotation. *Phys. Plasmas*, **16**(4), 042301 (2009). doi:10.1063/1.3100236.

[Zohm99] Zohm, H., Gantenbein, G., Giruzzi, G., et al. Experiments on neoclassical tearing mode stabilization by ECCD in ASDEX Upgrade. *Nucl. Fusion*, **39**, 577 (1999). doi:10.1088/0029-5515/39/5/101.

[Zohm01] Zohm, H., Gantenbein, G., Gude, A., et al. The physics of neoclassical tearing modes and their stabilization by ECCD in ASDEX Upgrade. *Nucl. Fusion*, **41**(2), 197–202 (2001). doi:10.1088/0029-5515/41/2/306.

Acknowledgments

At this point I would like to thank everyone who supported me during the preparation of this dissertation, especially

- Sibylle Günter for giving me the opportunity to work on this PhD thesis at IPP Garching, for taking time even when there was none, for many illuminating discussions, for answering so many questions, and for all the advice that helped to improve the structure and quality of this dissertation.
- Qingquan Yu for many fruitful discussions on physical, mathematical, numerical and whatsoever problems.
- Ivo Classen for providing ECE-Imaging data for the comparisons to experimental measurements at, both, TEXTOR and ASDEX Upgrade and for answering many questions related to the experiments.
- the ASDEX Upgrade Team for providing me with the experimental data I compared my simulations to. Special thanks go to Marc Maraschek, Giovanni Tardini, Rainer Fischer, Christoph Fuchs, Nathaniel Hicks, Alexander Mlynek, and Thomas Pütterich.
- the TEXTOR Team for the experimental data required for the comparison of simulations and island measurements.
- Erika Strumberger, Elisabeth Schwarz, and Christiane Tichmann for support using the MHD equilibrium code package and some adaptations of it to my requirements.
- Klaus Reuter for being a great office mate, for many nice discussions, and quite some technical help.